UNIVERSITY OF OKLAHOMA

GRADUATE COLLEGE

ANALYSIS AND CONTROL OF THERMOELASTIC VIBRATIONS IN PLATE STRUCTURES

A Dissertation

SUBMITTED TO THE GRADUATE FACULTY

in partial fulfillment of the requirements for the

degree of

Doctor of Philosophy

By

Robert J. Adams
Norman, Oklahoma
2001

UMI Number: 3034595

UMI

ProQuest Information and Learning Company
300 North Zeeb Road
P.O. Box 1346
Ann Arbor, MI 48106-1346

ANALYSIS AND CONTROL OF THERMOELASTIC VIBRATIONS
IN PLATE STRUCTURES

A Dissertation APPROVED FOR THE
SCHOOL OF AEROSPACE AND
MECHANICAL ENGINEERING

BY

ACKNOWLEDGMENTS

I owe an enormous debt of thanks to Dr. Charles W. Bert. His patient support over the long course of my Doctoral studies and his encouragement to complete my dissertation after several "false starts," will guide me always.

My deepest thanks to the members of my committee for their patience and the comments they supplied concerning the content of the dissertaion. Dr. Kevin Grasse for his help with math and control theory problems. and whose kindness and support inspired me to suceed. Dr. Striz for his assistance with finite elements. Dr. Lai for his help with heat transfer theory. and Dr. J. David Baldwin for joining my committee on short notice when Dr. Egle retired.

To Dr. Davis M. Egle for his support during the first few years of my Doctoral studies and his tutelage during my undergraduate and graduate studies.

To Jonathan Bar-on. friend. collaborator. and mentor. who taught me the value of rigorous analysis. His reviews of this work. and his honest penetrating inquisition helped improve and finalize this dissertation.

A special belated thanks to Dr. William N. Patten whose enthusiasm for control and estimation theory first motivated me to study those subjects.

To my children. Chelsea and Truman. who are a constant reminder that there is much more to life than education and a successful career.

Lastly to my wife. Vinh N. Adams. whose life was affected by this work much more than my own. Without her I would have never finished my Doctoral studies. She taught me. by example. that with hard work and perseverance you can achieve your goals.

DEDICATION

One must not lose desires. They are mighty stimulants to creativeness, to love, and to long life.

— Alexander A. Bogomoletz

Do not take life too seriously. You will never get out of it alive.

— Elbert Hubbard

TABLE OF CONTENTS

LIST OF TABLES

LIST OF FIGURES

ABSTRACT

This work is concerned with the analysis and control of thermoelastic vibrations in rectangular plate structures using piezoelectric materials for the sensor(s) and actuator(s). Both isotropic and symmetrically laminated. cross–ply composite plates subjected to mechanical and thermal loads are studied. Chapter 2 develops an analytical solution for the case of a simply supported. rectangular symmetrically laminated. cross–ply composite plate subjected to a thermal shock. The analysis includes the interaction between the strain and temperature fields and. in the case of the composite plates, investigates the effect of accounting for the orthotropic material properties in the governing elastic and thermal equations. The resulting solution for the vibration of the composite plate is compared to a previous analysis of a homogeneous. isotropic. rectangular plate. Comparison indicates that. while the solutions have similar forms. the explicit summation in the isotropic solution has been replaced by implied summations resulting from vector inner product multiplications in the composite solution. Chapter 3 develops a new coupled thermoelastic finite element model of a rectangular plate with embedded piezoelectric patches suitable for closed loop vibration control. The open loop response of this model subjected to a thermal shock is validated against the response of the Chapter 2 solution. and the closed loop response is validated against previous work. In both cases. the new finite element model compared favorably. Chapter 4 describes an approach used to design controllers suitable for closed-loop control of plate thermoelastic vibrations. and applies this approach to two different design problems. Chapter 5 presents the conclusions and suggestions for future work.

CHAPTER 1

INTRODUCTION AND LITERATURE REVIEW

1.1 Introduction

The past two decades has seen a flurry of research activity in the field of intelligent, or smart, structures as witnessed by the number of reference articles contained in the survey papers of Rao and Sunar [1] and Crawley [2], a pioneer in this field. Intelligent structures are defined by Wada *et al* [3] as actively controlled structures with a highly distributed, as opposed to a localized, control system. Much of this work has focused on the use of piezolectric materials to provide the sensing and actuation capabilities of the control system. Piezoelectric materials can be used as sensors because they possess a phenomenon called the direct piezoelectric effect. This means that, when the material is subjected to a mechanical force, the induced strain produces an electrical charge in the material. Conversely, when the material is subjected to an electric field, the material reacts by producing a strain or mechanical force. This is the converse piezoelectric effect, and is the basis of the use of piezoelectric materials as actuators. The most commonly studied piezoelectric materials are lead zirconate titanate (PZT) and polyvinylidene flouride (PVDF or PVF_2). Most studies of intelligent structures are in the area of vibration control, with some work in the area of buckling enhancement [4]. Recently, research has focused on control of thermally induced vibrations of intelligent structures, *e.g.*, the papers by Tauchert [5], Tzou and Howard [6], Chandrashekhara and Kolli [7], Tang and Xu [8], and Zhou *et al* [9]. A thorough understanding of the coupling between the thermal, mechanical, and electric fields is required to achieve the promise of intelligent structures as, by definition, these structures will contain the heat generating power electronics as part of the distributed control system. This work is concerned with the control of thermoelastic vibrations in rectangular plate structures using piezoelectric materials for the sensor(s) and actuator(s). Both homogeneous, isotropic and symmetrically laminated, cross-ply composite plates subjected to thermal and mechanical loads are studied and compared.

1.2 Literature Review:

The following literature review lists all papers reviewed over the course of this work. The papers are grouped according to the field of study, thermoelastic, piezoelectromechanical, and piezothermoelastic. Within each group, the papers are listed in chronological order.

1.2.1 Thermoelastic Literature Review

The response of a homogeneous isotropic plate subject to a thermal shock was first treated by Boley and Weiner [10], and Kovalenko and Kharnaukhov [11]. These works ignored the interaction of the strain and temperature fields which adds damping to the system. Kozlov [12] included the interaction of the strain and temperature fields in his analysis of a rectangular, homogeneous isotropic plate.

Chung [13] performed an early survey of dynamic problems of thermoelasticity. Both linear and nonlinear vibration problems in thermomechanics associated with elasticity, viscoelasticity, plasticity, and magnetoelasticity were presented.

Ignaczak's survey paper [14] presented a look at the historical development of linear dynamic thermoelasticity over the period 1836 – 1981. A linear theory of non-steady heat conduction was combined with elastodynamics to describe thermo-mechanical processes in a solid body. Due to the complicated structure of the governing equations, only a few one-dimensional initial boundary value problems had been solved in a form suitable for complete analysis. A relatively large number of problems that had been solved successfully concerned periodic thermoelastic disturbances. The reason is that the periodicity hypothesis allowed the reduction of the governing equations to a form appropriate for the application of classical elastodynamics. The survey also included a description of the fundamental results of a basic system of field equations for dynamic thermoelasticity with relaxation times. Suggestions concerning areas of the theory that were critically in need of further investigation were given. This survey paper contains 50 references. The second survey [15] covered the significant and numerous developments in the field of thermoelasticity that had occurred during the first half of the 1980's. This included coupled thermoelasticity with or without relaxation times.

Included were new global balance laws, domain of influence theorems, convolutional variational principles, closed-form aperiodic-in-time fundamental solutions, qualitative properties of particular solutions, and results on thermoelastic waves propagating in beams, plates, and shells. This survey paper contains 84 references.

Tauchert [16] presented a survey of investigations concerned with the response of flat plates to thermal loadings. The three major topics were: (*i*) thermally induced bending, (*ii*) buckling, postbuckling, and large deformation behaviors, and (*iii*) vibrational characteristics associated with elevated temperatures and rapid heating.

Chandrashekhara [17] used a finite element formulation to analyze the buckling behavior of laminated composite plates subjected to a uniform temperature field. Transverse shear flexibility was accounted for in the analysis using the thermoelastic version of the first-order shear deformation theory.

Mukherjee and Sinha [18] examined the coupled dynamic thermoelastic response of a fibrous composite plate exposed to a thermal shock. An explicit and integrated finite element method was employed to solve the associated coupled thermoelastic equations simultaneously. Classical linear coupled thermoelastic theory was considered for a laminated composite plate. The structural model included the effects of extension-bending-twisting coupling, shear deformation, and rotary coupling inertias. An example was presented of a simply supported carbon-carbon composite plate subjected to a central thermal shock.

Tamma and Namburu [19] presented an overview of non-classical and classical dynamic thermoelasticity models and equations governing thermal-structural interactions. Attention was focused on the computational approaches for the modeling and analysis of various classes of problems encompassing thermal-structural interactions. These interactions were broadly classified as: (*i*) thermally-induced stress wave propagation problems, (*ii*) thermally-induced dynamic (inertial type) problems, and (*iii*) the general field of thermal stresses. A variety of illustrative numerical examples encompassing non-classical and classical influences were presented to provide an improved understanding of the behavior of thermal-structural problems via effective unified computational developments.

This review article contains 142 references.

Blandino and Thornton [20] described the first detailed study of thermally induced vibration caused by internal heating. A mathematical model was developed to predict the thermal-structural behavior of an internally heated beam. The results from the model were compared to the results obatined from an experiment. The model accurately predicted the steady-state temperatures, adequately predicted the steady-state displacements, and predicted the displacement histories with some error. The analysis revealed that the natural frequency of the beam was more important than the heating rate in determining if vibrations will occur, and the convection heat transfer governed the amplitude of vibrations and steady-state amplitude. This study showed that thermally induced vibrations of internally heated beams belong to the class of vibrations called self-sustaining oscillations.

1.2.2 Piezoelectromechanical Literature Review

Crawley and Anderson [21] developed techniques for modeling induced strain actuation of beam-like components of intelligent structures. The models presented described the detailed mechanics of induced strain actuators bonded to and embedded in one-dimensional structures. The specific characteristics of one type of induced strain actuator, piezoceramic materials, were discussed, and implications for practical use of piezoceramic actuators were outlined.

Crawley and Lazarus [22] developed and experimentally verified the induced strain actuation of plate components of an intelligent structure. Equations relating the actuation strains, created by induced strain actuators, to the strains induced in the actuator/substrate system were derived for isotropic and anisotropic plates. Plate strain energy relations were also developed.

Lee [23] presented theory and experimental validation of various aspects of vibration control using piezoelectric sensors and actuators. Topics covered included Classical Laminated Plate Theory with embedded piezoelectric sensors and actuators, twisting/bending sensors and actuators, vibration control of a cantilever beam using modal sensors and actuators, spatial filters to measure wave propagation which can be used to develop non-causal vibration sensors, and piezoelectric strain rate sensors.

Chandrashekhara and Agarwal [24] used a finite element formulation for modeling the behavior of laminated composites with integrated sensors and actuators. The formulation was based on the first-order shear deformation theory, which is applicable for both thin and moderately thick plates. The model was valid for both continuous and segmented piezoelectric elements that can be either surface bonded or embedded in the laminated plate.

Tzou and Fu, Part I [25], developed a plate model for segmented sensors and actuators using a modal decomposition method. A model with single-piece symmetrically distributed sensors and actuators was compared to a model with quarterly segmented-distributed sensors and actuators. For symmetric boundary conditions, it was analytically shown that the single piece sensor/actuator was incapable of sensing/controlling the antisymmetric (even) modes. The quarterly segmented-distributed sensor/actuator was capable of sensing/controlling all but the quadruple modes. In Part II [26], active vibration control of a plate with various sizes of sensors/actuators and control algorithms, proportional feedback and Lyapunov, was investigated. Time-history responses of the plate with and without feedback controls were analyzed and compared.

Barret [27] investigated the characteristics of directionally attached piezoelectric (DAP) elements and constructed a low aspect ratio DAP torque-plate wing. Closed-form expressions of DAP strains based on laminated plate theory were presented. The models demonstrated that DAP elements can generate pure extension, bending, or twist deflections in beams and plates. Experimental beam specimens were constructed to verify the models. Tests showed that 0.030-inch (0.0762-cm) thick aluminum beams with antisymmetrically laminated DAP elements produced twist rates of 0.23 degree/inch (9 degree/meter) and bending rates in excess of 0.36 degree/inch (14 degree/meter) with theory and experiment in close agreement. A DAP torque-plate was constructed of 8.0-mil-thick piezoceramic elements bonded antisymmetrically on a 5-mil steel substrate. The torque plate was then used to induce pitch deflections in a subsonic missile fin with a NACA 0012 profile and an aspect ratio of 1.4. The wing demonstrated a break frequency in excess of 80 Hz and static pitch deflections of 8.5 degree, showing excellent correlation with theory.

Rao and Sunar [1] presented a survey of the recent research trends addressing piezoelectricity in the context of distributed sensing and control of flexible structures. A brief history of piezoelectricity is also noted. This article contains 145 references.

Anderson and Hagood [28] developed a general formulation for coupled electromechanical modelling specialized to the analysis of transducers used for simultaneous sensing and actuation.

Crawley [2] presented an overview and assessment of the technology leading to the development of intelligent structures, and listed the present and future needs required to fulfill the promise of intelligent structures. This article contains 128 references.

Gu *et al* [29] performed an experimental investigation into the implementation of shaped PVDF modal sensors to control specific modes of vibration of a simply supported rectangular plate. The plate was excited by a steady-state harmonic point force while the control was achieved by two independent piezoelectric actuators bonded to the surface of the plate.

Main and Garcia [30] presented data illustrating the need for inclusion of piezoelectric nonlinearities if accurate system models are desired. The analysis used describing functions to improve the overall accuracy of the system model, but also noted that describing functions are extremely sensitive to amplitude at low actuator displacements which compromises the accuracy of system models that include voltage-controlled piezoelectric actuators. It was also demonstrated that using charge-feedback control with piezoelectric actuators makes the use of nonlinear elements less pressing since the charge control describing functions are much nearer unity than their voltage-control counterparts.

Chen and Chopra [31] developed a smart rotor with active control of blade twist using embedded piezoceramic elements as sensors and actuators to minimize rotor vibrations. A 1/8 Froude-scale (dynamically scaled) bearingless helicopter rotor model was built with banks of torsional actuators capable of manipulating blade twist at frequencies from 5 to 100 Hz. The effectiveness of the torsional actuators and vibration suppression capabilities were assessed using wind tunnel tests. Accelerometers embedded in the blade tip were used to measure the oscillatory blade twist response. The changes in rotor vibratory loads due to piezoinduced twist were determined using a rotating hub balance located at the rotor hub. Experimental test results showed that tip twist amplitudes on the order of 0.5 degree were attainable in forward flight. Although these amplitudes were less than the target value (1 to 2 degree for complete vibration suppression control), test results showed that partial vibration reduction was possible. Open-loop phase shift control of blade twist at the first four rotor harmonics was used, and changes in rotor thrust of up to 9 percent of the steady-state values were measured.

Barret *et al* [32] presented two new designs for aerodynamic control surfaces that employ piezoceramic actuation elements. These control surfaces consisted of a graphite/epoxy shell that is free to rotate around a stiff graphite/epoxy spar, with the rotation controlled by piezoceramic (PZT) element(s). The authors refer to this class of control surfaces as Flexspars. The tip-joint Flexspar was designed for low-torque large deflection applications, and uses one PZT bender element. The shell-joint Flexspar was designed for high-torque small deflection applications, and uses multiple PZT bender elements. Classical laminated plate theory was used to predict the bending curvature of the PZT bender elements and kinematics was used to determine the associated control surface deflection. A tip-joint Flexspar was constructed to verify the theory and determine the dynamic characteristics. Several bench and wind tunnel tests were performed to determine the actuation range and frequency response of the test specimen.

1.2.3 Piezothermoelasticity Literature Review

Nowacki [33] presented a thorough treatment of the theory of dynamic thermoelasticity including piezothermoelasticity and magnetothermoelasticity. The theoretical foundations of dynamic thermoelasticity were presented in a context useful to practicing engineers and scientists. It described, through examples and discussions, the magnitudes of the coupling effects which distinguish this subject from previous works in thermoelasticity. This book, published in 1975, is an English translation of the original monograph written in Polish and published in 1966.

Tauchert [5] examined the response of a thin composite plate constructed of piezothermoelastic layers and subject to stationary thermal and electric fields. Solutions based on classical lamination theory were extended to include piezoelectric effects for a "free" plate of arbitrary contour and for a simply supported, rectangular plate. This analysis assumed a linear temperature gradient through the thickness of the plate.

Tzou and Howard [6] developed a generic piezothermoelastic shell theory for thin piezoelectric shells using the linear piezoelectric theory and Kirchoff-Love assumptions. A simplification procedure, based on the Lamé parameters and radii of curvatures, was proposed, and applications of the theory to (1) a piezoelectric cylindrical shell, (2) a piezoelectric ring, and (3) a piezoelectric beam were presented.

Tang and Xu [8] presented a theory for dynamic analysis of piezothermoelastic laminated plates. The general dynamic equations, which include mechanical, thermal, and electric effects, were derived based on the anisotropic composite laminated plate theory. Analytical dynamic solutions were obtained for the case of general forces acting on a simply supported piezothermoelastic laminated plate. As a special application of the solutions, they examined the harmonic response to temperature variations and an electric fields. Their analysis assumed a linear temperature gradient through the thickness of the plate.

Chandrashekhara and Kolli [7] developed a mathematical model for the active control of thermally induced vibration of laminated doubly curved shells with piezoelectric sensors and actuators, assuming a linear temperature gradient. Their model took into account the mass, stiffness, and thermal expansion of the piezoelectric patches. A C^0 continuous nine noded shear flexible element was implemented to model the shell. A constant gain positive position feedback algorithm was used to actively control the dynamic response of the shell in a closed loop.

Lee and Saravanos [34] used discrete-layer mechanics to develop a model of the completely coupled mechanical, electrical, and thermal response of piezoelectric composite beams. Finite element equations were developed and implemented for a beam element with linear shape functions. Comparisons with conventional thermoelastic finite element analysis and classical beam theory were presented. Numerical studies were used to demonstrate the capabilities of the model to predict the thermal deformation of composite beams, as well as the active compensation of these thermal deformations using piezoelectric structures.

Smittakorn and Heyliger [35] studied the steady-state and transient behavior of laminated hygrothermopiezoelectric plates under the coupled effects of mechanical, electrical, thermal, and moisture fields. A three-dimensional discrete-layer model was developed for analyzing rectangular multilayered laminated plates with various types of boundary condition. The discrete-layer model employed one-dimensional finite-element approximations in the through-thickness direction, and two-dimensional in-plane analytical functions (*e.g.*, trigonometric and polynomial functions). The laminates were excited by surface tractions, electric potentials, temperature, and/or moisture concentration on top, interlaminar, and bottom surfaces.

Zhou *et al* [9] recently developed a completely coupled thermo-piezoelectric-mechanical theory to model the response of composite plates with surface bonded piezoelectric actuators. They used a higher-order laminate theory to describe the displacement fields to accurately model the transverse shear deformation. They used a higher-order temperature theory to model the temperature distribution through the thickness of the composite plates. A two-dimensional finite element model was used to implement the coupled theory. Studies were performed to analyze the response of a plate under thermal and piezoelectric loads. Numerical results indicated that the the thermo-piezoelectric-mechanical coupling has significant effect on the dynamic response of composite plates.

1.3 Significance of This Research

In the current work, two models that can be used to solve the coupled thermoelastic differential equations governing the response of a laminated composite to mechanical and thermal loading were developed. These models accurately predict the temperature field in a laminated composite subjected to thermal loads.

The first model is an analytical solution of the dynamic response of a rectangular, simply supported, symmetrically laminated, composite plate subjected to an external thermal shock. This is an extension of the work on rectangular, homogeneous, isotropic plates performed by Kozlov [12]. Comparison of the two solutions using a rectangular aluminum plate indicates very good agreement.

The second model is a finite element model of a symmetrically laminated composite plate containing surface mounted and embedded piezoelectric elements in a form suitable for feedback control design. This model includes two-way coupling between the thermal and mechanical fields. and one-way coupling between these fields and the piezoelectric field. The piezoelectric sensors account for the one-way coupling of the thermal and mechanical fields with the piezoelectric field. and the piezoelectric actuators account for the one-way coupling of the piezoelectric field with the mechanical and thermal fields. A new technique to couple displacement plate finite elements with three-dimensional thermal finite elements was developed. Although this work is very closely related to the recent work by Zhou *et al* [9]. the major differences are:

1. A three-dimensional finite element model with linear shape functions in the plate thickness direction was used to describe the temperature distribution through the thickness of the plate instead of an assumed functional distribution. This approach allows for more general boundary conditions in the plate thickness direction at the plate edges. and the incoporation of internal heat sources.

2. The piezolectric actuators and sensors can be embedded in the plate and are not restricted to only surface bonded actuators and sensors.

3. The current work uses a 1^{st} order shear deformation theory to describe the displacement fields. while Zhou *et al* used a third-order theory.

4. The current work formulates the coupled thermopiezoelectric model in state-space form and applies recent advances in control theory to reduce the order of the model.

This model was used to design feedback controllers for two different smart plate applications using classical control performance and stability metrics in conjunction with a constrained optimization routine. The first application is concerned with designing a set of constant feedback gains to minimize the mechanical impulse response of a clamped graphite/epoxy/PZT smart plate. This study compares a linear controller with two controllers that limit the applied negative electric field to within the recommended limits for PZT. The second application requires the design of a set of constant feedback gains to minimize the thermal impulse response of a simply supported graphite/epoxy/PZT smart plate.

CHAPTER 2

THERMAL IMPACT THEORETICAL SOLUTION

2.1 Introduction

This chapter develops a theoretical solution for the response of an orthotropic simply-supported plate subjected to a thermal shock. Specifically, the solution is developed for a simply-supported, N-layer, symmetrically laminated, rectangular plate ($0 \le x \le a$; $0 \le y \le b$) that is subjected to a step heat flux of intensity q applied to the upper surface, $z = h/2$, at time $t = 0$. The lower surface, $z = -h/2$, is assumed to be thermally insulated and the temperature of the periphery of the plate is maintained at the initial temperature T_0. Additionally, the simple supports at $x = 0$ and $y = 0$ are fixed while the simple supports at $x = a$ and $y = b$ are free to move laterally. This assumption decouples the differential equations governing the in-plane effects from the differential equations governing the plate displacement. These initial and boundary conditions were chosen so that the solution could be compared to the solution for an isotropic rectangular plate derived by Kozlov [12].

2.2 Analysis

The governing differential equations for the system described in the Introduction are:

Plate displacement (ignoring mechanical damping)

$$D_{11}\frac{\partial^4 w}{\partial x^4} + 2D_k\frac{\partial^4 w}{\partial x^2 \partial y^2} + D_{22}\frac{\partial^4 w}{\partial y^4} + m\frac{\partial^2 w}{\partial t^2} + \frac{\partial^2 m_{Tx}}{\partial x^2} + \frac{\partial^2 m_{Ty}}{\partial y^2} = 0 \tag{2.1}$$

Plate thermal

$$\begin{aligned} &k_x\frac{\partial^2 T}{\partial x^2} + k_y\frac{\partial^2 T}{\partial y^2} + \frac{\partial}{\partial z}\left(k_z\frac{\partial T}{\partial z}\right) - \rho C_v\frac{\partial T}{\partial t} \\ &+T_0 z\frac{\partial}{\partial t}\left[(Q_{11}\alpha_x + Q_{12}\alpha_y)\frac{\partial^2 w}{\partial x^2} + (Q_{12}\alpha_x + Q_{22}\alpha_y)\frac{\partial^2 w}{\partial y^2}\right] = 0 \end{aligned} \tag{2.2}$$

where

$$D_k = D_{12} + 2D_{66} \tag{2.3}$$

$$m = \int_{-\frac{h}{2}}^{\frac{h}{2}} \rho dz = \sum_{i=1}^{N} h_i \rho_i \tag{2.4}$$

$$m_{Tx} = \int_{-\frac{h}{2}}^{\frac{h}{2}} (Q_{11}\alpha_x + Q_{12}\alpha_y)(T - T_0)\, z dz \tag{2.5}$$
$$m_{Ty} = \int_{-\frac{h}{2}}^{\frac{h}{2}} (Q_{12}\alpha_x + Q_{22}\alpha_y)(T - T_0)\, z dz$$

and h_i is the thickness of the i^{th} layer. These coupled differential equations are subject to the following initial conditions at time $t = 0$:

$$w = 0; \qquad \frac{\partial w}{\partial t} = 0; \qquad T = T_0 \qquad (t = 0): \tag{2.6}$$

and the following boundary conditions:

$$\begin{aligned} w &= 0; \quad \frac{\partial^2 w}{\partial x^2} = 0 \quad (x = 0,\ x = a); \\ w &= 0; \quad \frac{\partial^2 w}{\partial y^2} = 0 \quad (y = 0,\ y = b); \\ k_z \frac{\partial T}{\partial z} &= q \quad (z = \frac{h}{2}); \quad \frac{\partial T}{\partial z} = 0 \quad (z = -\frac{h}{2}); \\ T &= T_0 \quad (x = 0,\ x = a,\ y = 0,\ y = b). \end{aligned} \tag{2.7}$$

To facilitate the solution, the following dimensionless quantities are introduced

$$\begin{aligned} &\xi = \frac{x}{a}; && \eta = \frac{y}{b}; && \zeta = \frac{z}{h}; \\ &\tau = \bar{k}_z \frac{t}{h^2 \bar{\rho} \bar{C}_v}; && W = \bar{k}_z \frac{w}{q \bar{\alpha}_x a^2}; && \Theta = \bar{k}_z \frac{T - T_0}{qh}; \\ &B^4 = \frac{D_{11}}{m} \left(\frac{h^2 \bar{\rho} \bar{C}_v}{a^2 \bar{k}_z} \right)^2; && \bar{k}_z = \frac{1}{h} \sum_{i=1}^{N} h_i k_{zi}; && \bar{\alpha}_x = \frac{1}{h} \sum_{i=1}^{N} h_i \alpha_{xi}; \\ &\bar{\rho} = \frac{1}{h} \sum_{i=1}^{N} h_i \rho_i; && \bar{C}_v = \frac{1}{h} \sum_{i=1}^{N} h_i C_{vi} \end{aligned} \tag{2.8}$$

Substitution of Equations (2.8) into Equations (2.1)and (2.2) yields the following dimensionless coupled partial differential equations.

$$\frac{\partial^4 W}{\partial \xi^4} + 2C_1 \frac{\partial^4 W}{\partial \xi^2 \partial \eta^2} + C_2 \frac{\partial^4 W}{\partial \eta^4} + \frac{1}{B^4} \frac{\partial^2 W}{\partial \tau^2} - \frac{\partial^2 M_{T\xi}}{\partial \xi^2} + \frac{\partial^2 M_{T\eta}}{\partial \eta^2} = 0 \tag{2.9}$$

$$C_5 \frac{\partial^2 \Theta}{\partial \xi^2} + C_6 \frac{\partial^2 \Theta}{\partial \eta^2} + \frac{\partial}{\partial \zeta} \left(C_7 \frac{\partial \Theta}{\partial \zeta} \right) - \frac{\partial \Theta}{\partial \tau} + \zeta \frac{\partial}{\partial \tau} \left(C_8 \frac{\partial^2 W}{\partial \xi^2} + C_9 \frac{\partial^2 W}{\partial \eta^2} \right) = 0 \tag{2.10}$$

where

$$
\begin{aligned}
&M_{T\xi} = \textstyle\int_{-\frac{1}{2}}^{\frac{1}{2}} C_3(\zeta)\,\Theta\zeta d\zeta; && M_{T\eta} = \textstyle\int_{-\frac{1}{2}}^{\frac{1}{2}} C_4(\zeta)\,\Theta\zeta d\zeta; \\
&C_1 = \frac{D_k a^2}{D_{11} b^2}; && C_2 = \frac{D_{22} a^4}{D_{11} b^4}; \\
&C_3(\zeta) = \frac{h^3}{D_{11}\bar{\alpha}_x}\left(Q_{11}\alpha_x + Q_{12}\alpha_y\right); && C_4(\zeta) = \frac{h^3 a^2}{D_{11}\bar{\alpha}_x b^2}\left(Q_{12}\alpha_x + Q_{22}\alpha_y\right); \\
&C_5(\zeta) = \frac{h^2 k_x \bar{\rho}\bar{C}_v}{a^2 \bar{k}_z \rho C_v}; && C_6(\zeta) = \frac{h^2 k_y \bar{\rho}\bar{C}_v}{b^2 \bar{k}_z \rho C_v}; \\
&C_7(\zeta) = \frac{k_z \bar{\rho}\bar{C}_v}{\bar{k}_z \rho C_v}; && C_8(\zeta) = \frac{T_0\bar{\alpha}_x}{\rho C_v}\left(Q_{11}\alpha_x + Q_{21}\alpha_y\right); \\
&C_9(\zeta) = \frac{T_0\bar{\alpha}_x a^2}{\rho C_v b^2}\left(Q_{12}\alpha_x + Q_{22}\alpha_y\right); && C_{10}(\zeta) = \frac{k_z}{\bar{k}_z}
\end{aligned}
\tag{2.11}
$$

Note that while the parameters C_3 through C_{10} are functions of ζ, they are constant in each layer of a laminated composite. For a complete derivation of these non-dimensional equations see Appendix A. Substitution of Equations (2.8) into Equations (2.6) and (2.7) yields the following initial conditions and boundary conditions for the non-dimensional, coupled, differential equations expressed in Equations (2.9) and (2.10):

$$
\begin{aligned}
&W = 0; \quad \frac{\partial W}{\partial \tau} = 0; \quad \Theta = 0 \quad (\tau = 0) \\
&W = 0; \quad \frac{\partial^2 W}{\partial \xi^2} = 0 \quad (\xi = 0, \xi = 1) \\
&W = 0; \quad \frac{\partial^2 W}{\partial \eta^2} = 0 \quad (\eta = 0, \eta = 1) \\
&\Theta = 0 \quad (\xi = 0, \xi = 1, \eta = 0, \eta = 1) \\
&C_{10}(\zeta)\frac{\partial \Theta}{\partial \zeta} = 1 \quad \left(\zeta = \frac{1}{2}\right); \quad \frac{\partial \Theta}{\partial \zeta} = 0 \quad \left(\zeta = -\frac{1}{2}\right)
\end{aligned}
\tag{2.12}
$$

With the given boundary conditions the following double finite Fourier sine series in ξ and η can be used to obtain the solution of Equations (2.9) and (2.10) subject to Equations (2.12):

$$
W^*(m, n, \tau) = \int_0^1 \int_0^1 W(\xi, \eta, \tau)\sin(m\pi\xi)\sin(n\pi\eta)\,d\xi d\eta \tag{2.13}
$$

$$
\Theta^*(m, n, \zeta, \tau) = \int_0^1 \int_0^1 \Theta(\xi, \eta, \zeta, \tau)\sin(m\pi\xi)\sin(n\pi\eta)\,d\xi d\eta \tag{2.14}
$$

The inverse transformations of Equations (2.13) and (2.14) are obtained from the theory of Fourier series and have the form:

$$W(\xi,\eta,\tau) = 4\sum_{m=1}^{\infty}\sum_{n=1}^{\infty} W^{*}(m,n,\tau)\sin(m\pi\xi)\sin(n\pi\eta) \tag{2.15}$$

$$\Theta(\xi,\eta,\zeta,\tau) = 4\sum_{m=1}^{\infty}\sum_{n=1}^{\infty} \Theta^{*}(m,n,\zeta,\tau)\sin(m\pi\xi)\sin(n\pi\eta). \tag{2.16}$$

Applying the transformations (2.13) and (2.14) to Equations (2.9) and (2.10) yields

$$\frac{d^2W^{*}}{d\tau^2} - \omega_1^4 B^4 W^{*} = B^4 \int_{-\frac{1}{2}}^{\frac{1}{2}} \omega_2^2 \zeta \Theta^{*} d\zeta \tag{2.17}$$

$$\frac{\partial}{\partial\zeta}\left(C_7\frac{\partial\Theta^{*}}{\partial\zeta}\right) - \frac{\partial\Theta^{*}}{\partial\tau} - \omega_3^2\Theta^{*} = \omega_4^2\zeta\frac{dW^{*}}{d\tau} \tag{2.18}$$

where

$$\omega_1^4 = \pi^4\left(m^4 - 2C_1m^2n^2 + C_2n^4\right) \tag{2.19}$$

$$\omega_2^2(\zeta) = \pi^2\left(C_3m^2 + C_4n^2\right) \tag{2.20}$$

$$\omega_3^2(\zeta) = \pi^2\left(C_5m^2 + C_6n^2\right) \tag{2.21}$$

$$\omega_4^2(\zeta) = \pi^2\left(C_8m^2 - C_9n^2\right) \tag{2.22}$$

The parameters ω_2, ω_3, and ω_4 are functions of ζ, but are constant in each layer of a laminated composite. The differential equations (2.17) and (2.18) are subject to the following initial and boundary conditions, which are obtained by applying Equations (2.13) and (2.14) to Equations (2.12)

$$\begin{gathered}
W^{*} = 0; \qquad \frac{\partial W^{*}}{\partial\tau} = 0; \qquad \Theta^{*} = 0 \qquad (\tau = 0) \\
C_{10}\frac{\partial\Theta^{*}}{\partial\zeta} = \frac{4}{mn\pi^2} \qquad (m,n = 1,3,5,\ldots) \qquad \left(\zeta = \frac{1}{2}\right) \\
\frac{\partial\Theta^{*}}{\partial\zeta} = 0 \qquad \left(\zeta = -\frac{1}{2}\right).
\end{gathered} \tag{2.23}$$

For a layered composite, it is possible to use the finite element method to solve Equation (2.18). Properly formulated, this method constrains the temperature and heat flux at the boundaries of each layer within the plate to be equal. Using the weak form of the Galerkin finite element formulation, the weighted average of the residual can be written as

$$
\begin{aligned}
I &= \int_{-\frac{1}{2}}^{\frac{1}{2}} \left(-C_7 \frac{d\mathrm{w}}{d\zeta} \frac{\partial \bar{\Theta}^*}{\partial \zeta} - \mathrm{w} \frac{\partial \bar{\Theta}^*}{\partial \tau} - \omega_3^2 \mathrm{w} \bar{\Theta}^* - \omega_4^2 \zeta \mathrm{w} \frac{dW^*}{d\tau} \right) d\zeta + C_7 \mathrm{w} \frac{\partial \bar{\Theta}^*}{\partial \zeta} \bigg|_{-\frac{1}{2}}^{\frac{1}{2}} \\
&= \sum_{i=1}^{k} \left[\int_{\zeta_i}^{\zeta_{i+1}} \left(-C_{7i} \frac{d\mathrm{w}}{d\zeta} \frac{\partial \bar{\Theta}^*}{\partial \zeta} - \mathrm{w} \frac{\partial \bar{\Theta}^*}{\partial \tau} - \omega_{3i}^2 \mathrm{w} \bar{\Theta}^* - \omega_{4i}^2 \zeta \mathrm{w} \frac{dW^*}{d\tau} \right) d\zeta \right] \\
&\quad + C_7 \mathrm{w} \frac{\partial \bar{\Theta}^*}{\partial \zeta} \bigg|_{-\frac{1}{2}}^{\frac{1}{2}} \\
&= \sum_{i=1}^{k} \left[\int_{\zeta_i}^{\zeta_{i+1}} \left(-C_{7i} \frac{d\mathrm{w}}{d\zeta} \frac{\partial \bar{\Theta}^*}{\partial \zeta} - \mathrm{w} \frac{\partial \bar{\Theta}^*}{\partial \tau} - \omega_{3i}^2 \mathrm{w} \bar{\Theta}^* - \omega_{4i}^2 \zeta \mathrm{w} \frac{dW^*}{d\tau} \right) d\zeta \right] \\
&\quad + \frac{4}{mn\pi^2} \frac{\bar{\rho} \bar{C}_v}{\rho\left(\frac{1}{2}\right) C_v\left(\frac{1}{2}\right)}
\end{aligned} \tag{2.24}
$$

where $\bar{\Theta}^*$ is the trial function and w is the test function. In the second form. the domain has been discretized into k segments. with segment 1 being associated with the bottom of the plate ($\zeta = -1/2$). Let $\bar{\Theta}^*$ be approximated using piecewise linear shape functions. such that over the i^{th} segment the trial function is

$$
\begin{aligned}
\bar{\Theta}_i^* &= H_1(\zeta)\Theta_i^* + H_2(\zeta)\Theta_{i+1}^* \\
\Theta_i^* &= \Theta^*(\zeta_i) \\
\Theta_{i+1}^* &= \Theta^*(\zeta_{i+1})
\end{aligned} \tag{2.25}
$$

and in Galerkin's method the test functions are

$$
\begin{aligned}
\mathrm{w}_1 &= H_1(\zeta) \\
\mathrm{w}_2 &= H_2(\zeta).
\end{aligned} \tag{2.26}
$$

The linear shape functions are defined as

$$
\begin{aligned}
H_1(\zeta) &= \frac{(\zeta_{i+1} - \zeta)}{h_i} \\
H_2(\zeta) &= \frac{(\zeta - \zeta_i)}{h_i} \\
h_i &= \zeta_{i+1} - \zeta_i.
\end{aligned} \tag{2.27}
$$

where i and $i+1$ are the nodes of the i^{th} segment. Substituting Equations (2.25) and (2.26) into

Equation (2.24) and performing the integration on the i^{th} segment yields

$$I_i = -\mathcal{M}_e \left\{ \begin{array}{c} \dot{\Theta}_i^* \\ \dot{\Theta}_{i+1}^* \end{array} \right\} + \mathcal{K}_e \left\{ \begin{array}{c} \Theta_i^* \\ \Theta_{i+1}^* \end{array} \right\} + \mathcal{F}_{2e} \frac{dW^*}{d\tau} \tag{2.28}$$

where

$$\begin{aligned} \mathcal{M}_e &= \int_{\zeta_i}^{\zeta_{i+1}} \left\{ \begin{array}{c} H_1 \\ H_2 \end{array} \right\} \left[\begin{array}{cc} H_1 & H_2 \end{array} \right] d\zeta \\ &= \frac{h_i}{6} \left[\begin{array}{cc} 2 & 1 \\ 1 & 2 \end{array} \right] \end{aligned} \tag{2.29}$$

$$\begin{aligned} \mathcal{K}_e &= -\int_{\zeta_i}^{\zeta_{i+1}} \left(C_{7i} \left\{ \begin{array}{c} H_1' \\ H_2' \end{array} \right\} \left[\begin{array}{cc} H_1' & H_2' \end{array} \right] + \omega_{3i}^2 \left\{ \begin{array}{c} H_1 \\ H_2 \end{array} \right\} \left[\begin{array}{cc} H_1 & H_2 \end{array} \right] \right) d\zeta \\ &= -\frac{C_{7i}}{h_i} \left[\begin{array}{cc} 1 & -1 \\ -1 & 1 \end{array} \right] - \frac{\omega_{3i}^2 h_i}{6} \left[\begin{array}{cc} 2 & 1 \\ 1 & 2 \end{array} \right] \end{aligned} \tag{2.30}$$

$$\begin{aligned} \mathcal{F}_{2e} &= -\int_{\zeta_i}^{\zeta_{i+1}} \omega_{4i}^2 \zeta \left\{ \begin{array}{c} H_1 \\ H_2 \end{array} \right\} d\zeta \\ &= -\frac{\omega_{4i}^2 h_i}{6} \left\{ \begin{array}{c} \zeta_{i+1} + 2\zeta_i \\ 2\zeta_{i+1} + \zeta_i \end{array} \right\} \end{aligned} \tag{2.31}$$

As shown in Equation (2.24), the element integrals are summed to form the expression for I. Since each element has different nodes associated with it, we expand $\mathcal{K}_e$ and $\mathcal{M}_e$ into $(k-1) \times (k-1)$ matrices by adding rows and columns of zeros for all nodes not associated with the current finite element. Similarly, $\mathcal{F}_{2e}$ is expanded into a column vector of size $k+1$ by adding rows of zeros for all nodes not associated with the current finite element. A detailed explanation of this process can be found in [36]. This procedure allows one to sum the resulting element matrices and vectors and is represented by:

$$\mathcal{M} = \sum_e \mathcal{M}_e \tag{2.32}$$

$$\mathcal{K} = \sum_{e} \mathcal{K}_e \tag{2.33}$$

$$\mathcal{F}_2 = \sum_{e} \mathcal{F}_{2e}. \tag{2.34}$$

To obtain the finite element form of Equation (2.24) apply the boundary conditions to node 1 and node $k+1$. This is accomplished by adding the specified boundary conditions to nodes 1 and $k+1$, and adding zeros to all other nodes. The boundary conditions are applied in the following equation through the vector $\mathcal{F}_1$.

$$I = -\mathcal{M}\begin{Bmatrix} \dot{\Theta}_1^* \\ \dot{\Theta}_2^* \\ \vdots \\ \dot{\Theta}_{k+1}^* \end{Bmatrix} + \mathcal{K}\begin{Bmatrix} \Theta_1^* \\ \Theta_2^* \\ \vdots \\ \Theta_{k+1}^* \end{Bmatrix} + \mathcal{F}_1 \frac{4}{mn\pi^2} + \mathcal{F}_2 \frac{dW^*}{d\tau} \tag{2.35}$$

$$\mathcal{F}_1 = \begin{Bmatrix} 0 \\ 0 \\ \vdots \\ \frac{\rho C_w}{\mu(\frac{\cdot}{\cdot})C_w(\frac{\cdot}{\cdot})} \end{Bmatrix} \tag{2.36}$$

Equation (2.35) can be solved by setting $I = 0$; if the number of elements used to discretize Equation (2.24) is large enough, the finite element solution will be a good approximation of the actual solution. Since this problem is properly constrained, the matrices $\mathcal{M}$ and $\mathcal{K}$ are invertible, which allows the problem to be written in a form well known in linear systems theory.

$$\begin{Bmatrix} \dot{\Theta}_1^* \\ \dot{\Theta}_2^* \\ \vdots \\ \dot{\Theta}_{k+1}^* \end{Bmatrix} - \mathcal{A}\begin{Bmatrix} \Theta_1^* \\ \Theta_2^* \\ \vdots \\ \Theta_{k+1}^* \end{Bmatrix} = \mathcal{B}\begin{Bmatrix} \frac{4}{mn\pi^2} \\ \frac{dW^*}{d\tau} \end{Bmatrix} \tag{2.37}$$

with

$$\mathcal{A} = \mathcal{M}^{-1}\mathcal{K} \tag{2.38}$$

$$\mathcal{B} = \mathcal{M}^{-1}\begin{bmatrix} \mathcal{F}_1 & \mathcal{F}_2 \end{bmatrix}. \tag{2.39}$$

The solution to Equation (2.37) is obtained using the variation of parameters method [37], and is given by

$$\begin{Bmatrix} \Theta_1^*(\tau) \\ \Theta_2^*(\tau) \\ \vdots \\ \Theta_{k+1}^*(\tau) \end{Bmatrix} = \frac{4}{mn\pi^2}\mathcal{A}^{-1}\left[\exp(\mathcal{A}\tau) - I\right]\mathcal{B}_1 - \int_0^{\tau} \exp(\mathcal{A}(\tau - \hat{\tau}))\,\mathcal{B}_2 \frac{dW^*}{d\hat{\tau}}d\hat{\tau} \tag{2.40}$$

where I is the identity matrix of dimension $(k+1) \times (k+1)$, and the set of initial conditions is, $\Theta_i^*(\tau) = 0$ for $i = 1 \ldots k+1$. At steady-state this reduces to

$$\begin{Bmatrix} \Theta_1^*(\tau) \\ \Theta_2^*(\tau) \\ \vdots \\ \Theta_{k+1}^*(\tau) \end{Bmatrix} = \frac{4}{mn\pi^2}\mathcal{A}^{-1}\left[\exp(\mathcal{A}\tau) - I\right]\mathcal{B}_1 \tag{2.41}$$

Substituting Equation (2.40) into Equation (2.17), and performing the integration yields

$$\frac{d^2W^*}{d\tau^2} + \omega_1^4 B^4 W^* = -B^4 \int_0^{\tau} G(\tau - \hat{\tau})\frac{dW^*}{d\hat{\tau}}d\hat{\tau} + \Phi(\tau) \tag{2.42}$$

with the conditions

$$W^* = 0; \qquad \frac{dW^*}{d\tau} = 0 \qquad (\tau = 0) \tag{2.43}$$

where

$$G(\tau) = F \cdot \exp(\mathcal{A}(\tau))\,\mathcal{B}_2 \tag{2.44}$$

$$F = -\sum_e \frac{\omega_{2i}^2 h_i}{6}\left\{ \zeta_{i+1} + 2\zeta_i \quad 2\zeta_{i-1} + \zeta_i \right\} \tag{2.45}$$

$$\Phi(\tau) = \frac{4B^4}{mn\pi^2} F \cdot \mathcal{A}^{-1}\left[I - \exp(\mathcal{A}\tau)\right]\mathcal{B}_1 \tag{2.46}$$

For a complete derivation of Equation (2.42) see Appendix A. Equation (2.42) has a form similar to that of the integro-differential equation governing the non-dimensional plate deflection found in [12]. Since $|G(\tau - \hat{\tau})| \ll \omega_1^4$, the Method of Averaging [38] may be applied to Equation (2.42), subject to conditions (2.43). This yields the following approximation

$$\begin{aligned} W^* &= \frac{4}{mn\pi^2\omega_1^4} F \cdot \left\langle \left\{ \exp(-\alpha_1 \tau) \left[\omega_1^2 B^2 \sin\left(\left(\omega_1^2 B^2 + \alpha_2 \right) \tau \right) I \right. \right. \right. \\ &\quad \left. - \cos\left(\left(\omega_1^2 B^2 + \alpha_2 \right) \tau \right) \mathcal{A} \right] + \mathcal{A} \exp(\mathcal{A}\tau) \right\} \left(\mathcal{A}^2 - \omega_1^4 B^4 I \right)^{-1} \\ &\quad \left. + \mathcal{A}^{-1} \left(I - \exp(\mathcal{A}\tau) \right) \right\rangle \mathcal{B}_1 \end{aligned} \tag{2.47}$$

where

$$\alpha_1 = -\frac{B^4}{2} F \cdot \left(\mathcal{A}^2 + \omega_1^4 B^4 I \right)^{-1} \mathcal{A}\mathcal{B}_2 \tag{2.48}$$

$$\alpha_2 = \frac{\omega_1^2 B^6}{2} F \cdot \left(\mathcal{A}^2 + \omega_1^4 B^4 I \right)^{-1} \mathcal{B}_2 \tag{2.49}$$

For a complete derivation of Equation (2.47) see Appendix A. Applying the inversion formulas (2.15) and (2.16) to Equation (2.47) yields the solution for the deflection, W, of a symmetrically laminated, cross-ply, composite plate subject to a thermal shock applied at the upper surface. The solution may be separated into a quasistatic deflection, W_{st}, and a dynamic deflection, W_d, where

$$W = W_{st} - W_d. \tag{2.50}$$

Here

$$W_{st} = \frac{16}{\pi^2} \sum_{\substack{m=1 \\ m \text{ odd}}}^{\infty} \sum_{\substack{n=1 \\ n \text{ odd}}}^{\infty} \frac{\sin(m\pi\xi)\sin(n\pi\eta)}{mn\omega_1^4} F \cdot \mathcal{A}^{-1} \left(I - \exp(\mathcal{A}\tau) \right) \mathcal{B}_1 \tag{2.51}$$

$$\begin{aligned} W_d &= -\frac{16}{\pi^2} \sum_{\substack{m=1 \\ m \text{ odd}}}^{\infty} \sum_{\substack{n=1 \\ n \text{ odd}}}^{\infty} \frac{\sin(m\pi\xi)\sin(n\pi\eta)}{mn\omega_1^4} F \left\{ \exp(-\alpha_1 \tau) \right. \\ &\quad \times \left[\cos\left(\left(\omega_1^2 B^2 + \alpha_2 \right) \tau \right) \mathcal{A} - \omega_1^2 B^2 \sin\left(\left(\omega_1^2 B^2 + \alpha_2 \right) \tau \right) I \right] \\ &\quad \left. - \mathcal{A} \exp(\mathcal{A}\tau) \right\} \left(\mathcal{A}^2 - \omega_1^4 B^4 I \right)^{-1} \mathcal{B}_1 \end{aligned} \tag{2.52}$$

At steady state the temperature solution is

$$\left\{ \begin{array}{c} \Theta_1(\tau) \\ \Theta_2(\tau) \\ \vdots \\ \Theta_{k+1}(\tau) \end{array} \right\} = \frac{16}{\pi^2} \sum_{m=1}^{\infty} \sum_{n=1}^{\infty} \frac{\sin(m\pi\xi)\sin(n\pi\eta)}{mn} \mathcal{A}^{-1} \left[\exp(\mathcal{A}\tau) - I \right] \mathcal{B}_1 \tag{2.53}$$

For comparison, the solution technique found in [12] was applied to the isotropic equivalents of Equations (2.1), (2.2), (2.6), and (2.7) to yield the steady-state, isotropic, nondimensional, temperature, quasistatic and dynamic deflections:

$$\Theta = \frac{16}{\pi^2} \sum_{m=1}^{\infty} \sum_{n=1}^{\infty} \frac{\sin(m\pi\xi)\sin(n\pi\eta)}{mn} \left\{ \frac{a^2}{h^2} \frac{1 - \exp\left(-\frac{h^2}{a^2}\omega^2\tau\right)}{\omega^2} + 2\sum_{k=1}^{\infty} \frac{(-1)^k \left(1 - \exp\left(-\delta^2\tau\right)\right)}{\delta^2} \cos\left(k\pi\left(\zeta + \frac{1}{2}\right)\right) \right\} \tag{2.54}$$

$$W_{st} = \frac{768\,(1+\nu)}{\pi^4} \sum_{\substack{m=1 \\ m \text{ odd}}}^{\infty} \sum_{\substack{n=1 \\ n \text{ odd}}}^{\infty} \frac{\sin(m\pi\xi)\sin(n\pi\eta)}{mn\omega^2} \sum_{\substack{k=1 \\ k \text{ odd}}}^{\infty} \frac{1 - \exp\left(-\delta^2\tau\right)}{k^2\delta^2} \tag{2.55}$$

$$W_d = -\frac{768\,(1+\nu)}{\pi^4} \sum_{\substack{m=1 \\ m \text{ odd}}}^{\infty} \sum_{\substack{n=1 \\ n \text{ odd}}}^{\infty} \frac{\sin(m\pi\xi)\sin(n\pi\eta)}{mn\omega^2} \sum_{\substack{k=1 \\ k \text{ odd}}}^{\infty} \left\{ \exp\left(-\varepsilon_1\alpha_1\tau\right) \times \frac{\left[\delta^2 \cos\left(\left(\omega^2B^2 + \varepsilon_1\alpha_2\right)\tau\right) - \omega^2B^2 \sin\left(\left(\omega^2B^2 + \varepsilon_1\alpha_2\right)\tau\right)\right] - \delta^2\exp(-\delta^2\tau)}{k^2\left(\delta^4 + \omega^4B^4\right)} \right\} \tag{2.56}$$

where

$$\alpha_1 = \frac{48\omega^4B^4}{\pi^4} \sum_{\substack{k=1 \\ k \text{ odd}}}^{\infty} \frac{\delta^2}{k^4\left(\delta^4 + \omega^4B^4\right)} \tag{2.57}$$

$$\alpha_2 = \frac{48\omega^6B^6}{\pi^4} \sum_{\substack{k=1 \\ k \text{ odd}}}^{\infty} \frac{1}{k^4\left(\delta^4 + \omega^4B^4\right)} \tag{2.58}$$

$$B = \frac{h}{a}\sqrt{\frac{hC_v}{k_T}} \left[\frac{\rho E}{12\left(1-\nu^2\right)}\right]^{\frac{1}{4}} \tag{2.59}$$

$$\varepsilon_1 = (1+\nu)\frac{T_0 E \alpha_T^2}{(1-\nu)\rho C_v} \tag{2.60}$$

$$\delta^2 = \left(\frac{h^2}{a^2}\omega^2 + k^2\pi^2\right) \tag{2.61}$$

$$\omega^2 = \left(m^2 + \frac{a^2}{b^2}n^2\right)\pi^2 \tag{2.62}$$

In Equations (2.55) and (2.56) the summation over k comes from the solution of the isotropic version of the nondimensional thermal differential equation, Equation (2.18), using an infinite cosine series. Comparing Equations (2.51) and (2.52) to Equations (2.55) and (2.56) reveals that the solutions have the same general form. However, in Equations (2.51) and (2.52) the innermost summation on k has been replaced by implied summations resulting from vector inner product multiplications.

Additionally the parameter ε_1 in Equation (2.56) is now embedded in the parameters α_1 and α_2 in Equation (2.52).

An alternate solution method that does not depend on the assumption that $|G(\tau - \hat{\tau})| \ll \omega_1^4$ used by the method of averaging is derived in Appendix A. Figures comparing the two solutions are also presented in Appendix A.

2.3 Numerical Results

To test the validity of this solution technique. Equations (2.51) through (2.53) were applied to a plate 6 inches (in) square. 0.125 inch thick. consisting of four-equal thickness layers of aluminum alloy (*i.e.*. an isotropic plate). The mechanical and thermal properties used can be found in Table 2.1. The response using Equations (2.51) through (2.53) was compared to that obtained using the homogeneous isotropic solution. Equations (2.55) through (2.54). Figures 2.1. 2.2. and 2.3 show a comparison of the displacement per unit heat flux $\left(\frac{\text{in Btu}}{\text{h ft}^2}\right)$ at the center of the plate using the two different solution methods. In the layered solution 24 finite elements were used to approximate the solution of (2.18) whereas. in the homogeneous isotropic solution. the summations on k in Equations (2.55) through (2.54) were truncated at 99. In both cases. the summations on m and n were truncated at 21. Figure 2.1 shows good agreement between the two solution techniques for the quasistatic deflection. W_{st}. Notice that this deflection converges to a steady-state condition very rapidly. Figures 2.2 and 2.3 show a comparison of the dynamic deflection. W_d, for time $t = 0$ and time $t = 10$ seconds. respectively. In both cases. the solutions show very good agreement. This indicates that the frequency and decay rate of the vibrations predicted by the layered solution are the same as those predicted by the homogeneous isotropic solution. and that the solutions do not diverge with time. This result is significant since the parameter α_1 in Equation (2.52) is composed of a product of a row vector. F. a matrix. $\left(\mathcal{A}^2 + \omega_1^4 \mathcal{B}^4 I\right)^{-1} \mathcal{A}$. and a column vector $\mathcal{B}_2$. while the equivalent parameter. $\varepsilon_1\alpha_1$. in the homogeneous isotropic solution. Equation (2.56). is given by an explicit summation. Figures 2.2 and 2.3 also illustrate that the dynamic response is dominated by the first mode response. A comparison of the normalized decay of the dynamic deflection. W_d. for the two solution is shown in Figure 2.4. Again, the two responses are in agreement. The overall decay rate of W_d, which is a summation of the decay of all the plate vibration modes, corresponds to a logarithmic decay of $\exp(-0.0764t)$. Figure 2.5 shows a comparison of the steady-state temperature profiles, $T - T_0$, given by Equations (2.53) and (2.54), at the center of the plate for the case where the plate was subjected to a unit heat flux. These results, presented in Figures 2.1 through 2.5, indicate that the solution technique is valid and that it reduces to the homogeneous isotropic solution when all layers of the plate are composed of the same isotropic material.

Table 2.1: Mechanical and Thermal Properties of Aluminum Alloy

Mechanical [39]		**Thermal [40]**	
Young's Modulus	$10.3 \times 10^6 \frac{\text{lb}}{\text{in}^2}$	Conductivity	$130 \frac{\text{Btu}}{\text{h ft} \cdot \text{F}}$
Poisson's Ratio	0.334	Expansion Coefficient	$14 \times 10^{-6} \frac{\text{in}}{\text{in} \cdot \text{F}}$
Density	$3.046 \times 10^{-3} \frac{\text{slug}}{\text{in}^3}$	Specific Heat	$6.885 \frac{\text{Btu}}{\text{slug} \cdot \text{F}}$

Equations (2.51) through (2.53) were then applied to a graphite-epoxy laminate, four-layer, 0/90/90/0 composite plate with the same dimensions as the aluminum plate above. The graphite-epoxy lamina consisted of AS graphite fibers, 70% by weight, embedded in IMLS epoxy resin, with 0% void content. The material and thermal properties of the lamina were calculated using the equations found in [41], and are listed in Table 2.2. The solution for the composite plate used the same number of finite elements and summation limits on m and n as those for the aluminum alloy plate described above. Figures 2.6 and 2.7 show the displacement per unit heat flux $\left(\frac{\text{in h ft}^2}{\text{Btu}}\right)$ at the center of the composite plate. Figure 2.6 illustrates the quasistatic response, while Figure 2.7 shows the dynamic response. Figure 2.8 shows the normalized decay in the amplitude of the dynamic deflection. The overall decay rate of W_d corresponds to a logarithmic decay of $\exp(-8.468 \cdot 10^{-6}t)$. Comparison of Figures 2.1 and 2.6 indicates that the two materials have nearly the same overall response, but very different time constants and steady-state deflection. The difference in time constant can be attributed primarily to the difference in thermal conductivity in the z direction. For aluminum $k_z = 130 \frac{\text{Btu}}{\text{h ft} \cdot \text{F}}$, while for the graphite-epoxy composite $k_z = 0.392 \frac{\text{Btu}}{\text{h ft} \cdot \text{F}}$. Thus, k_z

for the graphite-epoxy composite is more than a factor of $\frac{1}{300}$ times smaller. which corresponds to the difference in the time taken to reach steady-state quasistatic deflection. The difference in the steady-state deflection cannot be attributed solely to a difference in stiffness between the two plates as the effective stiffness of the first mode is very similar in both plates. This can be seen by comparing the frequencies of the dynamic responses in Figures 2.2 and 2.7. The difference in the magnitude of the quasistatic deflection is mainly due to differences in the applied thermal moments which depend on the steady-state temperature distribution and the thermal expansion coefficients (see Equation (2.5)). Figures 2.5 and 2.9 are the steady-state temperature profiles. $T - T_0$. at the center of the plate for the aluminum and composite plate subject to a unit heat flux. respectively. The thermal moments based on these temperature profiles are shown in Table 2.3. As can be seen. the thermal moments in the composite plate are at least an order of magnitude larger. thus supporting the previous statement. The increased temperature at steady state in the composite case is mainly due to the reduced conductivity. At steady state the plate can dissipate heat only at the periphery. Therefore. the lower conductivities in the x and y directions limit the rate at which heat can be dissipated: this leads to an overall higher steady-state temperature.

Table 2.2: Mechanical and Thermal Properties of a Graphite-Epoxy Lamina

Mechanical		**Thermal**	
Elastic Moduli		Conductivities	
E_{11}	$19.72 \times 10^6 \frac{\text{lb}}{\text{in}^2}$	k_{11}	$30.5 \frac{\text{Btu}}{\text{h ft }^\circ\text{F}}$
E_{22}, E_{33}	$1.236 \times 10^6 \frac{\text{lb}}{\text{in}^2}$	k_{22}, k_{33}	$0.392 \frac{\text{Btu}}{\text{h ft }^\circ\text{F}}$
G_{12}	$0.641 \times 10^6 \frac{\text{lb}}{\text{in}^2}$		
Poisson's Ratios		Expansion Coefficients	
ν_{12}	0.278	α_{11}	$-1.028 \times 10^{-8} \frac{\text{in}}{\text{in }^\circ\text{F}}$
ν_{21}	0.017	α_{22}, α_{33}	$2.097 \times 10^{-5} \frac{\text{in}}{\text{in }^\circ\text{F}}$
Density		Specific Heat	
ρ	$1.763 \times 10^{-3} \frac{\text{slug}}{\text{in}^3}$	C_v	$6.917 \frac{\text{Btu}}{\text{slug }^\circ\text{F}}$

Table 2.3: Comparison of the Steady-State Thermal Moments at the Center of the Plate

Thermal Moment	Aluminum	Composite
m_{T_x}	$1.188 \times 10^{-5} \frac{\text{in lb}}{\text{in}}$	$1.658 \times 10^{-4} \frac{\text{in lb}}{\text{in}}$
m_{T_y}	$1.188 \times 10^{-5} \frac{\text{in lb}}{\text{in}}$	$4.172 \times 10^{-4} \frac{\text{in lb}}{\text{in}}$

Comparison of Figures 2.2 through 2.7 indicates that the two materials have similar dynamic responses. The main differences are that the composite response appears to consist of a summation of multiple frequency sinusoids whereas the isotropic response appears to be a single frequency sinusoid. Additionally, the magnitude of the oscillation in the composite response is smaller than that in the aluminum alloy response. In the composite plate $D_{22} < D_{11}$ so that the second mode is much closer in frequency to the first mode when compared to the aluminum plate. Therefore, the thermal shock excites the second mode in the composite plate more than it excites the second mode in the aluminum plate as is indicated by the slightly different responses. The difference in the magnitude of the dynamic responses is due to the reduced thermal conductivity, k_z, of the composite plate. Since the plate vibration is excited by $\frac{\partial}{\partial t}\left(\frac{\partial^2 m_{T_x}}{\partial x^2} + \frac{\partial^2 m_{T_y}}{\partial y^2}\right)$, the reduced conductivity decreases the effect of the thermal shock, resulting in a lower amplitude vibration. The different normalized decay rates in the dynamic deflections, as seen in Figures 2.4 and 2.8, are also due to the reduced conductivities, (k_x, k_y, and k_z) of the composite plate. The smaller value for k_z in the composite plate reduces the coupling between the strain and temperature fields. As mentioned above, the smaller values for k_x and k_y limit the ability of the plate to dissipate heat, including the heat generated by the vibration. These two effects lead to a drastically smaller value for the thermomechanical damping in the composite plate when compared to the aluminum plate.

2.4 Summary

A solution was presented for the dynamic response of a symmetric, cross-ply, laminated composite plate subject to a thermal shock. The solution was validated by using it to determine the response of a homogeneous isotropic plate and comparing it to the response obtained from a solution derived for homogeneous isotropic plates. Comparison of the solutions indicates that they have a very similar form. The main difference is that an explicit summation in the isotropic solution has been replaced by implied summations resulting from vector inner product multiplications in the composite solution.

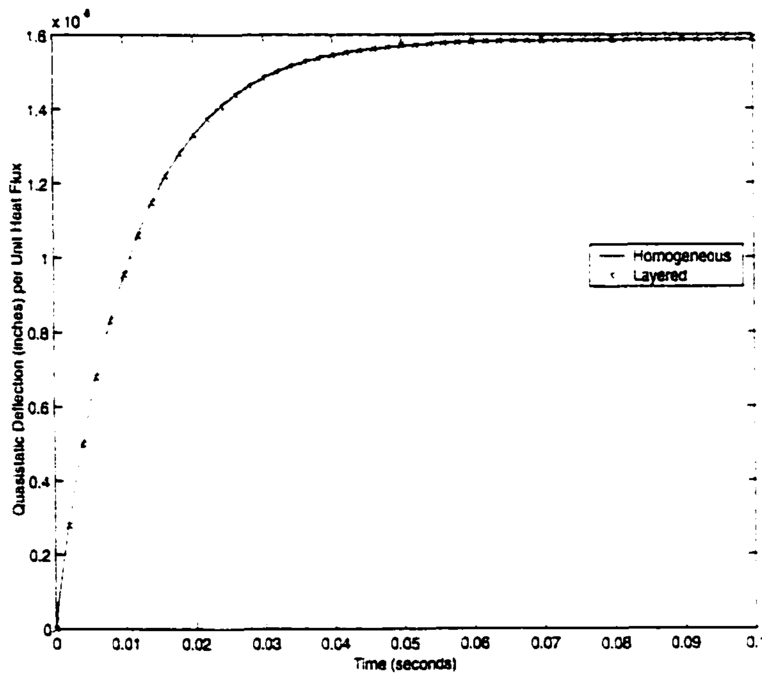

Figure 2.1: Comparison of homogeneous and layered solutions: quasistatic deflection (in) per unit heat flux $\left(\frac{\mathrm{Btu}}{\mathrm{h\,ft^2}}\right)$ at the plate center.

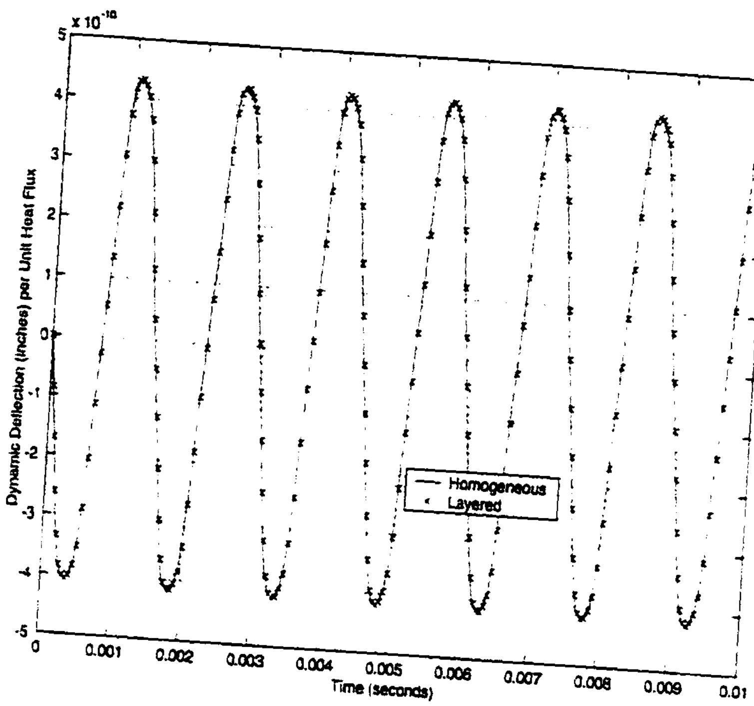

Figure 2.2: Comparison of homogeneous and layered solutions: dynamic deflection (in) per unit heat flux $\left(\frac{\text{Btu}}{\text{h ft}^2}\right)$ at the plate center starting at time zero.

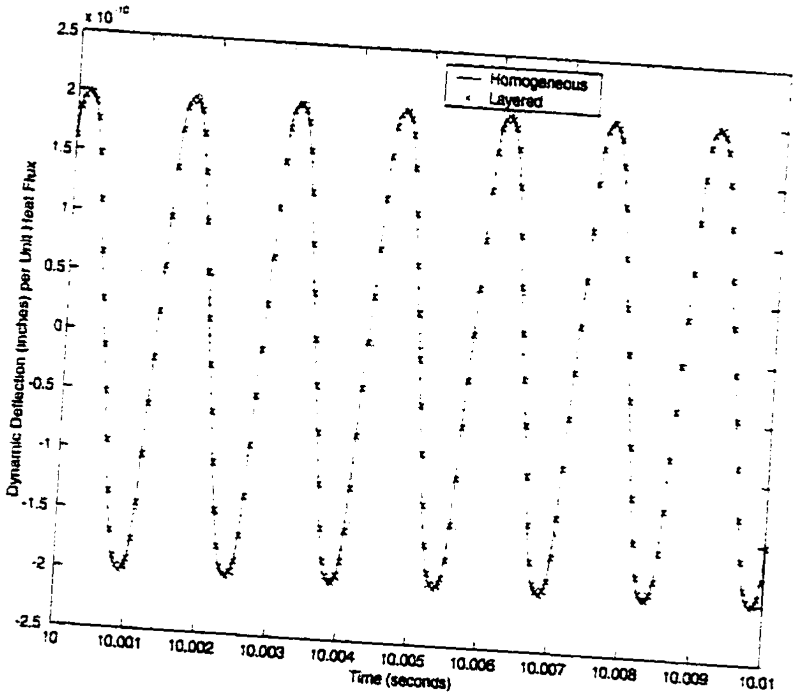

Figure 2.3: Comparison of homogeneous and layered solutions: dynamic deflection (in) per unit heat flux $\left(\frac{\text{Btu}}{\text{h ft}^2}\right)$ at the plate center starting at time 10 seconds.

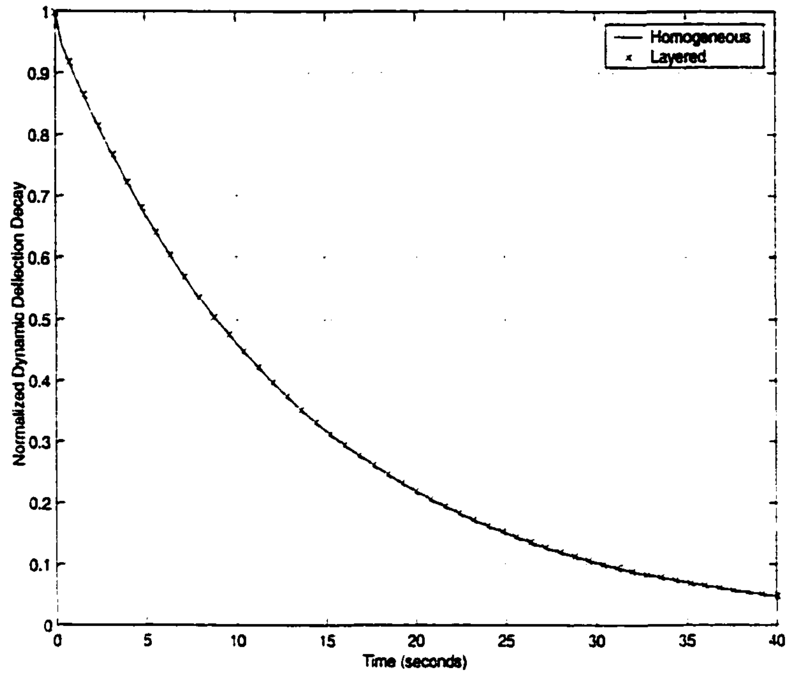

Figure 2.4: Comparison of homogeneous and layered solutions: normalized decay in the amplitude of the dynamic deflection W_d.

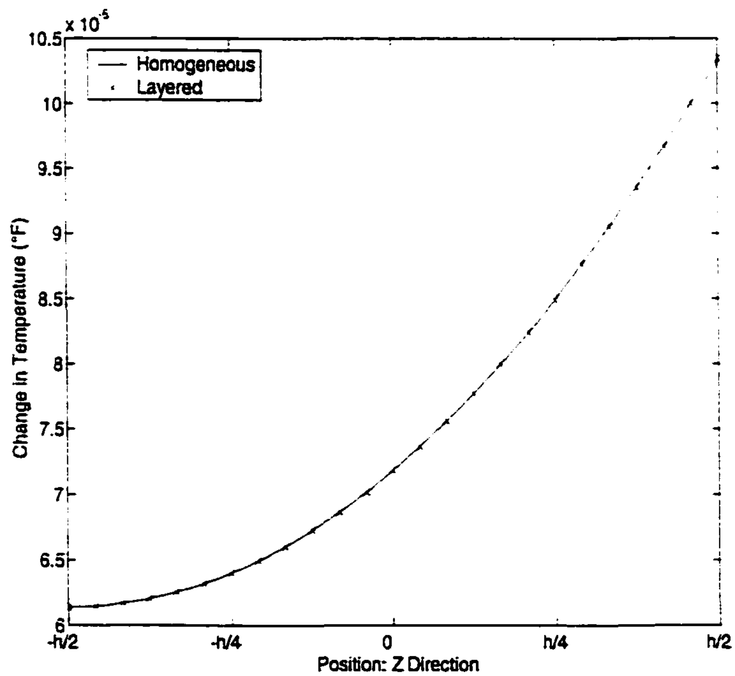

Figure 2.5: Comparison of homogeneous and layered solutions: steady state temperature profile: $T - T_0$ (°F), vs. z at the center of the plate for a unit heat flux $\left(\frac{\text{Btu}}{\text{h ft}^2}\right)$.

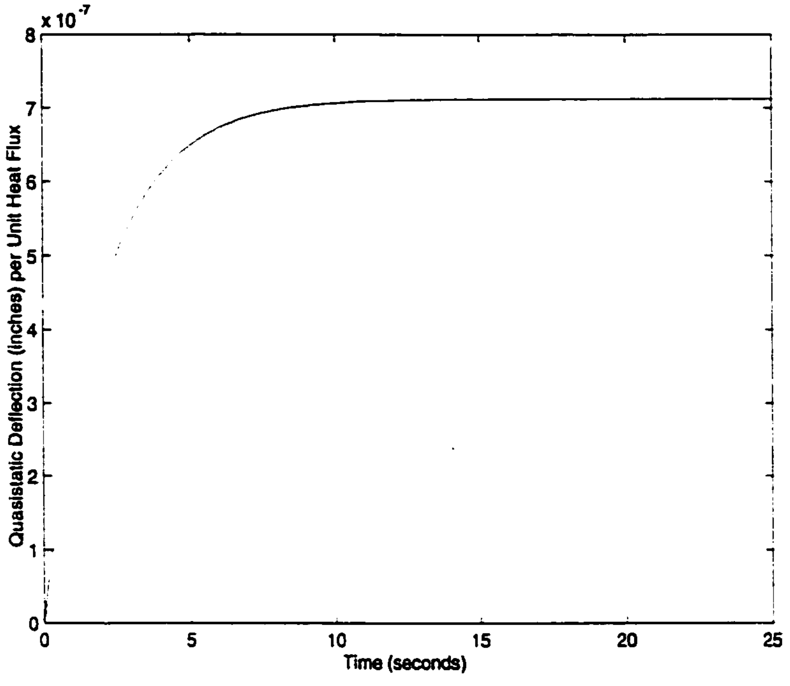

Figure 2.6: Graphite-epoxy composite plate quasistatic deflection (in) per unit heat flux $\left(\frac{\text{Btu}}{\text{h ft}^2}\right)$ at the plate center.

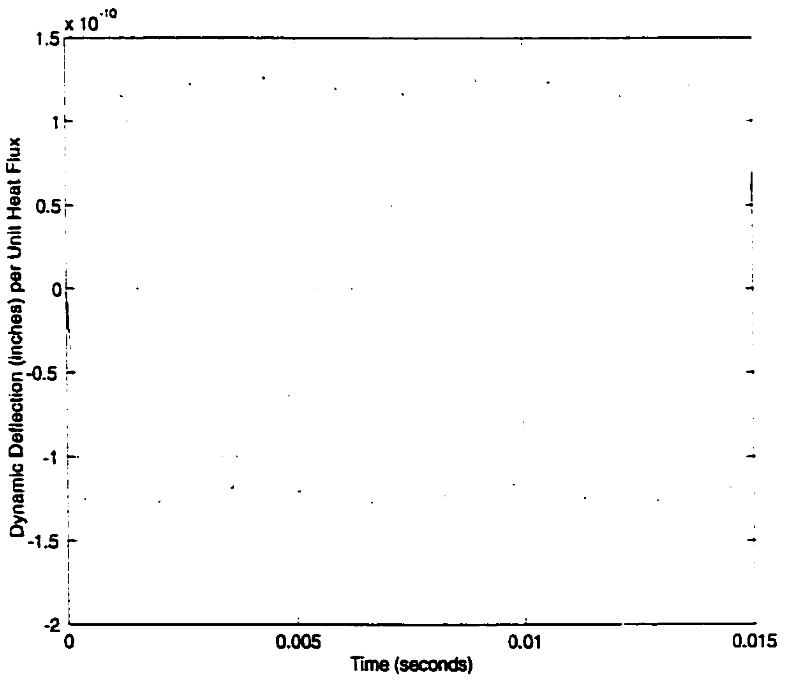

Figure 2.7: Graphite-epoxy composite plate dynamic deflection (in) per unit heat flux $\left(\frac{\text{Btu}}{\text{h ft}^2}\right)$ at the plate center starting at time zero.

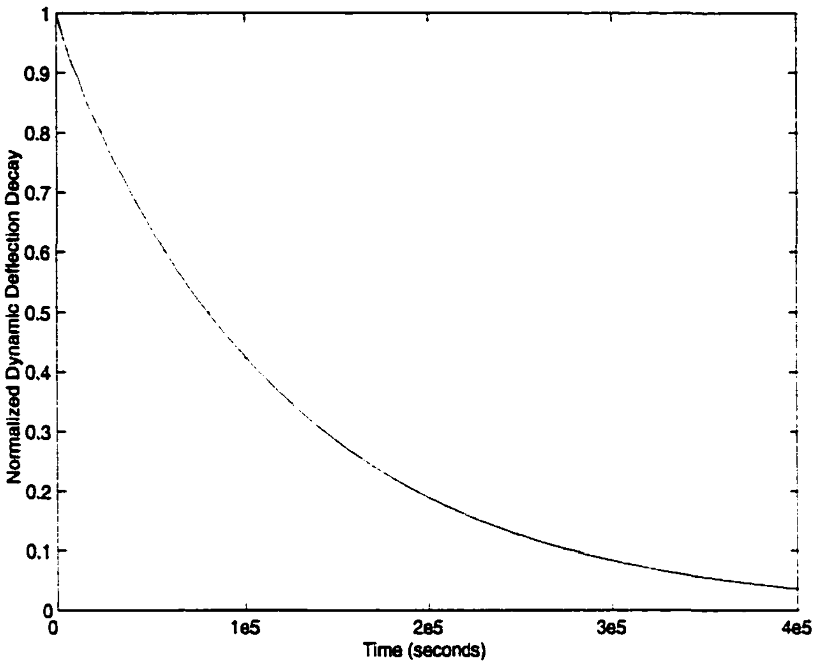

Figure 2.8: Graphite-epoxy composite plate normalized decay of the dynamic deflection, W_d, amplitude.

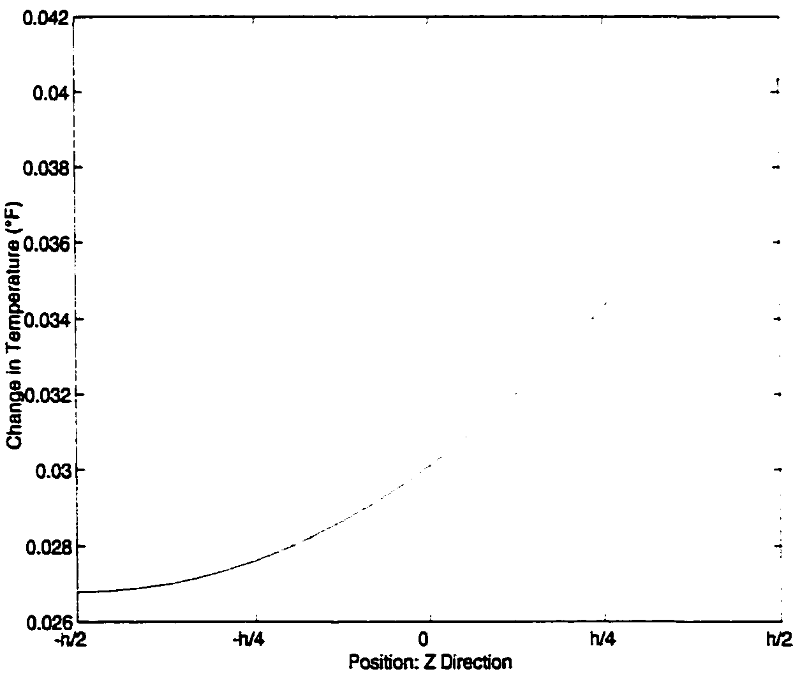

Figure 2.9: Steady state temperature profile: $T - T_0$ (°F), vs. z at the center of the graphite-epoxy plate for a unit heat flux $\left(\frac{\text{Btu}}{\text{h ft}^2}\right)$.

CHAPTER 3

MODELING

3.1 Introduction

In Chapter 2, an analytical solution based on modal expansion and Classical Laminated Plate Theory (CLPT) was derived for the response of a simply supported thin composite plate subjected to a thermal impact. From a "Smart Structure" perspective, this solution represents the open loop response of the system. In this chapter, a model of an orthotropic composite plate with piezoelectric sensors and actuators that can be excited by mechanical or thermal loading is developed. This model does not include the differential equation governing the electric displacement associated with the piezoelectric elements, but includes the pyroelectric effect in the piezoelectric sensor equations, and the inverse pyroelectric effect in the piezoelectric actuator equations. This model is derived using finite elements to discretize both the displacement and the thermal governing equations. One major advantage of a finite element model over a modal expansion model is that it is suitable for any set of boundary conditions. The model is based on a first-order shear deformable theory and can be used to determine the in-plane responses, $u(t)$ and $v(t)$, the out-of-plane response, $w(t)$, as well as the non-dimensional thermal response, Θ. The stresses due to thermal and mechanical loads can be calculated using the displacement and thermal fields.

3.2 Finite Element Smart Plate Model

This section develops a finite element model of an orthotropic composite smart plate that is suitable for closed-loop control system design. It starts with the lamina constitutive relations for a piezothermoelastic material, presents the strain-displacement relations of a first-order shear theory, and then derives the laminate coupled thermo-elastic partial differential equations. These equations are subsequently converted to a set of coupled first-order ordinary differential equations using finite element methods.

3.2.1 Lamina Constitutive Relations

The k^{th} layer orthotropic lamina constitutive relations relative to the principal material axes $(1,2,3)$ of the lamina are

$$\{\hat{\sigma}\}^k = [C]^k \left(\{\hat{\varepsilon}\}^k - \{\hat{\alpha}\}^k [T]^k - \left([d]^k\right)^T \{E\}^k \right) \tag{3.1}$$

$$\{D\}^k = [e]^k \{\hat{\varepsilon}\}^k + [\epsilon]^k \{E\}^k - \{\hat{p}\}^k \Theta^k \tag{3.2}$$

where $\{\hat{\sigma}\}^k$ is the stress vector, $[C]^k$ is the elastic stiffness matrix, $\{\hat{\varepsilon}\}^k$ is the strain vector, $\{\hat{\alpha}\}^k$ is the thermal expansion coefficient vector, Θ^k is the temperature measured from the strain-free temperature, $[d]^k$ is the piezoelectric strain matrix, $\{E\}^k$ is the electric field vector, $\{D\}^k$ is the electric displacement vector, $[e]^k = [d]^k [C]^k$ is the piezoelectric stress matrix, $[\epsilon]^k$ is the permittivity matrix, and $\{\hat{p}\}^k$ is the pyroelectric coefficient vector. The superscript T represents the transpose operation. These parameters take the following forms:

$$\{\hat{\sigma}\}^k = [\sigma_1 \quad \sigma_2 \quad \sigma_3 \quad \tau_{23} \quad \tau_{31} \quad \tau_{12}]^T \tag{3.3}$$

$$\{\hat{\varepsilon}\}^k = [\varepsilon_1 \quad \varepsilon_2 \quad \varepsilon_3 \quad \gamma_{23} \quad \gamma_{31} \quad \gamma_{12}]^T \tag{3.4}$$

$$\{\hat{\alpha}\}^k = [\alpha_1 \quad \alpha_2 \quad \alpha_3 \quad 0 \quad 0 \quad 0]^T \tag{3.5}$$

$$\{E\}^k = [E_1 \quad E_2 \quad E_3]^T \tag{3.6}$$

$$\{D\}^k = [D_1 \quad D_2 \quad D_3]^T \tag{3.7}$$

$$\{\hat{p}\}^k = [p_1 \quad p_2 \quad p_3]^T \tag{3.8}$$

$$[C]^k = \begin{bmatrix} C_{11} & C_{12} & C_{13} & 0 & 0 & 0 \\ C_{12} & C_{22} & C_{23} & 0 & 0 & 0 \\ C_{13} & C_{23} & C_{33} & 0 & 0 & 0 \\ 0 & 0 & 0 & C_{44} & 0 & 0 \\ 0 & 0 & 0 & 0 & C_{55} & 0 \\ 0 & 0 & 0 & 0 & 0 & C_{66} \end{bmatrix} \tag{3.9}$$

$$[d]^k = \begin{bmatrix} 0 & 0 & 0 & 0 & d_{15} & 0 \\ 0 & 0 & 0 & d_{24} & 0 & 0 \\ d_{31} & d_{32} & d_{33} & 0 & 0 & 0 \end{bmatrix} \tag{3.10}$$

$$[\epsilon]^k = \begin{bmatrix} \epsilon_{11} & 0 & 0 \\ 0 & \epsilon_{22} & 0 \\ 0 & 0 & \epsilon_{33} \end{bmatrix} \tag{3.11}$$

For the case where the electric field is applied only along the 3^{rd} axis. the last term in Equation (3.1). known as the piezoelectric strain. can be written as

$$\begin{aligned} \{\bar{\varepsilon}\}_p^k &= \left([d]^k\right)^T \{E\}^k \\ \{\bar{\varepsilon}\}_p^k &= \begin{bmatrix} 0 & 0 & d_{31} \\ 0 & 0 & d_{32} \\ 0 & 0 & d_{33} \\ 0 & d_{24} & 0 \\ d_{15} & 0 & 0 \\ 0 & 0 & 0 \end{bmatrix} \begin{Bmatrix} 0 \\ 0 \\ E_3^k \end{Bmatrix} \\ &= E_3^k \{d\}^k \end{aligned} \tag{3.12}$$

$$\{d\}^k = [d_{31} \quad d_{32} \quad d_{33} \quad 0 \quad 0 \quad 0]^T \tag{3.13}$$

Substituting Equation (3.12) into Equation (3.1) yields

$$\{\bar{\sigma}\}^k = [C]^k \left(\{\bar{\varepsilon}\}^k - \{\bar{\alpha}\}^k T^k - E_3^k \{d\}^k\right) \tag{3.14}$$

Equation (3.14) is referenced with respect to the principal material axes. In order to incorporate the k^{th} layer into the laminate. it is necessary to transform Equation (3.14) into the laminate x. y. and z axes. This can be accomplished using the following formulas [42]

$$\{\bar{\sigma}\}^k = [T]^k \{\sigma\}^k \tag{3.15}$$

$$\{\bar{\varepsilon}\}^k = [R][T]^k [R]^{-1} \{\varepsilon\}^k \tag{3.16}$$

where

$$
\begin{aligned}
\{\sigma\}^k &= [\sigma_x \quad \sigma_y \quad \sigma_z \quad \tau_{yz} \quad \tau_{zx} \quad \tau_{xy}]^T && (3.17)\\
\{\varepsilon\}^k &= [\varepsilon_x \quad \varepsilon_y \quad \varepsilon_z \quad \gamma_{yz} \quad \gamma_{zx} \quad \gamma_{xy}]^T && (3.18)\\
\{\alpha\}^k &= [\alpha_x \quad \alpha_y \quad \alpha_z \quad 0 \quad 0 \quad \alpha_{xy}]^T && (3.19)
\end{aligned}
$$

$$
[T]^k = \begin{bmatrix} (c\theta)^2 & (s\theta)^2 & 0 & 0 & 0 & 2c\theta s\theta \\ (s\theta)^2 & (c\theta)^2 & 0 & 0 & 0 & -2c\theta s\theta \\ 0 & 0 & 1 & 0 & 0 & 0 \\ 0 & 0 & 0 & c\theta & -s\theta & 0 \\ 0 & 0 & 0 & s\theta & c\theta & 0 \\ -c\theta s\theta & c\theta s\theta & 0 & 0 & 0 & (c\theta)^2-(s\theta)^2 \end{bmatrix} \qquad (3.20)
$$

$$
c\theta = \cos(\theta_k) \qquad (3.21)
$$

$$
s\theta = \sin(\theta_k) \qquad (3.22)
$$

$$
R = \begin{bmatrix} 1 & 0 & 0 & 0 & 0 & 0 \\ 0 & 1 & 0 & 0 & 0 & 0 \\ 0 & 0 & 1 & 0 & 0 & 0 \\ 0 & 0 & 0 & 2 & 0 & 0 \\ 0 & 0 & 0 & 0 & 2 & 0 \\ 0 & 0 & 0 & 0 & 0 & 2 \end{bmatrix} \qquad (3.23)
$$

where $\{\sigma\}^k$ and $\{\varepsilon\}^k$ are defined with reference to the laminate axes. and θ_k is the angle measured from the x axis of the laminate to the 1 axis of the lamina. Using these transformations. one can write Equation (3.14) as

$$
\{\sigma\}^k = [\bar{C}]^k \left(\{\varepsilon\}^k - \{\alpha\}^k T^k\right) - [\hat{C}]^k \left(E_3^k \{d\}^k\right) \qquad (3.24)
$$

$$
[\bar{C}]^k = \left([T]^k\right)^{-1} [C]^k [R] [T]^k [R]^{-1} \qquad (3.25)
$$

$$
[\hat{C}]^k = \left([T]^k\right)^{-1} [C]^k \qquad (3.26)
$$

For a generally anisotropic material, the equations relating the heat flow to the temperature gradient in Cartesian tensor notation are [43]

$$-q_i = k_{ij}\frac{\partial \Theta}{\partial x_j} \qquad i,j = 1,2,3 \tag{3.27}$$

where q_i is the heat flow in the x_i direction, Θ is the temperature change from the nominal stress free temperature, and k_{ij} is the ij^{th} entry of the thermal conductivity tensor. For an orthotropic material, such as a uniaxial fiber reinforced composite lamina, Equations (3.27) become

$$\begin{aligned} -q_1 &= k_{11}\frac{\partial \Theta}{\partial x_1} \\ -q_2 &= k_{22}\frac{\partial \Theta}{\partial x_2} \\ -q_3 &= k_{33}\frac{\partial \Theta}{\partial x_3} \end{aligned} \tag{3.28}$$

where x_1 is aligned with the fiber, x_2 is in the plane of the lamina and normal to the fibers, and x_3 is normal to the lamina. Equation (3.28) is referenced with respect to the principal material axes. In order to incorporate the lamina into a complete laminate, it is necessary to transform Equation (3.28) into the laminate x, y, and z axes. This is accomplished using the following second order tensor transformation formula [42]

$$\begin{aligned} k'_{ij} &= a_{ik}a_{jl}k_{kl} \qquad i,j,k,l = 1,2,3 \\ a_{ij} &= \cos(x'_i, x_j) \end{aligned} \tag{3.29}$$

where a_{ij} is the direction cosine between the i^{th} direction in the x'_1, x'_2, x'_3 system and the j^{th} direction in the x_1, x_2, x_3 system. For a rotation θ about the x_3 axis, the direction cosine matrix is

$$[a_{ij}] = \begin{bmatrix} \cos(\theta) & \sin(\theta) & 0 \\ -\sin(\theta) & \cos(\theta) & 0 \\ 0 & 0 & 1 \end{bmatrix} \tag{3.30}$$

Letting the primed system represent the laminate axes and the unprimed system represent the lamina principal axes, the thermal conductivity tensor for the laminate x, y, and z axes is

$$[k_{ij}] = \begin{bmatrix} k_x & k_{xy} & 0 \\ k_{xy} & k_y & 0 \\ 0 & 0 & k_z \end{bmatrix} \tag{3.31}$$

where

$$k_x = k_{11}\cos^2(\theta) + k_{22}\sin^2(\theta) \tag{3.32}$$

$$k_{xy} = -k_{11}\cos(\theta)\sin(\theta) + k_{22}\cos(\theta)\sin(\theta) \tag{3.33}$$

$$k_y = k_{11}\sin^2(\theta) + k_{22}\cos^2(\theta) \tag{3.34}$$

$$k_z = k_{33} \tag{3.35}$$

The equations that define the thermo-mechanical constants of a generally anisotropic material in Cartesian tensor notation are [33]

$$\beta_{ij} = \alpha_{kl}C_{ijkl} \qquad i,j,k,l = 1,2,3 \tag{3.36}$$

where β_{ij} are the thermo-mechanical coupling coefficients, α_{kl} are the thermal expansion coefficients, and C_{ijkl} are the elastic stiffness coefficients. For an orthotropic lamina in the principal axes using full and reduced notation, as well as symmetry of the stiffness coefficients, Equation (3.36) yields

$$\begin{aligned} \beta_{11} &= \alpha_{11}C_{1111} + \alpha_{22}C_{1122} + \alpha_{33}C_{1133} \\ &= \alpha_1 C_{11} + \alpha_2 C_{12} + \alpha_3 C_{13} \end{aligned} \tag{3.37}$$

$$\begin{aligned} \beta_{12} &= \alpha_{11}C_{1211} + \alpha_{22}C_{1222} + \alpha_{33}C_{1233} \\ &= \alpha_1 C_{16} + \alpha_2 C_{26} + \alpha_3 C_{36} \\ &= 0 \end{aligned} \tag{3.38}$$

$$\begin{aligned} \beta_{13} &= \alpha_{11}C_{1311} + \alpha_{22}C_{1322} + \alpha_{33}C_{1333} \\ &= \alpha_1 C_{15} + \alpha_2 C_{25} + \alpha_3 C_{35} \\ &= 0 \end{aligned} \tag{3.39}$$

$$\beta_{21} = \beta_{12} = 0 \tag{3.40}$$

$$\begin{aligned}
\beta_{22} &= \alpha_{11}C_{2211} + \alpha_{22}C_{2222} - \alpha_{33}C_{2233} \\
&= \alpha_1 C_{12} + \alpha_2 C_{22} + \alpha_3 C_{23}
\end{aligned} \tag{3.41}$$

$$\begin{aligned}
\beta_{23} &= \alpha_{11}C_{2311} - \alpha_{22}C_{2322} - \alpha_{33}C_{2333} \\
&= \alpha_1 C_{14} - \alpha_2 C_{24} - \alpha_3 C_{34} \\
&= 0
\end{aligned} \tag{3.42}$$

$$\beta_{31} = \beta_{13} = 0 \tag{3.43}$$

$$\beta_{32} = \beta_{23} = 0 \tag{3.44}$$

$$\begin{aligned}
\beta_{33} &= \alpha_{11}C_{3311} - \alpha_{22}C_{3322} - \alpha_{33}C_{3333} \\
&= \alpha_1 C_{13} - \alpha_2 C_{23} - \alpha_3 C_{33}
\end{aligned} \tag{3.45}$$

In tensor matrix notation. this is

$$[\beta] = \begin{bmatrix} \beta_{11} & 0 & 0 \\ 0 & \beta_{22} & 0 \\ 0 & 0 & \beta_{33} \end{bmatrix} \tag{3.46}$$

The transformed tensor due to a rotation θ about the $3-axis$ is

$$[\beta'] = \begin{bmatrix} \beta'_{11} & \beta'_{12} & 0 \\ \beta'_{12} & \beta'_{22} & 0 \\ 0 & 0 & \beta'_{33} \end{bmatrix} \tag{3.47}$$

where

$$\beta'_{11} = \beta_{11}\cos^2(\theta) + \beta_{22}\sin^2(\theta) \tag{3.48}$$

$$\beta'_{12} = -\beta_{11}\cos(\theta)\sin(\theta) + \beta_{22}\cos(\theta)\sin(\theta) \tag{3.49}$$

$$\beta'_{22} = \beta_{11}\sin^2(\theta) + \beta_{22}\cos^2(\theta) \tag{3.50}$$

$$\beta'_{33} = \beta_{33} \tag{3.51}$$

For the case where the primed coordinate system is aligned with the laminate x, y, and z axes, these equations indicate that an orthotropic lamina can generate heat only from the terms $\beta_x\dot{\varepsilon}_x$, $\beta_y\dot{\varepsilon}_y$, $\beta_{xy}\dot{\varepsilon}_{xy}$, and $\beta_z\dot{\varepsilon}_z$.

3.2.2 Strain-Displacement Relations

The derivations in this section follow the derivations found in [24]. The first-order shear deformable theory outlined in [44] uses the following displacement field equations

$$\begin{aligned} u(x,y,z,t) &= u^0(x,y,t) + z\psi_x(x,y,t) \\ v(x,y,z,t) &= v^0(x,y,t) + z\psi_y(x,y,t) \\ w(x,y,z,t) &= w^0(x,y,t) \end{aligned} \tag{3.52}$$

where u, v, and w are the displacements in the x, y, and z directions, respectively, u^0, v^0, and w^0 are the displacements in the x, y, and z directions of a point (x,y) on the midplane, respectively, t is time, and ψ_x and ψ_y are the rotations in the xz and yz planes, respectively, as a result of bending only. To simplify the derivations, define the displacement vector and the generalized displacement vector corresponding to the midplane as

$$\{u\} = \begin{bmatrix} u & v & w \end{bmatrix}^T \tag{3.53}$$

$$\{\bar{u}\} = \begin{bmatrix} u^0 & v^0 & w^0 & \psi_x & \psi_y \end{bmatrix}^T \tag{3.54}$$

respectively. Equations (3.52) can then be expressed in matrix notation using (3.53) and (3.54) as

$$\{u\} = \mathcal{G}\{\bar{u}\} \tag{3.55}$$

where

$$\mathcal{G} = \begin{bmatrix} 1 & 0 & 0 & z & 0 \\ 0 & 1 & 0 & 0 & z \\ 0 & 0 & 1 & 0 & 0 \end{bmatrix} \tag{3.56}$$

Substituting Equation (3.52) into the infinitesimal strain equations yields

$$\{\varepsilon\} = \{\varepsilon^0\} + z\{\varkappa\} \tag{3.57}$$

where

$$\{\varepsilon\} = \begin{bmatrix}\varepsilon_x & \varepsilon_y & \varepsilon_z & \gamma_{yz} & \gamma_{xz} & \gamma_{xy}\end{bmatrix}^T \tag{3.58}$$

$$\begin{aligned}\{\varepsilon^0\} &= \begin{bmatrix}\varepsilon_x^0 & \varepsilon_y^0 & 0 & \gamma_{yz}^0 & \gamma_{xz}^0 & \gamma_{xy}^0\end{bmatrix}^T \\ &= \begin{bmatrix}\dfrac{\partial u^0}{\partial x} & \dfrac{\partial v^0}{\partial y} & 0 & \dfrac{\partial w^0}{\partial y} + \psi_y & \dfrac{\partial w^0}{\partial x} + \psi_x & \dfrac{\partial u^0}{\partial y} + \dfrac{\partial v^0}{\partial x}\end{bmatrix}^T\end{aligned} \tag{3.59}$$

$$\begin{aligned}\{\kappa\} &= \begin{bmatrix}\kappa_x & \kappa_y & 0 & 0 & 0 & \kappa_{xy}\end{bmatrix}^T \\ &= \begin{bmatrix}\dfrac{\partial \psi_x}{\partial x} & \dfrac{\partial \psi_y}{\partial y} & 0 & 0 & 0 & \dfrac{\partial \psi_x}{\partial y} + \dfrac{\partial \psi_y}{\partial x}\end{bmatrix}^T\end{aligned} \tag{3.60}$$

In the first-order shear deformable theory, ε_z is usually assumed to be zero and will be ignored in subsequent derivations. To simplify derivations define the generalized strain vector corresponding to the midplane as

$$\{\bar{\varepsilon}\} = \begin{bmatrix}\varepsilon_x^0 & \varepsilon_y^0 & \gamma_{yz}^0 & \gamma_{xz}^0 & \gamma_{xy}^0 & \kappa_x & \kappa_y & \kappa_{xy}\end{bmatrix}^T \tag{3.61}$$

With this notation, the relationship between Equation (3.54) and Equation (3.61) can be written as

$$\{\bar{\varepsilon}\} = \mathcal{L}\{\bar{u}\} \tag{3.62}$$

where $\mathcal{L}$ is a differential operator matrix defined by

$$\mathcal{L} = \begin{bmatrix} \frac{\partial}{\partial x} & 0 & 0 & 0 & 0 \\ 0 & \frac{\partial}{\partial y} & 0 & 0 & 0 \\ 0 & 0 & \frac{\partial}{\partial y} & 0 & 1 \\ 0 & 0 & \frac{\partial}{\partial x} & 1 & 0 \\ \frac{\partial}{\partial y} & \frac{\partial}{\partial x} & 0 & 0 & 0 \\ 0 & 0 & 0 & \frac{\partial}{\partial x} & 0 \\ 0 & 0 & 0 & 0 & \frac{\partial}{\partial y} \\ 0 & 0 & 0 & \frac{\partial}{\partial y} & \frac{\partial}{\partial x} \end{bmatrix} \tag{3.63}$$

3.2.3 Governing Equations

For a symmetric laminate consisting of N layers, with the plane of symmetry at $z = 0$, the laminate constitutive relations, including piezoelectric and thermal effects, but ignoring the normal stress in the z direction, can be written as

$$\{\bar{N}\} = [\mathcal{D}]\{\bar{\varepsilon}\} - \{\bar{N}_P\} - \{\bar{N}_T\} \tag{3.64}$$

where $\{\bar{N}\}$ is the stress and moment resultant vector, $[\mathcal{D}]$ is the generalized stiffness matrix, $\{\bar{N}_P\}$ is the piezoelectric stress and moment resultant vector, and $\{\bar{N}_T\}$ is the thermal stress and moment resultant vector. The definitions of these terms are

$$\{\bar{N}\} = \lfloor N_x \quad N_y \quad Q_y \quad Q_x \quad N_{xy} \quad M_x \quad M_y \quad M_{xy} \rfloor^T \tag{3.65}$$

$$(N_x, N_y, Q_y, Q_x, N_{xy}) = \int_{-\frac{h}{2}}^{\frac{h}{2}} (\sigma_x, \sigma_y, \tau_{yz}, \tau_{xz}, \tau_{xy})\, dz \tag{3.66}$$

$$(M_x, M_y, M_{xy}) = \int_{-\frac{h}{2}}^{\frac{h}{2}} (\sigma_x, \sigma_y, \tau_{xy})\, z dz \tag{3.67}$$

$$[\mathcal{D}] = \begin{bmatrix} A_{11} & A_{12} & 0 & 0 & A_{16} & B_{11} & B_{12} & B_{16} \\ A_{12} & A_{22} & 0 & 0 & A_{26} & B_{12} & B_{22} & B_{26} \\ 0 & 0 & A_{44} & A_{45} & 0 & 0 & 0 & 0 \\ 0 & 0 & A_{45} & A_{55} & 0 & 0 & 0 & 0 \\ A_{16} & A_{26} & 0 & 0 & A_{66} & B_{16} & B_{26} & B_{66} \\ B_{11} & B_{12} & 0 & 0 & B_{16} & D_{11} & D_{12} & D_{16} \\ B_{12} & B_{22} & 0 & 0 & B_{26} & D_{12} & D_{22} & D_{26} \\ B_{16} & B_{26} & 0 & 0 & B_{66} & D_{16} & D_{26} & D_{66} \end{bmatrix} \tag{3.68}$$

$$\begin{aligned} (A_{ij}, B_{ij}, D_{ij}) &= \sum_{k=1}^{N} \int_{z_{k-1}}^{z_k} \bar{C}_{ij}^k \left(1, z, z^2\right) dz \qquad (i, j = 1, 2, 6) \\ A_{ij} &= \sum_{k=1}^{N} \varkappa_i \varkappa_j \int_{z_{k-1}}^{z_k} \bar{C}_{ij}^k dz \qquad (i, j = 4, 5) \\ \varkappa_i^2 &= \frac{5}{6} \end{aligned} \tag{3.69}$$

The values for the shear correction coefficients, $\varkappa_i^2$, depend on the the material properties, see Bert [45]. However, for comparison to previous works, $\varkappa_i^2 = \frac{5}{6}$ will be used [46]. Laminates with a plane of symmetry at $z = 0$ have the same symmetry as a monoclinic homogeneous material. Therefore, they have the same elastic configuration as monoclinic homogeneous materials, which are defined by thirteen independent elastic constants.

The piezoelectric actuator stress and moment resultant vector, $\{\bar{N}_P\}$, is given by

$$\{\bar{N}_P\} = [N_{Px} \quad N_{Py} \quad Q_{Py} \quad Q_{Px} \quad N_{Pxy} \quad M_{Px} \quad M_{Py} \quad M_{Pxy}]^T \tag{3.70}$$

Assuming that there are N_A piezolelectric actuator patches distributed throughout the plate, the expression for N_{Px} is

$$\begin{aligned} N_{Px} &= \sum_{k=1}^{N_A} \left(\hat{C}_{11}^k d_{31}^k - \hat{C}_{12}^k d_{32}^k \right) \int_{z_{k-1}}^{z_k} E_k dz \\ &= \sum_{k=1}^{N_A} \left(\hat{C}_{11}^k d_{31}^k - \hat{C}_{12}^k d_{32}^k \right) V_k \end{aligned} \tag{3.71}$$

Here, the $\hat{C}_{ij}^k$ are the transformed elastic stiffnesses given by Equation (3.14) for the k^{th} piezoelectric actuator, the d_{ij}^k are the piezoelectric strain coefficients for the k^{th} piezoelectric actuator, $V_k = E_k h_k$ is the electric voltage applied across the k^{th} piezoelectric actuator, $h_k = (z_k - z_{k-1})$ is the thickness of the k^{th} piezoelectric actuator, and z_k^0 is the z distance from the midplane of the laminate to the midplane of the k^{th} piezoelectric actuator defined by

$$z_k^0 = \frac{1}{2}(z_k - z_{k-1}) \tag{3.72}$$

The expressions for the remaining elements of $\{\bar{N}_P\}$ are

$$\begin{aligned} N_{Py} &= \sum_{k=1}^{N_A} \left(\hat{C}_{12}^k d_{31}^k - \hat{C}_{22}^k d_{32}^k \right) \int_{z_{k-1}}^{z_k} E_k dz \\ &= \sum_{k=1}^{N_A} \left(\hat{C}_{11}^k d_{31}^k - \hat{C}_{12}^k d_{32}^k \right) V_k \end{aligned} \tag{3.73}$$

$$Q_{Py} = 0 \tag{3.74}$$

$$Q_{Px} = 0 \tag{3.75}$$

$$\begin{aligned} N_{Pxy} &= \sum_{k=1}^{N_A} \left(\hat{C}_{16}^k d_{31}^k - \hat{C}_{26}^k d_{32}^k \right) \int_{z_{k-1}}^{z_k} E_k dz \\ &= \sum_{k=1}^{N_A} \left(\hat{C}_{16}^k d_{31}^k + \hat{C}_{26}^k d_{32}^k \right) V_k \end{aligned} \tag{3.76}$$

$$
\begin{aligned}
M_x^P &= \sum_{k=1}^{N_A} \left(\hat{C}_{11}^k d_{31}^k + \hat{C}_{12}^k d_{32}^k \right) \int_{z_{k-1}}^{z_k} E_k z dz \\
&= \sum_{k=1}^{N_A} \left(\hat{C}_{11}^k d_{31}^k + \hat{C}_{12}^k d_{32}^k \right) (z_k^2 - z_{k-1}^2) E_k \\
&= \sum_{k=1}^{N_A} \left(\hat{C}_{11}^k d_{31}^k - \hat{C}_{12}^k d_{32}^k \right) z_0^k V_k
\end{aligned} \tag{3.77}
$$

$$
\begin{aligned}
M_y^P &= \sum_{k=1}^{N_A} \left(\hat{C}_{12}^k d_{31}^k - \hat{C}_{22}^k d_{32}^k \right) \int_{z_{k-1}}^{z_k} E_k z dz \\
&= \sum_{k=1}^{N_A} \frac{1}{2} \left(\hat{C}_{12}^k d_{31}^k - \hat{C}_{22}^k d_{32}^k \right) (z_k^2 - z_{k-1}^2) E_k \\
&= \sum_{k=1}^{N_A} \left(\hat{C}_{12}^k d_{31}^k - \hat{C}_{22}^k d_{32}^k \right) z_0^k V_k
\end{aligned} \tag{3.78}
$$

$$
\begin{aligned}
M_{xy}^P &= \sum_{k=1}^{N_A} \left(\hat{C}_{16}^k d_{31}^k - \hat{C}_{26}^k d_{32}^k \right) \int_{z_{k-1}}^{z_k} E_k z dz \\
&= \sum_{k=1}^{N_A} \frac{1}{2} \left(\hat{C}_{16}^k d_{31}^k - \hat{C}_{26}^k d_{32}^k \right) (z_k^2 - z_{k-1}^2) E_k \\
&= \sum_{k=1}^{N_A} \left(\hat{C}_{16}^k d_{31}^k + \hat{C}_{26}^k d_{32}^k \right) z_0^k V_k
\end{aligned} \tag{3.79}
$$

These equations can be reformulated so that the voltages across the piezoelectric laminates are available as inputs to the system.

$$
\{\bar{N}_P\} = [P]\{V\} \tag{3.80}
$$

where

$$
\begin{aligned}
[P] &= \begin{bmatrix} P_1 & P_2 & \cdots & P_{N_A} \end{bmatrix} \\
[P_k] &= \begin{bmatrix} \bar{C}_{11}^k d_{31}^k + \bar{C}_{12}^k d_{32}^k \\ \bar{C}_{12}^k d_{31}^k + \bar{C}_{22}^k d_{32}^k \\ 0 \\ 0 \\ \bar{C}_{16}^k d_{31}^k + \bar{C}_{26}^k d_{32}^k \\ \left(\bar{C}_{11}^k d_{31}^k + \bar{C}_{12}^k d_{32}^k\right) z_0^k \\ \left(\bar{C}_{12}^k d_{31}^k + \bar{C}_{22}^k d_{32}^k\right) z_0^k \\ \left(\bar{C}_{16}^k d_{31}^k + \bar{C}_{26}^k d_{32}^k\right) z_0^k \end{bmatrix}
\end{aligned}
\tag{3.81}
$$

$$
\{V\} = \begin{bmatrix} V_1 & V_2 & \cdots & V_{N_A} \end{bmatrix}^T \tag{3.82}
$$

This formulation is required to provide control input to the system since the response will be controlled by the voltages applied to the piezoelectric actuators.

The thermal stress and moment resultant vector, $\{\hat{N}_T\}$, is

$$
\{\hat{N}_T\} = \begin{bmatrix} N_{Tx} & N_{Ty} & Q_{Ty} & Q_{Tx} & N_{Txy} & M_{Tx} & M_{Ty} & M_{Txy} \end{bmatrix}^T \tag{3.83}
$$

For a laminate consisting of N layers, the equations defining the thermal stress and moment resultants are

$$
N_{Tx}(x,y,t) = \sum_{k=1}^{N} \left(\bar{C}_{11}^k \alpha_x^k + \bar{C}_{12}^k \alpha_y^k + \bar{C}_{16}^k \alpha_{xy}^k\right) \int_{z_{k-1}}^{z_k} \Theta^k(x,y,z,t)\, dz \tag{3.84}
$$

$$
N_{Ty}(x,y,t) = \sum_{k=1}^{N} \left(\bar{C}_{12}^k \alpha_x^k + \bar{C}_{22}^k \alpha_y^k + \bar{C}_{26}^k \alpha_{xy}^k\right) \int_{z_{k-1}}^{z_k} \Theta^k(x,y,z,t)\, dz \tag{3.85}
$$

$$
Q_{Ty}(x,y,t) = 0 \tag{3.86}
$$

$$
Q_{Tx}(x,y,t) = 0 \tag{3.87}
$$

$$
N_{Txy}(x,y,t) = \sum_{k=1}^{N} \left(\bar{C}_{16}^k \alpha_x^k + \bar{C}_{26}^k \alpha_y^k + \bar{C}_{66}^k \alpha_{xy}^k\right) \int_{z_{k-1}}^{z_k} \Theta^k(x,y,z,t)\, dz \tag{3.88}
$$

$$
M_{Tx}(x,y,t) = \sum_{k=1}^{N} \left(\bar{C}_{11}^k \alpha_x^k + \bar{C}_{12}^k \alpha_y^k + \bar{C}_{16}^k \alpha_{xy}^k\right) \int_{z_{k-1}}^{z_k} \Theta^k(x,y,z,t)\, z\,dz \tag{3.89}
$$

$$M_{Ty}(x,y,t) = \sum_{k=1}^{N} \left(\bar{C}_{12}^k \alpha_x^k + \bar{C}_{22}^k \alpha_y^k + \bar{C}_{26}^k \alpha_{xy}^k\right) \int_{z_{k-1}}^{z_k} \Theta^k(x,y,z,t)\, z dz \tag{3.90}$$

$$M_{Txy}(x,y,t) = \sum_{k=1}^{N} \left(\bar{C}_{16}^k \alpha_x^k + \bar{C}_{26}^k \alpha_y^k + \bar{C}_{66}^k \alpha_{xy}^k\right) \int_{z_{k-1}}^{z_k} \Theta^k(x,y,z,t)\, z dz \tag{3.91}$$

where the $\bar{C}_{ij}^k$ are the transformed elastic stiffnesses given by Equation (3.14) for the k^{th} layer of the laminate, the α_i^k are the thermal expansion coefficients for the k^{th} layer of the laminate, and $\Theta^k(x,y,z)$ is the temperature change from the stress free temperature in the k^{th} layer of the laminate.

Hamilton's variational principle can be used to derive the laminate equations of motion. In the absence of damping, this can be expressed as

$$\int_{t_1}^{t_2} (\delta K - \delta U - \delta W)\, dt = 0 \tag{3.92}$$

where K is the kinetic energy, U is the strain energy, and W is the work performed by the surface tractions. The kinetic energy term can be expressed as

$$\delta K = \delta\left(\frac{1}{2} \int_V \rho \{\dot{u}\}^T \{\dot{u}\}\, dV\right) \tag{3.93}$$

where $\{\dot{u}\} = \partial \{u\} / \partial t$ is the velocity vector of any point in the laminate, ρ is the mass density of the material, and V represents the volume occupied by the laminate. Moving the variational operator under the integral yields

$$\delta K = \frac{1}{2} \int_V \rho \left[\delta \{\dot{u}\}^T \{\dot{u}\} + \{\dot{u}\}^T \delta \{\dot{u}\}\right] dV \tag{3.94}$$

Since δK is a scalar, the terms contained in the brackets are also scalars. Therefore,

$$\{\dot{u}\}^T \delta \{\dot{u}\} = \left(\{\dot{u}\}^T \delta \{\dot{u}\}\right)^T \tag{3.95}$$

which yields

$$\{\dot{u}\}^T \delta \{\dot{u}\} = \delta \{\dot{u}\}^T \{\dot{u}\} \tag{3.96}$$

and Equation (3.94) becomes

$$\delta K = \int_V \rho \delta \{\dot{u}\}^T \{\dot{u}\}\, dV \tag{3.97}$$

Substituting Equation (3.55) into Equation (3.97) yields

$$\delta K = \int_V \rho \{\delta \dot{u}\}^T \mathcal{G}^T \mathcal{G} \{\dot{u}\} dV \tag{3.98}$$

Integrating through the thickness yields the following expression for the kinetic energy

$$\delta K = \int_A \{\delta \dot{\bar{u}}\}^T \left[\bar{M}\right] \{\dot{\bar{u}}\} dA \tag{3.99}$$

where

$$\left[\bar{M}\right] = \int_{-\frac{h}{2}}^{\frac{h}{2}} \rho \mathcal{G}^T \mathcal{G} dz = \begin{bmatrix} I_1 & 0 & 0 & I_2 & 0 \\ 0 & I_1 & 0 & 0 & I_2 \\ 0 & 0 & I_1 & 0 & 0 \\ I_2 & 0 & 0 & I_3 & 0 \\ 0 & I_2 & 0 & 0 & I_3 \end{bmatrix} \tag{3.100}$$

and

$$(I_1, I_2, I_3) = \sum_{k=1}^{N} \int_{z_{k-}}^{z_k} \rho^k \left(1, z, z^2\right) dz \tag{3.101}$$

The strain energy term is given by

$$\delta U = \int_V \{\delta \varepsilon\}^T \{\sigma\} dV \tag{3.102}$$

Defining the generalized stress vector

$$\{\bar{\sigma}\} = \lfloor \sigma_x \quad \sigma_y \quad \tau_{yz} \quad \tau_{xz} \quad \tau_{xy} \quad z\sigma_x \quad z\sigma_y \quad z\tau_{xy} \rfloor^T \tag{3.103}$$

It is possible to rewrite Equation (3.102) as

$$\begin{aligned} \delta U &= \int_A \{\delta \varepsilon\}^T \{\sigma\} dA & (3.104) \\ &= \int_A \{\delta \bar{\varepsilon}\}^T \{\bar{\sigma}\} dA & (3.105) \end{aligned}$$

Integrating through the thickness and substituting Equation (3.64) yields

$$\delta U = \int_A \{\delta \bar{\varepsilon}\}^T \left([\mathcal{D}] \{\bar{\varepsilon}\} - [P] \{V\} - \{\bar{N}_T\}\right) dA \tag{3.106}$$

The potential energy due to the transverse loading is given by

$$\delta W = \int_A p \, \delta w \, dA \tag{3.107}$$

Substituting Equations (3.97), (3.106), and (3.107) into Equation (3.92) yields

$$\int_{t_1}^{t_2}\int_A \left[\{\delta\dot{\bar{u}}\}^T [\bar{M}] \{\dot{\bar{u}}\} - \{\delta\bar{\varepsilon}\}^T \left([\mathcal{D}]\{\bar{\varepsilon}\} - [P]\{V\} - \{\bar{N}_T\}\right) + p\delta w\right] dAdt = 0 \tag{3.108}$$

Integrating the first term by parts yields the following form of Hamilton's variational principle

$$\int_{t_1}^{t_2}\int_A \left[\{-\delta\bar{u}\}^T [\bar{M}] \{\ddot{\bar{u}}\} - \{\delta\bar{\varepsilon}\}^T \left([\mathcal{D}]\{\bar{\varepsilon}\} - [P]\{V\} - \{\bar{N}_T\}\right) + p\delta w\right] dAdt = 0 \tag{3.109}$$

Rearranging yields

$$\int_{t_1}^{t_2}\int_A \left[\{\delta\bar{u}\}^T [\bar{M}] \{\ddot{\bar{u}}\} + \{\delta\bar{\varepsilon}\}^T \left([\mathcal{D}]\{\bar{\varepsilon}\} - [P]\{V\} - \{\bar{N}_T\}\right) - p\delta w\right] dAdt = 0 \tag{3.110}$$

This equation will be used to develop the finite element equations for the plate displacement portion of the problem; it will be supplemented with a finite element formulation of the heat conduction equation.

The generalized heat conduction equation for a generally anisotropic material, including the inverse pyroelectric effect, in rectangular coordinates, is

$$-\frac{\partial q_x}{\partial x} - \frac{\partial q_y}{\partial y} - \frac{\partial q_z}{\partial z} = \rho C_v \frac{\partial \Theta}{\partial t} - T_0 \frac{\partial}{\partial t}\left(\beta_{ij}\varepsilon_{ij} + p_i E_i\right) \tag{3.111}$$

where

$$q_x = -\left(k_x \frac{\partial \Theta}{\partial x} + k_{xy}\frac{\partial \Theta}{\partial y} + k_{xz}\frac{\partial \Theta}{\partial z}\right) \tag{3.112}$$

$$q_y = -\left(k_{xy} \frac{\partial \Theta}{\partial x} + k_{y}\frac{\partial \Theta}{\partial y} + k_{yz}\frac{\partial \Theta}{\partial z}\right) \tag{3.113}$$

$$q_z = -\left(k_{xz} \frac{\partial \Theta}{\partial x} + k_{yz}\frac{\partial \Theta}{\partial y} + k_{z}\frac{\partial \Theta}{\partial z}\right) \tag{3.114}$$

$$\Theta = T - T_0 \tag{3.115}$$

$$\beta_{ij}\varepsilon_{ij} = \beta_x\varepsilon_x + 2\beta_{xy}\varepsilon_{xy} + 2\beta_{xz}\varepsilon_{xz} + \beta_y\varepsilon_y + 2\beta_{yz}\varepsilon_{yz} + \beta_z\varepsilon_z \tag{3.116}$$

and p_i and E_i are the pyroelectric constant and electric field in the i^{th} direction, respectively. For the problem of a rectangular laminated composite plate composed of orthotropic layers in which the thermal properties and electric field vary only in the z direction, this equation becomes

$$\begin{aligned} &k_x \frac{\partial^2 \Theta}{\partial x^2} + 2k_{xy}\frac{\partial^2 \Theta}{\partial x \partial y} + k_y \frac{\partial^2 \Theta}{\partial y^2} + \frac{\partial}{\partial z}\left(k_z \frac{\partial \Theta}{\partial z}\right) \\ &-\rho C_v \frac{\partial \Theta}{\partial t} - T_0 \frac{\partial}{\partial t}\left(\beta_x\varepsilon_x + 2\beta_{xy}\varepsilon_{xy} + \beta_y\varepsilon_y + p_z E_z\right) = 0 \end{aligned} \tag{3.117}$$

Expressing the strains in terms of the displacements yields

$$
\begin{aligned}
& k_x \frac{\partial^2 \Theta}{\partial x^2} + 2k_{xy}\frac{\partial^2 \Theta}{\partial x \partial y} + k_y \frac{\partial^2 \Theta}{\partial y^2} + \frac{\partial}{\partial z}\left(k_z \frac{\partial \Theta}{\partial z}\right) - \rho C_v \frac{\partial \Theta}{\partial t} - T_0 \frac{\partial}{\partial t}\left[\beta_x \left(\frac{\partial u^0}{\partial x} + z\frac{\partial \psi_x}{\partial x}\right)\right. \\
& \left. +2\beta_{xy}\left(\frac{\partial u^0}{\partial y} + z\frac{\partial \psi_x}{\partial y} + \frac{\partial v^0}{\partial x} + z\frac{\partial \psi_y}{\partial x}\right) + \beta_y\left(\frac{\partial v^0}{\partial y} + z\frac{\partial \psi_y}{\partial y}\right)\right] - T_0 p_z \dot{E}_z = 0 \qquad (3.118)
\end{aligned}
$$

Only piezoelectric layers have non-zero p_z, and in this work only those piezoelectric elements used as actuators are considered to have significant $\dot{E}_z$. For the k^{th} piezoelectric actuator, ignoring the change in the electric field generated by the strain rate and assuming the electric potential is linear across the piezoelectric element and increasing with increasing z,

$$
\begin{aligned}
E_z &= -\frac{\partial \phi}{\partial z} && (3.119)\\
&= -\frac{V_z}{h} && (3.120)
\end{aligned}
$$

and

$$
\dot{E}_z = -\frac{\dot{V}_z}{h}
$$

where V_z represents the external voltage applied to the piezoelectric actuator. Subsequent equations will also drop the z subscript unless needed for clarity. Equation (3.118) can be reformulated so that the voltage rate across the piezoelectric elements are inputs to the system.

$$
\begin{aligned}
& k_x \frac{\partial^2 \Theta}{\partial x^2} + 2k_{xy}\frac{\partial^2 \Theta}{\partial x \partial y} + k_y \frac{\partial^2 \Theta}{\partial y^2} + \frac{\partial}{\partial z}\left(k_z \frac{\partial \Theta}{\partial z}\right) - \rho C_v \frac{\partial \Theta}{\partial t} - T_0 \frac{\partial}{\partial t}\left[\beta_x \left(\frac{\partial u^0}{\partial x} + z\frac{\partial \psi_x}{\partial x}\right)\right. \\
& \left. +2\beta_{xy}\left(\frac{\partial u^0}{\partial y} + z\frac{\partial \psi_x}{\partial y} + \frac{\partial v^0}{\partial x} + z\frac{\partial \psi_y}{\partial x}\right) + \beta_y\left(\frac{\partial v^0}{\partial y} + z\frac{\partial \psi_y}{\partial y}\right)\right] - T_0 \lfloor p \rfloor \left\{\dot{V}\right\} = 0 \qquad (3.121)
\end{aligned}
$$

$$
\lfloor p \rfloor = \begin{bmatrix} \frac{p_1}{h_1} & \frac{p_2}{h_2} & \cdots & \frac{p_{N_A}}{h_{N_A}} \end{bmatrix} \qquad (3.122)
$$

$$
\left\{\dot{V}\right\} = \begin{bmatrix} \dot{V}_1 & \dot{V}_2 & \cdots & \dot{V}_{N_A} \end{bmatrix}^T \qquad (3.123)
$$

where the p_k and h_k are the k^{th} piezoelectric actuator pyroelectric constant and thickness, respectively, and N_A is the number of actuators.

3.2.4 Finite Element Model

The first-order shear deformation theory allows the use of linear interpolation functions to develop the finite element model. This follows from the derivative operator $\mathcal{L}$, defined in Eq (3.63).

which contains first-order derivatives and constants. Thus, it is sufficient for the interpolation functions to be C^0 continuous [24]. Formulating the problem with classical laminated plate theory ($CLPT$) results in second-order derivatives in the differential operator $\mathcal{L}$. This requires cubic interpolation functions on the variables which is computationally more difficult. In the first-order shear deformation theory finite element model, this difficulty is overcome by adding two more variables for interpolation, ψ_x and ψ_y. In the present work, nine-node quadrilateral finite elements with five degrees of freedom at each node are used. To reduce the number of finite elements required for convergence of the solution, quadratic interpolation is used for all variables over each element. Therefore, the interpolation equations can be written as

$$\begin{aligned} \{\bar{u}^e(x,y,t)\} &= \sum_{i=1}^{N_n} [N_i^e] \{\bar{u}_i^e(t)\} \\ [N_i^e] &= N_i^e I_5 \end{aligned} \tag{3.124}$$

where

$$N_1^e = f_l(x,x_l,x_u)\, f_l(y,y_l,y_u) \tag{3.125}$$

$$N_2^e = f_u(x,x_l,x_u)\, f_l(y,y_l,y_u) \tag{3.126}$$

$$N_3^e = f_u(x,x_l,x_u)\, f_u(y,y_l,y_u) \tag{3.127}$$

$$N_4^e = f_l(x,x_l,x_u)\, f_u(y,y_l,y_u) \tag{3.128}$$

$$N_5^e = f_m(x,x_l,x_u)\, f_l(y,y_l,y_u) \tag{3.129}$$

$$N_6^e = f_u(x,x_l,x_u)\, f_m(y,y_l,y_u) \tag{3.130}$$

$$N_7^e = f_m(x,x_l,x_u)\, f_u(y,y_l,y_u) \tag{3.131}$$

$$N_8^e = f_l(x,x_l,x_u)\, f_m(y,y_l,y_u) \tag{3.132}$$

$$N_9^e = f_m(x,x_l,x_u)\, f_m(y,y_l,y_u) \tag{3.133}$$

and

$$f_l(x,x_l,x_u) = \frac{2x^2 - (3x_u - x_l)\,x + (x_u + x_l)\,x_u}{(x_u - x_l)^2} \tag{3.134}$$

$$f_m(x,x_l,x_u) = -4\frac{x^2 - (x_u - x_l)\,x - x_u x_l}{(x_u - x_l)^2} \tag{3.135}$$

$$f_u\left(x,x_l,x_u\right) = \frac{2x^2 - \left(x_u + 3x_l\right)x + \left(x_u + x_l\right)x_l}{\left(x_u - x_l\right)^2} \tag{3.136}$$

Here N_n is the number of nodes per element, N_i^e are the element shape functions, x_l and x_u, y_l and y_u are the lower and upper bounds on the x and y dimensions of the current finite element, I_5 is the 5×5 identity matrix, and the superscript e denotes the parameter at the element level. The local numbering of the nodes and nodal coordinates is shown in Figure 3.1. The interpolation Equations

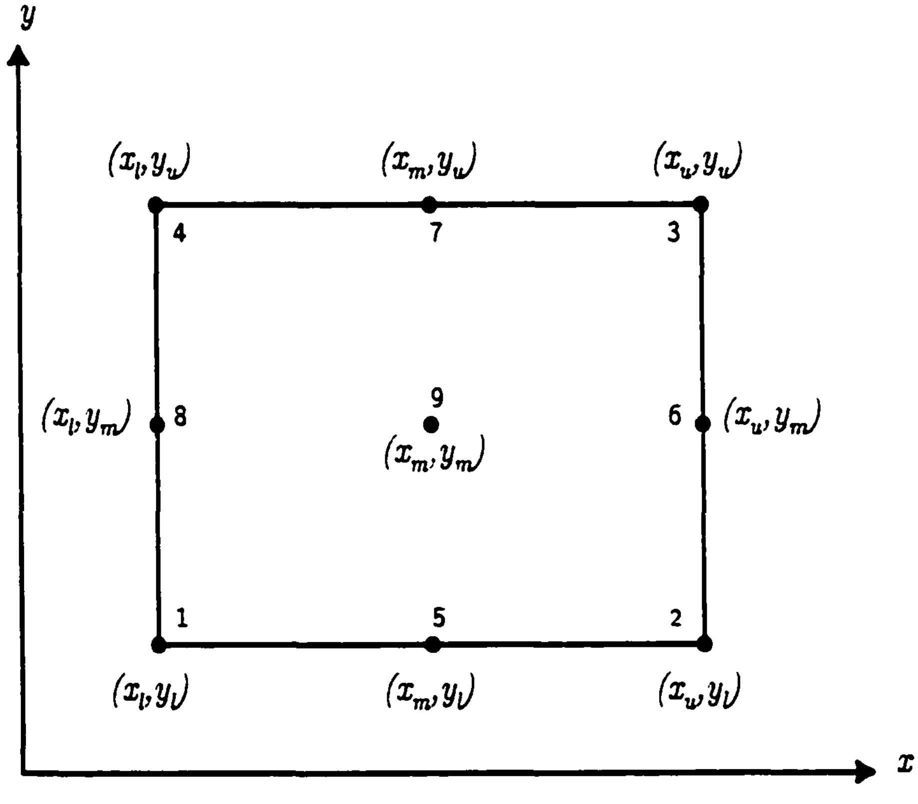

Figure 3.1: Nine-node quadrilateral mechanical finite element showing local node numbering and nodal coordinates.

(3.134) through (3.136) were derived assuming

$$x_m = \frac{1}{2}\left(x_u - x_l\right) \tag{3.137}$$

The interpolated variables are the displacements and rotations at each node

$$\left\{\bar{u}_i^e\right\} = \begin{bmatrix} u_i^0 & v_i^0 & w_i^0 & \psi_{xi} & \psi_{yi} \end{bmatrix}^T \tag{3.138}$$

Here u_i^0, v_i^0, w_i^0, v_{xi}, v_{yi} are the i^{th} nodal values of u^0, v^0, w^0, v_x, v_y, respectively. Equation (3.124) can be written in compact notation as

$$\{\bar{u}^e\} = [N^e]\{\tilde{u}^e\} \tag{3.139}$$

where

$$[N^e] = [[N_1^e], [N_2^e], \ldots, [N_{N_n}^e]] \tag{3.140}$$

$$\{\tilde{u}^e\} = \left(\{\tilde{u}_1^e\}^T, \{\tilde{u}_2^e\}^T, \ldots, \{\tilde{u}_{N_n}^e\}^T\right)^T \tag{3.141}$$

Substituting Equation (3.139) into Equation (3.62) yields

$$\{\bar{\varepsilon}^e\} = [B^e]\{\tilde{u}^e\} \tag{3.142}$$

$$[B^e] = \mathcal{L}[N^e] \tag{3.143}$$

To derive a finite element model, we divide the plate area, A, of Equation (3.110) into a finite number of element areas, A_e. Applying this process to Equation (3.110) yields

$$\int_{t_1}^{t_2} \sum_{e=1}^{N_{me}} \int_{A_e} \left[\{\delta\bar{u}^e\}^T [\bar{M}]\{\ddot{\bar{u}}^e\} - \{\delta\bar{\varepsilon}^e\}^T ([D]\{\bar{\varepsilon}^e\}\right.$$
$$\left. - [P^e]\{V^e\} - \{\bar{N}_T^e\}) - \{\delta\bar{u}^e\}^T\{\bar{F}^e\}\right] dA dt = 0 \tag{3.144}$$

where N_{me} is the total number of mechanical finite elements, the superscript e denotes that the parameter is associated with the current mechanical finite element, and

$$\{\bar{F}^e\} = (0, 0, p^e, 0, 0)^T \tag{3.145}$$

is the element mechanical load vector. Substituting Equations (3.139) and (3.142) into Equation (3.144) yields

$$\int_{t_1}^{t_2} \left[\sum_{e=1}^{N_{me}} \{\delta\tilde{u}^e\}^T ([M_M^e]\{\ddot{\tilde{u}}^e\} + [K_M^e]\{\tilde{u}^e\} - [F_{MP}^e]\{V^e\} - \{F_{MT}^e\} - \{F_M^e\})\right] dt = 0 \tag{3.146}$$

where

$$\begin{aligned} [M_M^e] &= \int_{A_e} [N^e]^T [\bar{M}] [N^e] dA \\ &= \int_{y_l}^{y_u} \int_{x_l}^{x_u} [N^e]^T [\bar{M}] [N^e] dx dy \end{aligned} \tag{3.147}$$

$$
\begin{aligned}
[K_M^e] &= \int_{A_e} [B^e]^T [\mathcal{D}] [B^e] \, dA \\
&= \int_{y_l}^{y_u} \int_{x_l}^{x_u} [B^e]^T [\mathcal{D}] [B^e] \, dx dy
\end{aligned} \tag{3.148}
$$

$$
\begin{aligned}
[F_{MP}^e] &= \int_{A_e} [B^e]^T [P^e] \, dA \\
&= \left(\int_{y_l}^{y_u} \int_{x_l}^{x_u} [B^e]^T \, dx dy \right) [P^e]
\end{aligned} \tag{3.149}
$$

$$
\begin{aligned}
\{F_{MT}^e\} &= \int_{A_e} [B^e]^T \{\bar{N}_T^e\} \, dA \\
&= \int_{y_l}^{y_u} \int_{x_l}^{x_u} [B^e]^T \{\bar{N}_T^e\} \, dx dy
\end{aligned} \tag{3.150}
$$

$$
\begin{aligned}
\{F_M^e\} &= \int_{A_e} [N^e]^T \{\bar{F}^e\} \, dA \\
&= \int_{y_l}^{y_u} \int_{x_l}^{x_u} [N^e]^T \{\bar{F}^e\} \, dx dy
\end{aligned} \tag{3.151}
$$

In these equations, x_l and x_u (y_l and y_u) are the lower and upper values of the x (y) dimension for the current mechanical finite element, respectively, and $\{\bar{N}_T^e\}$ represents the thermal stress and moment resultant associated with the current mechanical finite element. Special care is needed to insure that $[K_M^e]$ and $\{F_{MT}^e\}$ are properly calculated. To avoid shear locking, the shear portion $[K_M^e]$ should be under-integrated [36]. To facilitate this method, the element stiffness equation is separated into a bending stiffness portion and a shear stiffness portion

$$
\begin{aligned}
[K_M^e] &= \int_{A_e} \left([B_b^e]^T [\mathcal{D}_b] [B_b^e] + [B_s^e]^T [\mathcal{D}_s] [B_s^e] \right) dA \\
&= \int_{y_l}^{y_u} \int_{x_l}^{x_u} \left([B_b^e]^T [\mathcal{D}_b] [B_b^e] + [B_s^e]^T [\mathcal{D}_s] [B_s^e] \right) dx dy
\end{aligned} \tag{3.152}
$$

where

$$[\mathcal{D}_b] = \begin{bmatrix} A_{11} & A_{12} & 0 & 0 & A_{16} & B_{11} & B_{12} & B_{16} \\ A_{12} & A_{22} & 0 & 0 & A_{26} & B_{12} & B_{22} & B_{26} \\ 0 & 0 & 0 & 0 & 0 & 0 & 0 & 0 \\ 0 & 0 & 0 & 0 & 0 & 0 & 0 & 0 \\ A_{16} & A_{26} & 0 & 0 & A_{66} & B_{16} & B_{26} & B_{66} \\ B_{11} & B_{12} & 0 & 0 & B_{16} & D_{11} & D_{12} & D_{16} \\ B_{12} & B_{22} & 0 & 0 & B_{26} & D_{12} & D_{22} & D_{26} \\ B_{16} & B_{26} & 0 & 0 & B_{66} & D_{16} & D_{26} & D_{66} \end{bmatrix} \tag{3.153}$$

$$[\mathcal{D}_s] = \begin{bmatrix} 0 & 0 & 0 & 0 & 0 & 0 & 0 & 0 \\ 0 & 0 & 0 & 0 & 0 & 0 & 0 & 0 \\ 0 & 0 & A_{44} & A_{45} & 0 & 0 & 0 & 0 \\ 0 & 0 & A_{45} & A_{55} & 0 & 0 & 0 & 0 \\ 0 & 0 & 0 & 0 & 0 & 0 & 0 & 0 \\ 0 & 0 & 0 & 0 & 0 & 0 & 0 & 0 \\ 0 & 0 & 0 & 0 & 0 & 0 & 0 & 0 \\ 0 & 0 & 0 & 0 & 0 & 0 & 0 & 0 \end{bmatrix} \tag{3.154}$$

$$[B_b^e] = \begin{bmatrix} \frac{\partial}{\partial x} & 0 & 0 & 0 & 0 \\ 0 & \frac{\partial}{\partial y} & 0 & 0 & 0 \\ 0 & 0 & 0 & 0 & 0 \\ 0 & 0 & 0 & 0 & 0 \\ \frac{\partial}{\partial y} & \frac{\partial}{\partial x} & 0 & 0 & 0 \\ 0 & 0 & 0 & \frac{\partial}{\partial x} & 0 \\ 0 & 0 & 0 & 0 & \frac{\partial}{\partial y} \\ 0 & 0 & 0 & \frac{\partial}{\partial y} & \frac{\partial}{\partial x} \end{bmatrix} [N^e] \tag{3.155}$$

$$
[B_{s_1}^e] = \begin{bmatrix} 0 & 0 & 0 & 0 & 0 \\ 0 & 0 & 0 & 0 & 0 \\ 0 & 0 & \frac{\partial}{\partial y} & 0 & 1 \\ 0 & 0 & \frac{\partial}{\partial x} & 1 & 0 \\ 0 & 0 & 0 & 0 & 0 \\ 0 & 0 & 0 & 0 & 0 \\ 0 & 0 & 0 & 0 & 0 \\ 0 & 0 & 0 & 0 & 0 \end{bmatrix} [N^e] \tag{3.156}
$$

In this case, exact integration is used to integrate the bending stiffness terms (terms with the subscript b) and numerical integration is used for integration of the shear stiffness terms (terms with the subscript s). For quadratic shape functions, exact numerical integration of the shear stiffness terms requires a three-point Gauss quadrature. Therefore, to under-integrate the shear stiffness terms by one, a two-point Gauss quadrature is used. Gauss quadrature formulas for general limits of integration can be found in [47]. Applying the two-point Gauss quadrature formula to the shear stiffness term yields

$$
\begin{aligned}
[K_{M_{s1}}^e] &= \int_{y_l}^{y_u} \int_{x_l}^{x_u} [B_{s}^e]^T [\mathcal{D}_{s}] [B_{s1}^e] \, dx dy \\
&= \int_{y_l}^{y_u} \int_{x_l}^{x_u} f(x, y) \, dx dy \\
&\approx \frac{1}{4} (y_u - y_l)(x_u - x_l) [f(x_1, y_1) - f(x_2, y_1) - f(x_1, y_2) - f(x_2, y_2)]
\end{aligned} \tag{3.157}
$$

where

$$
x_1 = \frac{1}{2}\left[\left(1 - \frac{1}{\sqrt{3}}\right) x_l - \left(1 - \frac{1}{\sqrt{3}}\right) x_u\right] \tag{3.158}
$$

$$
x_2 = \frac{1}{2}\left[\left(1 - \frac{1}{\sqrt{3}}\right) x_l - \left(1 - \frac{1}{\sqrt{3}}\right) x_u\right] \tag{3.159}
$$

$$
y_2 = \frac{1}{2}\left[\left(1 - \frac{1}{\sqrt{3}}\right) y_l - \left(1 - \frac{1}{\sqrt{3}}\right) y_u\right] \tag{3.160}
$$

$$
y_2 = \frac{1}{2}\left[\left(1 - \frac{1}{\sqrt{3}}\right) y_l - \left(1 - \frac{1}{\sqrt{3}}\right) y_u\right] \tag{3.161}
$$

Further expansion of the expression for $\{F_{MT}^e\}$ is deferred until the development of the finite element equations relating to the thermal portion of the problem. For a general mechanical load, Equation

(3.151) can be reformulated so that $\left\{\bar{F}^e\right\}$ is interpolated using the same quadratic interpolation functions as for the displacements and rotations.

$$\left\{\bar{F}^e(x,y,t)\right\} = \sum_{i=1}^{N_n} [N_i^e] \left\{\bar{F}_i^e(t)\right\} \tag{3.162}$$

where

$$\left\{\bar{F}_i^e(t)\right\} = (0, 0, p_i^e, 0, 0)^T \tag{3.163}$$

and p_i^e is the pressure at the i^{th} node. Substituting Equation (3.162) into Equation (3.151) yields

$$\{F_M^e\} = \left(\int_{y_l}^{y_u} \int_{x_l}^{x_u} [N^e]^T [N^e] \, dx dy\right) \left\{\bar{F}^e\right\} \tag{3.164}$$

For the case of a uniform pressure load, p, Equation (3.151) can be simplified to

$$\begin{aligned} \{F_M^e\} &= \left(\int_{y_l}^{y_u} \int_{x_l}^{x_u} [N^e]^T \, dx dy\right) \left\{\begin{bmatrix} 0 & 0 & p & 0 & 0 \end{bmatrix}^T\right\} \\ &= p \end{aligned} \tag{3.165}$$

Summing over all mechanical finite elements, Equation (3.146) can be written as

$$\int_{t}^{t_2} \{\delta\bar{u}\}^T \left([M_M]\{\ddot{\bar{u}}\} + [K_M]\{\bar{u}\} - [F_{MP}]\{V\} - \{F_{MT}\} - \{F_M\}\right) dt = 0 \tag{3.166}$$

Since the variation $\{\delta\bar{u}\}$ is arbitrary, we get

$$[M_M]\{\ddot{\bar{u}}\} + [K_M]\{\bar{u}\} = [F_{MP}]\{V\} - \{F_{MT}\} - \{F_M\} \tag{3.167}$$

Equation (3.167) is the finite element differential equation governing the mechanical motion of the plate.

Applying the weak form of the Galerkin finite element formulation to Equation (3.121), the weighted average of the residual is

$$\begin{aligned} I = & \int_{-\frac{h}{2}}^{\frac{h}{2}} \int_0^b \int_0^a \left\{ w \left[k_x \frac{\partial^2\bar{\Theta}}{\partial x^2} + 2k_{xy}\frac{\partial^2\bar{\Theta}}{\partial x \partial y} + k_y \frac{\partial^2\bar{\Theta}}{\partial y^2} + \frac{\partial}{\partial z}\left(k_z \frac{\partial\bar{\Theta}}{\partial z}\right) - \rho C_v \frac{\partial\bar{\Theta}}{\partial t} \right.\right. \\ & -T_0 \frac{\partial}{\partial t}\left(\beta_x \left(\frac{\partial\bar{u}^0}{\partial x} + z\frac{\partial\bar{\psi}_x}{\partial x}\right) + 2\beta_{xy}\left(\frac{\partial\bar{u}^0}{\partial y} + z\frac{\partial\bar{\psi}_x}{\partial y} + \frac{\partial\bar{v}^0}{\partial x} + z\frac{\partial\bar{\psi}_y}{\partial x}\right)\right. \\ & \left.\left.\left. +\beta_y \left(\frac{\partial\bar{v}^0}{\partial y} + z\frac{\partial\bar{\psi}_y}{\partial y}\right)\right) + T_0 [p]\left\{\dot{V}\right\}\right]\right\} dx dy dz \end{aligned} \tag{3.168}$$

where $\tilde{\Theta}$, $\tilde{u}^0$, $\tilde{v}^0$, $\tilde{\psi}_x$, and $\tilde{\psi}_y$ are the trial functions, and w is the weighting function. Integration by parts is then used to reduce the order of the derivatives on $\tilde{\Theta}$ which yields

$$
\begin{aligned}
I_T = & \int_{-\frac{h}{2}}^{\frac{h}{2}} \int_0^b \int_0^a \left\{ -k_x \frac{\partial w}{\partial x}\frac{\partial \tilde{\Theta}}{\partial x} - k_{xy}\left(\frac{\partial w}{\partial x}\frac{\partial \tilde{\Theta}}{\partial y} + \frac{\partial w}{\partial y}\frac{\partial \tilde{\Theta}}{\partial x}\right) - k_y \frac{\partial w}{\partial y}\frac{\partial \tilde{\Theta}}{\partial y} - k_z \frac{\partial w}{\partial z}\frac{\partial \tilde{\Theta}}{\partial z} \right. \\
& -\rho C_v w \frac{\partial \tilde{\Theta}}{\partial t} - T_0 w \frac{\partial}{\partial t}\left[\beta_x \left(\frac{\partial \tilde{u}^0}{\partial x} + z\frac{\partial \tilde{\psi}_x}{\partial x}\right) + 2\beta_{xy}\left(\frac{\partial \tilde{u}^0}{\partial y} + z\frac{\partial \tilde{\psi}_x}{\partial y} + \frac{\partial \tilde{v}^0}{\partial x} + z\frac{\partial \tilde{\psi}_y}{\partial x}\right)\right. \\
& \left.\left. +\beta_y \left(\frac{\partial \tilde{v}^0}{\partial y} + z\frac{\partial \tilde{\psi}_y}{\partial y}\right)\right] - T_0 w \lfloor p \rfloor \left\{ \dot{V} \right\} \right\} dxdydz - \int_{-\frac{h}{2}}^{\frac{h}{2}} \int_0^b \left(k_x w \left. \frac{\partial \tilde{\Theta}}{\partial x}\right|_{x=0}^{x=a} \right) dydz \\
& - \int_{-\frac{h}{2}}^{\frac{h}{2}} \int_0^b \left(k_{xy} w \left. \frac{\partial \tilde{\Theta}}{\partial y}\right|_{x=0}^{x=a} \right) dydz - \int_{-\frac{h}{2}}^{\frac{h}{2}} \int_0^a \left(k_{xy} w \left. \frac{\partial \tilde{\Theta}}{\partial x}\right|_{y=0}^{y=b} \right) dxdz \qquad (3.169) \\
& - \int_{-\frac{h}{2}}^{\frac{h}{2}} \int_0^a \left(k_y w \left. \frac{\partial \tilde{\Theta}}{\partial y}\right|_{y=0}^{y=b} \right) dxdz - \int_0^b \int_0^a \left(k_z w \left. \frac{\partial \tilde{\Theta}}{\partial z}\right|_{z=-\frac{h}{2}}^{z=\frac{h}{2}} \right) dxdy
\end{aligned}
$$

If the domain is discretized into N_{te} cubic elements, the weighted average residual can be written as

$$
\begin{aligned}
I_T = & \sum_{k=1}^{N_{te}} \int_{z_l}^{z_u} \int_{y_l}^{y_u} \int_{x_l}^{x_u} \left\{ -k_x \frac{\partial w}{\partial x}\frac{\partial \tilde{\Theta}}{\partial x} - k_{xy}\left(\frac{\partial w}{\partial x}\frac{\partial \tilde{\Theta}}{\partial y} + \frac{\partial w}{\partial y}\frac{\partial \tilde{\Theta}}{\partial x}\right) - k_y \frac{\partial w}{\partial y}\frac{\partial \tilde{\Theta}}{\partial y} - k_z \frac{\partial w}{\partial z}\frac{\partial \tilde{\Theta}}{\partial z} \right. \\
& -\rho C_v w \frac{\partial \tilde{\Theta}}{\partial t} - T_0 w \frac{\partial}{\partial t}\left[\beta_x \left(\frac{\partial \tilde{u}^0}{\partial x} + z\frac{\partial \tilde{\psi}_x}{\partial x}\right) + 2\beta_{xy}\left(\frac{\partial \tilde{u}^0}{\partial y} + z\frac{\partial \tilde{\psi}_x}{\partial y} + \frac{\partial \tilde{v}^0}{\partial x} + z\frac{\partial \tilde{\psi}_y}{\partial x}\right)\right. \\
& \left.\left. +\beta_y \left(\frac{\partial \tilde{v}^0}{\partial y} + z\frac{\partial \tilde{\psi}_y}{\partial y}\right)\right] - T_0 w \lfloor p \rfloor \left\{ \dot{V} \right\} \right\} dxdydz \\
& - \sum_{k=1}^{N_{Tex_l}} \int_{z_l}^{z_u} \int_{y_l}^{y_u} \left(\left[k_z w \frac{\partial \tilde{\Theta}}{\partial x} + k_{xy} w \frac{\partial \tilde{\Theta}}{\partial y} \right|_{x=0} \right) dydz \\
& - \sum_{k=1}^{N_{Tex_m}} \int_{z_l}^{z_u} \int_{y_l}^{y_u} \left(\left[k_x w \frac{\partial \tilde{\Theta}}{\partial x} + k_{xy} w \frac{\partial \tilde{\Theta}}{\partial y} \right|_{x=a} \right) dydz \qquad (3.170) \\
& - \sum_{k=1}^{N_{Tey_l}} \int_{z_l}^{z_u} \int_{x_l}^{x_u} \left(\left[k_y w \frac{\partial \tilde{\Theta}}{\partial y} + k_{xy} w \frac{\partial \tilde{\Theta}}{\partial x} \right|_{y=0} \right) dxdz \\
& - \sum_{k=1}^{N_{Tey_u}} \int_{z_l}^{z_u} \int_{x_l}^{x_u} \left(\left[k_y w \frac{\partial \tilde{\Theta}}{\partial y} + k_{xy} w \frac{\partial \tilde{\Theta}}{\partial x} \right|_{y=b} \right) dxdz \\
& - \sum_{k=1}^{N_{Tez_l}} \int_{y_l}^{y_u} \int_{x_l}^{x_u} \left(k_z w \left. \frac{\partial \tilde{\Theta}}{\partial z} \right|_{z=-\frac{h}{2}} \right) dxdy - \sum_{k=1}^{N_{Tez_q}} \int_{y_l}^{y_u} \int_{x_l}^{x_u} \left(k_z w \left. \frac{\partial \tilde{\Theta}}{\partial z} \right|_{z=\frac{h}{2}} \right) dxdy
\end{aligned}
$$

where N_{Tex_l}, N_{Tex_m}, N_{Tey_n}, N_{Tey_u}, N_{Tez_l}, and N_{Tez_q} represent the number of elements that are adjacent to the boundary at $x = 0$, $x = a$, $y = 0$, $y = b$, $z = -\frac{h}{2}$, and $z = \frac{h}{2}$, respectively. The variables x_l, x_u, y_l, y_u, z_l, and z_u are the lower and upper bounds on the x, y, and z dimensions of the k^{th} cubic element, respectively. Let $\tilde{\Theta}$ be approximated using a combination of quadratic and linear shape functions such that, over the k^{th} element, the trial function is

$$\begin{aligned}
\tilde{\Theta}^k(x,y,z,t) &= \sum_{i=1}^{18} H_{Ti}^k(x,y,z)\,\Theta_i^k(t) \\
&= \begin{bmatrix} H_{T1}^k(x,y,z) & H_{T2}^k(x,y,z) & \cdots & H_{T18}^k(x,y,z) \end{bmatrix} \begin{Bmatrix} \Theta_1^k(t) \\ \Theta_2^k(t) \\ \vdots \\ \Theta_{18}^k(t) \end{Bmatrix} \\
&= \left[H_T^k(x,y,z)\right]\left\{\Theta^k(t)\right\}
\end{aligned} \tag{3.171}$$

where

$$H_{T1}^k(x,y,z) = f_l(x,x_l,x_u)\,f_l(y,y_l,y_u)\,\frac{(z_u - z)}{(z_u - z_l)} \tag{3.172}$$

$$H_{T2}^k(x,y,z) = f_u(x,x_l,x_u)\,f_l(y,y_l,y_u)\,\frac{(z_u - z)}{(z_u - z_l)} \tag{3.173}$$

$$H_{T3}^k(x,y,z) = f_u(x,x_l,x_u)\,f_u(y,y_l,y_u)\,\frac{(z_u - z)}{(z_u - z_l)} \tag{3.174}$$

$$H_{T4}^k(x,y,z) = f_l(x,x_l,x_u)\,f_u(y,y_l,y_u)\,\frac{(z_u - z)}{(z_u - z_l)} \tag{3.175}$$

$$H_{T5}^k(x,y,z) = f_m(x,x_l,x_u)\,f_l(y,y_l,y_u)\,\frac{(z_u - z)}{(z_u - z_l)} \tag{3.176}$$

$$H_{T6}^k(x,y,z) = f_u(x,x_l,x_u)\,f_m(y,y_l,y_u)\,\frac{(z_u - z)}{(z_u - z_l)} \tag{3.177}$$

$$H_{T7}^k(x,y,z) = f_m(x,x_l,x_u)\,f_u(y,y_l,y_u)\,\frac{(z_u - z)}{(z_u - z_l)} \tag{3.178}$$

$$H_{T8}^k(x,y,z) = f_l(x,x_l,x_u)\,f_m(y,y_l,y_u)\,\frac{(z_u - z)}{(z_u - z_l)} \tag{3.179}$$

$$H_{T9}^k(x,y,z) = f_m(x,x_l,x_u)\,f_m(y,y_l,y_u)\,\frac{(z_u - z)}{(z_u - z_l)} \tag{3.180}$$

$$H_{T10}^k(x,y,z) = f_l(x,x_l,x_u)\,f_l(y,y_l,y_u)\,\frac{(z - z_l)}{(z_u - z_l)} \tag{3.181}$$

$$H_{T11}^k(x,y,z) = f_u(x,x_l,x_u)\,f_l(y,y_l,y_u)\,\frac{(z - z_l)}{(z_u - z_l)} \tag{3.182}$$

$$H_{T12}^k(x,y,z) = f_u(x,x_l,x_u)\,f_u(y,y_l,y_u)\,\frac{(z - z_l)}{(z_u - z_l)} \tag{3.183}$$

$$H_{T13}^k(x,y,z) = f_l(x,x_l,x_u)\,f_u(y,y_l,y_u)\,\frac{(z - z_l)}{(z_u - z_l)} \tag{3.184}$$

$$H_{T14}^k(x,y,z) = f_m(x,x_l,x_u)\,f_l(y,y_l,y_u)\,\frac{(z - z_l)}{(z_u - z_l)} \tag{3.185}$$

$$H_{T15}^{k}(x,y,z) = f_u(x,x_l,x_u)\, f_m(y,y_l,y_u)\,\frac{(z-z_l)}{(z_u-z_l)} \tag{3.186}$$

$$H_{T16}^{k}(x,y,z) = f_m(x,x_l,x_u)\, f_u(y,y_l,y_u)\,\frac{(z-z_l)}{(z_u-z_l)} \tag{3.187}$$

$$H_{T17}^{k}(x,y,z) = f_l(x,x_l,x_u)\, f_m(y,y_l,y_u)\,\frac{(z-z_l)}{(z_u-z_l)} \tag{3.188}$$

$$H_{T18}^{k}(x,y,z) = f_m(x,x_l,x_u)\, f_m(y,y_l,y_u)\,\frac{(z-z_l)}{(z_u-z_l)} \tag{3.189}$$

and f_l, f_m, and f_u are defined by Equations (3.134) through (3.136), respectively. The geometry and local node numbering of the cubic element is shown in Figure 3.2. In the Galerkin's method, the test functions are

$$\mathbf{w} = \begin{bmatrix} H_{T1}^{k}(x,y,z) \\ H_{T2}^{k}(x,y,z) \\ \vdots \\ H_{T18}^{k}(x,y,z) \end{bmatrix} = \left[H_T^k(x,y,z)\right]^T \tag{3.190}$$

Substituting Equations (3.171) and (3.190) into Equation (3.170) and performing the integration over the k^{th} non-boundary element yields

$$\begin{aligned} I_T^k \;=\; & -\left[M_T^k\right]\left\{\dot{\Theta}^k(t)\right\} - \left[K_T^k\right]\left\{\Theta^k(t)\right\} - \left\{F_{QP}^k\right\}\dot{V}^k \\ & -T_0\int_{z_l}^{z_u}\int_{y_l}^{y_u}\int_{x_l}^{x_u}\left[H_T^k\right]^T\frac{\partial}{\partial t}\left[\beta_x\left(\frac{\partial \tilde{u}^0}{\partial x} - z\frac{\partial \tilde{\psi}_x}{\partial x}\right)\right. \\ & \left. -2\beta_{xy}\left(\frac{\partial \tilde{u}^0}{\partial y} - z\frac{\partial \tilde{\psi}_x}{\partial y} - \frac{\partial \tilde{v}^0}{\partial x} - z\frac{\partial \tilde{\psi}_y}{\partial x}\right) - \beta_y\left(\frac{\partial \tilde{v}^0}{\partial y} - z\frac{\partial \tilde{\psi}_y}{\partial y}\right)\right] dxdydz \end{aligned} \tag{3.191}$$

Here

$$\left[M_T^k\right] = \int_{z_l}^{z_u}\rho C_v\int_{y_l}^{y_u}\int_{x_l}^{x_u}\left(\left[H_T^k\right]^T\left[H_T^k\right]\right) dxdydz \tag{3.192}$$

$$\begin{aligned} \left[K_T^k\right] \;=\; & \int_{z_l}^{z_u}\int_{y_l}^{y_u}\int_{x_l}^{x_u}\left\{k_x\frac{\partial\left[H_T^k\right]^T}{\partial x}\frac{\partial\left[H_T^k\right]}{\partial x} + k_{xy}\left(\frac{\partial\left[H_T^k\right]^T}{\partial x}\frac{\partial\left[H_T^k\right]}{\partial y}\right.\right. \\ & \left.\left. + \frac{\partial\left[H_T^k\right]^T}{\partial y}\frac{\partial\left[H_T^k\right]}{\partial x}\right) + k_y\frac{\partial\left[H_T^k\right]^T}{\partial y}\frac{\partial\left[H_T^k\right]}{\partial y} + k_z\frac{\partial\left[H_T^k\right]^T}{\partial z}\frac{\partial\left[H_T^k\right]}{\partial z}\right\} dxdydz \end{aligned} \tag{3.193}$$

$$\left\{F_{QP}^k\right\} = T_0\frac{p_k}{h_k}\int_{z_l}^{z_u}\int_{y_l}^{y_u}\int_{x_l}^{x_u}\left[H_T^k\right]^T dxdydz \tag{3.194}$$

and the explicit dependence of H_T^k on x, y, and z has been dropped for clarity. The remaining integral in Equation (3.191) contains the terms that couple the mechanical motion into the thermal

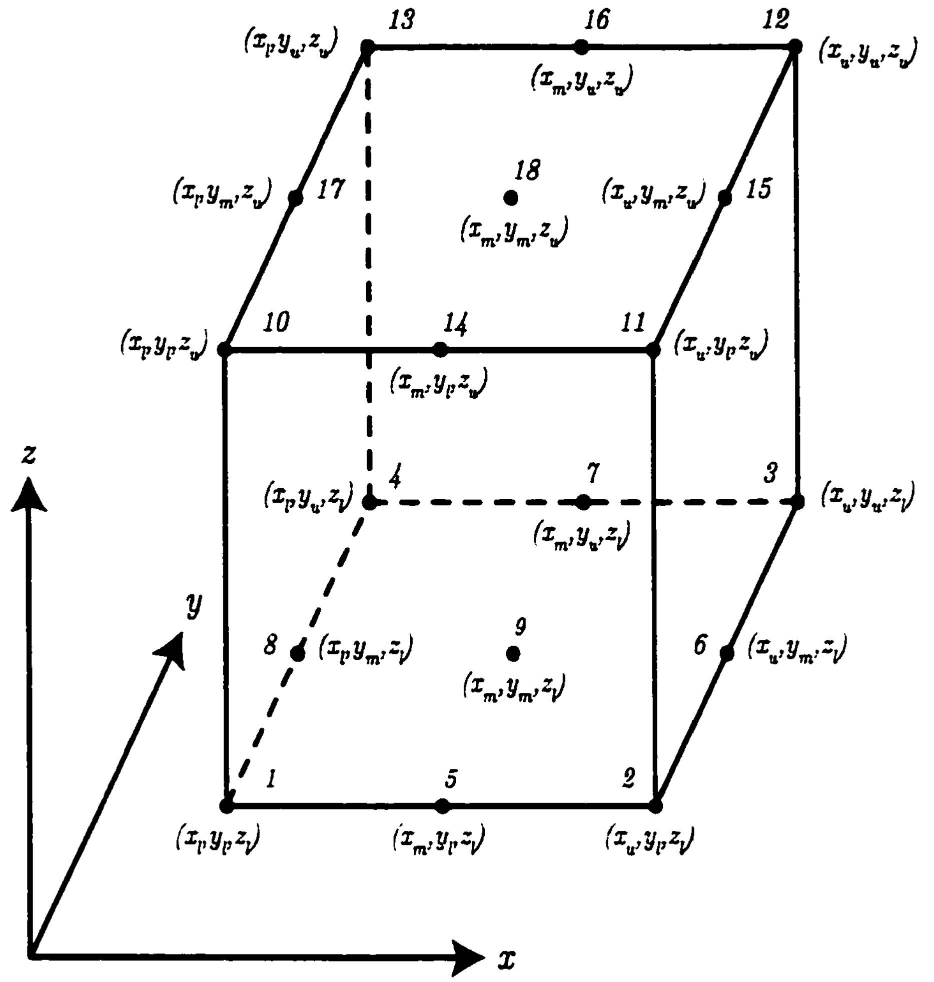

Figure 3.2: Cubic thermal finite element showing local node numbers and coordinates.

differential equation. The trial functions $\bar{u}^0$, $\bar{v}^0$, $\bar{\psi}_x$, and $\bar{\psi}_y$ associated with the mechanical motion are approximated using the same quadratic functions defined in Equation (3.124). To easily incorporate the mechanical motion finite element terms in Equation (3.191), the displacement finite element nodes are aligned with the thermal finite element nodes at the plate centerline as shown in Figure 3.3. This figure shows two thermal finite elements that are adjacent to the plate centerline which is shown as the shaded plane. The thermal finite element nodes are numbered *1* through *27*, with nodes *10* through *18* lying in the centerline plane. Also shown is a mechanical finite element that has nodes numbered 1 through 9. These nodes are aligned with nodes *10* through *18* of the thermal finite elements. This alignment allows the substitution of Eq (3.139) into Equation (3.191) because the current thermal element would share the same x and y nodal coordinates as the mechanical element at the plate centerline. In this case we say the thermal and mechanical elements are *geometrically aligned*. Performing this substitution yields

$$I_T^k = -\left[M_T^k\right]\left\{\dot{\Theta}^k(t)\right\} - \left[K_T^k\right]\left\{\Theta^k(t)\right\} - \left\{F_{QP}^k\right\}\dot{V}^k - \left[C_{TM}^k\right]\left\{\dot{u}^k\right\} \tag{3.195}$$

where

$$\left[C_{TM}^k\right] = T_0 \int_{z_l}^{z_u}\int_{y_l}^{y_u}\int_{x_l}^{x_u} \left[H_T^k\right]^T \left[B_T^e\right] dx dy dz \tag{3.196}$$

$$\left[B_T^e\right] = \left[\begin{array}{cccccc} \beta_x \frac{\partial}{\partial x} - 2\beta_{xy}\frac{\partial}{\partial y} & 2\beta_{xy}\frac{\partial}{\partial x} - \beta_y \frac{\partial}{\partial y} & 0 & z\left(\beta_x\frac{\partial}{\partial x} - 2\beta_{xy}\frac{\partial}{\partial y}\right) & z\left(2\beta_{xy}\frac{\partial}{\partial x} - \beta_y\frac{\partial}{\partial y}\right) \end{array}\right]\left[N^e\right] \tag{3.197}$$

In Equation (3.195), $\left\{\dot{u}^k\right\}$ represents the time rate of change of the nodal displacements and rotations associated with the mechanical finite element that shares the same x and y nodal coordinates as the k^{th} thermal finite element. For a boundary thermal finite element, Equation (3.195) is modified to include the effects of the appropriate boundary condition. The two types of boundary conditions are specified temperature (*essential*) and specified heat flux (*natural*). The effect of different boundary conditions will be illustrated using the k^{th} element that has a boundary located at $x = 0$. In this case, Equation (3.195) is modified to include the boundary condition term at $x = 0$.

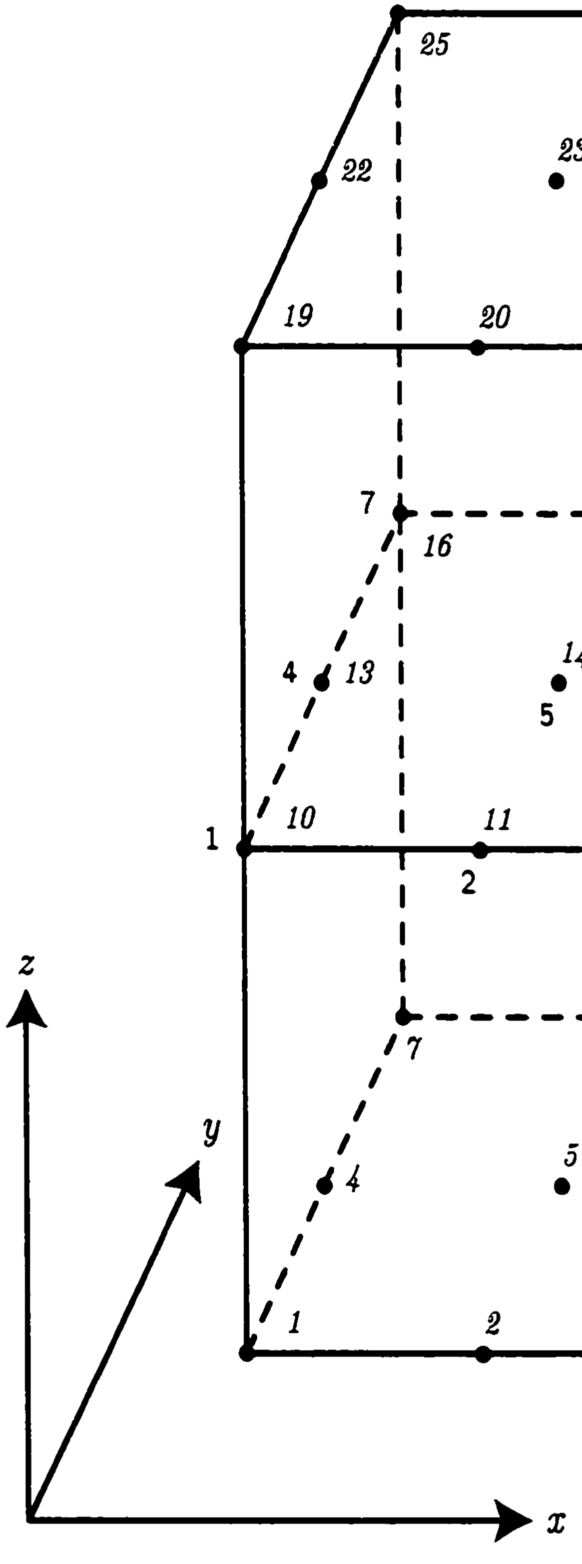

Figure 3.3: Alignment of the mechanical finite element nodes and the thermal finite element nodes at the plate centerline. Also shown is the global nodal numbering convention.

$$
\begin{aligned}
I_T^k &= -\left[M_T^k\right]\left\{\dot{\Theta}_{x_0}^k(t)\right\} - \left[K_T^k\right]\left\{\Theta_{x_0}^k(t)\right\} - \left\{F_{QP}^k\right\}\dot{V}^k - \left[C_{TM}^k\right]\left\{\dot{u}_{x_0}^k\right\} \\
&\quad - \int_{z_l}^{z_u}\int_{y_l}^{y_u}\left(\left[k_x w\frac{\partial\bar{\Theta}}{\partial x} - k_{xy} w\frac{\partial\bar{\Theta}}{\partial y}\right|_{x=0}\right) dydz
\end{aligned} \tag{3.198}
$$

In Equation (3.198), the subscript x_0 indicates that these nodal temperature and displacement vectors are associated with finite elements that include the boundary $x = 0$. For the case of a specified temperature at the boundary, Equation (3.198) can be written as

$$
\begin{aligned}
I_T^k &= -\left[M_T^k\right]\left\{\dot{\Theta}_{x_0}^k(t)\right\} - \left[K_T^k\right]\left\{\Theta_{x_0}^k(t)\right\} - \left\{F_{QP}^k\right\}\dot{V}^k - \left[C_{TM}^k\right]\left\{\dot{u}_{x_0}^k\right\} \\
&\quad - \int_{z_l}^{z_u}\int_{y_l}^{y_u}\left(\left[H_T^k\right]^T(0,y,z)\left[k_x\frac{\partial\left[H_T^k\right]}{\partial x} - k_{xy}\frac{\partial\left[H_T^k\right]}{\partial y}\right|_{x=0}\right) dydz\left\{\Theta_{x_0}^k(t)\right\} \\
&= -\left[M_T^k\right]\left\{\dot{\Theta}_{x_0}^k(t)\right\} - \left[K_{Tx_0}^k\right]\left\{\Theta_{x_0}^k(t)\right\} - \left\{F_{QP}^k\right\}\dot{V}^k - \left[C_{TM}^k\right]\left\{\dot{u}_{x_0}^k\right\}
\end{aligned} \tag{3.199}
$$

where

$$
\left[K_{Tx_0}^k\right] = \left[K_T^k\right] - \int_{z_l}^{z_u}\int_{y_l}^{y_u}\left(\left[H_T^k\right]^T(0,y,z)\left[k_x\frac{\partial\left[H_T^k\right]}{\partial x} - k_{xy}\frac{\partial\left[H_T^k\right]}{\partial y}\right|_{x=0}\right) dydz \tag{3.200}
$$

Similar expressions can be found for specified temperature boundary conditions at $x = a$, $y = 0$, $y = b$, $z = -\frac{1}{2}$, and $z = \frac{1}{2}$. Note that the displacement boundary conditions at $x = 0$ may require constraints on $\left\{\dot{u}_{x_0}^k\right\}$. For the case of specified heat flux at the boundary $x = 0$,

$$
k_x\left.\frac{\partial\bar{\Theta}}{\partial x}\right|_{x=0} = Q_{x_0}(y,z,t) \tag{3.201}
$$

$$
k_{xy}\left.\frac{\partial\bar{\Theta}}{\partial y}\right|_{x=0} = Q_{xy_0}(y,z,t) \tag{3.202}
$$

Equation (3.198) can be written as

$$
\begin{aligned}
I_T^k &= -\left[M_T^k\right]\left\{\dot{\Theta}^k(t)\right\} - \left[K_T^k\right]\left\{\Theta^k(t)\right\} - \left\{F_{QP}^k\right\}\dot{V}^k - \left[C_{TM}^k\right]\left\{\dot{u}^k\right\} - \\
&\quad \int_{z_l}^{z_u}\int_{y_l}^{y_u}\left(\left[H_T^k\right]^T(0,y,z)\left[Q_{x_0} - Q_{xy_0}\right]\right) dydz \\
&= -\left[M_T^k\right]\left\{\dot{\Theta}^k(t)\right\} - \left[K_T^k\right]\left\{\Theta^k(t)\right\} - \left\{F_{QP}^k\right\}\dot{V}^k - \left[C_{TM}^k\right]\left\{\dot{u}^k\right\} - F_{Qx_0}^k
\end{aligned} \tag{3.203}
$$

where for uniform heat fluxes

$$
F_{Q_{x_0}}^k = -\frac{A_{x_0}^k}{12}\begin{bmatrix} 1 & 0 & 0 & 1 & 0 & 0 & 0 & 4 & 0 & 1 & 0 & 0 & 1 & 0 & 0 & 0 & 4 & 0 \end{bmatrix}^T \left(Q_{x_0} - Q_{xy_0}\right) \tag{3.204}
$$

and, for a more general heat flux distribution,

$$F^k_{Q_{x_u}} = -\int_{z_l}^{z_u}\int_{y_l}^{y_u}\left(\left[H^k_T\right]^T(0,y,z)\left[H^k_T\right](0,y,z)\right)dydz\left\{Q^k_{x_u} - Q^k_{xy_u}\right\} \tag{3.205}$$

$$\left\{Q^k_{x_u}\right\} = \begin{bmatrix} {}_1Q^k_{x_u} \\ 0 \\ 0 \\ {}_4Q^k_{x_u} \\ 0 \\ 0 \\ 0 \\ {}_8Q^k_{x_u} \\ 0 \\ {}_{10}Q^k_{x_u} \\ 0 \\ 0 \\ {}_{13}Q^k_{x_u} \\ 0 \\ 0 \\ 0 \\ {}_{17}Q^k_{x_u} \\ 0 \end{bmatrix} \tag{3.206}$$

$$\left\{Q^k_{xy_0}\right\} = \begin{bmatrix} {}_1Q^k_{xy_0} \\ 0 \\ 0 \\ {}_4Q^k_{xy_0} \\ 0 \\ 0 \\ 0 \\ {}_8Q^k_{xy_0} \\ 0 \\ {}_{10}Q^k_{xy_0} \\ 0 \\ 0 \\ {}_{13}Q^k_{xy_0} \\ 0 \\ 0 \\ 0 \\ {}_{17}Q^k_{xy_0} \\ 0 \end{bmatrix} \tag{3.207}$$

In Equation (3.206), ${}_iQ^k_{x_0}$ represents the heat flux in the x direction at $x = 0$ at node i. In Equation (3.207), ${}_iQ^k_{xy_0}$ represents the heat flux in the y direction at $x = 0$ at node i. Note again that the displacement boundary conditions at $x = 0$ may require constraints on $\left\{\dot{u}^k\right\}$. Similar expressions can be found for specified heat flux boundary conditions at $x = a$, $y = 0$, $y = b$, $z = -\frac{1}{2}$, and $z = \frac{1}{2}$. Assembling the residuals from all N_{te} thermal finite elements yields

$$I_T = -[M_T]\left\{\dot{\Theta}\right\} - [K_T]\{\Theta\} - [C_{TM}]\left\{\dot{u}\right\} + \{F_Q\} - [F_{QP}]\left\{\dot{V}\right\} \tag{3.208}$$

where the explicit dependence of $\{\Theta\}$ on time has been omitted for clarity. Equation (3.208) can be solved by setting $I_T = 0$. If the number of elements is large enough the finite element solution will be a good approximation of the actual solution. Setting $I_T = 0$ and rearranging yields

$$[M_T]\left\{\dot{\Theta}\right\} + [K_T]\{\Theta\} + [C_{TM}]\{\dot{u}\} = \{F_Q\} + [F_{QP}]\left\{\dot{V}\right\} \tag{3.209}$$

which is the finite element version of Equation (3.118).

Now if the plate thermal differential equation has been discretized using finite elements, the thermal terms in Equations (3.84) through (3.91) need to be modified to include the finite element approximation of the temperature field. Performing this substitution yields

$$\begin{aligned} N_{Tx}(x,y,t) &= \sum_{k=1}^{N_{tr}} \left(\bar{C}_{11}^k \alpha_x^k + \bar{C}_{12}^k \alpha_y^k + \bar{C}_{16}^k \alpha_{xy}^k\right) \int_{z_{k-1}}^{z_k} \bar{\Theta}^k(x,y,z,t)\, dz \\ &= \sum_{k=1}^{N_{tr}} \left(\bar{C}_{11}^k \alpha_x^k + \bar{C}_{12}^k \alpha_y^k + \bar{C}_{16}^k \alpha_{xy}^k\right) \left(\int_{z_{k-1}}^{z_k} \left[H_T^k(x,y,z)\right] dz\right) \left\{\Theta^k(t)\right\} \end{aligned} \tag{3.210}$$

$$\begin{aligned} N_{Ty}(x,y,t) &= \sum_{k=1}^{N_{tr}} \left(\bar{C}_{12}^k \alpha_x^k + \bar{C}_{22}^k \alpha_y^k + \bar{C}_{26}^k \alpha_{xy}^k\right) \int_{z_{k-1}}^{z_k} \bar{\Theta}^k(x,y,z,t)\, dz \\ &= \sum_{k=1}^{N_{tr}} \left(\bar{C}_{12}^k \alpha_x^k + \bar{C}_{22}^k \alpha_y^k + \bar{C}_{26}^k \alpha_{xy}^k\right) \left(\int_{z_{k-1}}^{z_k} \left[H_T^k(x,y,z)\right] dz\right) \left\{\Theta^k(t)\right\} \end{aligned} \tag{3.211}$$

$$\begin{aligned} N_{Txy}(x,y,t) &= \sum_{k=1}^{N_{tr}} \left(\bar{C}_{16}^k \alpha_x^k + \bar{C}_{26}^k \alpha_y^k + \bar{C}_{66}^k \alpha_{xy}^k\right) \int_{z_{k-1}}^{z_k} \bar{\Theta}^k(x,y,z,t)\, dz \\ &= \sum_{k=1}^{N_{tr}} \left(\bar{C}_{16}^k \alpha_x^k + \bar{C}_{26}^k \alpha_y^k + \bar{C}_{66}^k \alpha_{xy}^k\right) \left(\int_{z_{k-1}}^{z_k} \left[H_T^k(x,y,z)\right] dz\right) \left\{\Theta^k(t)\right\} \end{aligned} \tag{3.212}$$

$$\begin{aligned} M_{Tx}(x,y,t) &= \sum_{k=1}^{N_{tr}} \left(\bar{C}_{11}^k \alpha_x^k + \bar{C}_{12}^k \alpha_y^k + \bar{C}_{16}^k \alpha_{xy}^k\right) \int_{z_{k-1}}^{z_k} \bar{\Theta}^k(x,y,z,t)\, zdz \\ &= \sum_{k=1}^{N_{tr}} \left(\bar{C}_{11}^k \alpha_x^k + \bar{C}_{12}^k \alpha_y^k + \bar{C}_{16}^k \alpha_{xy}^k\right) \left(\int_{z_{k-1}}^{z_k} \left[H_T^k(x,y,z)\right] zdz\right) \left\{\Theta^k(t)\right\} \end{aligned} \tag{3.213}$$

$$\begin{aligned} M_{Ty}(x,y,t) &= \sum_{k=1}^{N_{tr}} \left(\bar{C}_{12}^k \alpha_x^k + \bar{C}_{22}^k \alpha_y^k + \bar{C}_{26}^k \alpha_{xy}^k\right) \int_{z_{k-1}}^{z_k} \bar{\Theta}^k(x,y,z,t)\, zdz \\ &= \sum_{k=1}^{N_{tr}} \left(\bar{C}_{12}^k \alpha_x^k + \bar{C}_{22}^k \alpha_y^k + \bar{C}_{26}^k \alpha_{xy}^k\right) \left(\int_{z_{k-1}}^{z_k} \left[H_T^k(x,y,z)\right] zdz\right) \left\{\Theta^k(t)\right\} \end{aligned} \tag{3.214}$$

$$\begin{aligned} M_{Txy}(x,y,t) &= \sum_{k=1}^{N_{tr}} \left(\bar{C}_{16}^k \alpha_x^k + \bar{C}_{26}^k \alpha_y^k + \bar{C}_{66}^k \alpha_{xy}^k\right) \int_{z_{k-1}}^{z_k} \bar{\Theta}^k(x,y,z,t)\, zdz \\ &= \sum_{k=1}^{N_{tr}} \left(\bar{C}_{16}^k \alpha_x^k + \bar{C}_{26}^k \alpha_y^k + \bar{C}_{66}^k \alpha_{xy}^k\right) \left(\int_{z_{k-1}}^{z_k} \left[H_T^k(x,y,z)\right] zdz\right) \left\{\Theta^k(t)\right\} \end{aligned} \tag{3.215}$$

This can be written in compact form

$$\{\bar{N}_T\} = \sum_{k=1}^{N_{te}} [C_T^k] \int_{z_{k-1}}^{z_k} [\mathcal{H}^k]\, dz \, \{\Theta^k(t)\} \tag{3.216}$$

$$[C_T^k] = \begin{bmatrix} C_{T1}^k & 0 & 0 & 0 & 0 & 0 & 0 & 0 \\ 0 & C_{T1}^k & 0 & 0 & 0 & 0 & 0 & 0 \\ 0 & 0 & 0 & 0 & 0 & 0 & 0 & 0 \\ 0 & 0 & 0 & 0 & 0 & 0 & 0 & 0 \\ 0 & 0 & 0 & 0 & C_{T3}^k & 0 & 0 & 0 \\ 0 & 0 & 0 & 0 & 0 & C_{T1}^k & 0 & 0 \\ 0 & 0 & 0 & 0 & 0 & 0 & C_{T2}^k & 0 \\ 0 & 0 & 0 & 0 & 0 & 0 & 0 & C_{T3}^k \end{bmatrix} \tag{3.217}$$

where

$$C_{T1}^k = (\bar{C}_{11}^k \alpha_x^k - \bar{C}_{12}^k \alpha_y^k - \bar{C}_{16}^k \alpha_{xy}^k) \tag{3.218}$$

$$C_{T2}^k = (\bar{C}_{12}^k \alpha_x^k - \bar{C}_{22}^k \alpha_y^k - \bar{C}_{26}^k \alpha_{xy}^k) \tag{3.219}$$

$$C_{T3}^k = (\bar{C}_{16}^k \alpha_x^k - \bar{C}_{26}^k \alpha_y^k - \bar{C}_{66}^k \alpha_{xy}^k) \tag{3.220}$$

and

$$[\mathcal{H}^k] = \begin{bmatrix} [H_T^k(x,y,z)] \\ [H_T^k(x,y,z)] \\ 0 \\ 0 \\ [H_T^k(x,y,z)] \\ [H_T^k(x,y,z)]\, z \\ [H_T^k(x,y,z)]\, z \\ [H_T^k(x,y,z)]\, z \end{bmatrix} \tag{3.221}$$

In order to substitute Equation (3.216) into Equation (3.150), it must be modified to account for the thermal stress and moment resultant associated with the geometrically aligned mechanical finite element. This can be accomplished by limiting the summation in Equation (3.216) to those thermal finite elements that share the same x and y nodal coordinates with the current mechanical finite element. This restriction yields

$$\{\bar{N}_T^e\} = \sum_{k=1}^{N_{mte}} [C_T^e] \int_{z_{k-1}}^{z_k} [\mathcal{H}^{ke}] \, dz \, \{\Theta^{ke}(t)\} \tag{3.222}$$

where N_{mte} represents the number of thermal finite elements that are geometrically aligned with the current mechanical finite element, and the superscript e denotes that the parameter's value is associated with the current mechanical finite element. Substituting Equation (3.222) into Equation (3.150) yields

$$\begin{aligned} \{F_{MT}^e\} &= \int_{y_l}^{y_u} \int_{x_l}^{x_u} [B^e]^T \sum_{k=1}^{N_{mte}} [C_T^e] \int_{z_{k-1}}^{z_k} [\mathcal{H}^{ke}] \, dz \, \{\Theta^{ke}(t)\} \, dx dy \\ &= [K_{MT}^e] \{\Theta^e(t)\} \end{aligned} \tag{3.223}$$

$$[K_{MT}^e] = \sum_{k=1}^{N_{mte}} \int_{z_{k-1}}^{z_k} \int_{y_l}^{y_u} \int_{x_l}^{x_u} [B^e]^T [C_T^e] [\mathcal{H}^{ke}] \, dx dy dz \tag{3.224}$$

and $\{\Theta^e(t)\}$ represents the assembly of all $\{\Theta^{ke}(t)\}$ into one vector. Using this notation, Equation (3.167) becomes

$$[M_M]\{\ddot{u}\} + [K_M]\{u\} = [F_{MP}]\{V\} - [K_{MT}]\{\Theta\} - \{F_M\} \tag{3.225}$$

To include the effects of damping, Equation (3.225) is modified as follows:

$$[M_M]\{\ddot{u}\} + [C_M]\{\dot{u}\} + [K_M]\{u\} = [F_{MP}]\{V\} - [K_{MT}]\{\Theta\} - \{F_M\} \tag{3.226}$$

where $[C_M]$ is the damping matrix. Note that damping in a composite is anisotropic analogous to stiffness, but not proportional to it. To avoid numerical issues, a small amount of isotropic damping is added to the model. Isotropic damping has the form

$$[C_M] = 2\xi [M_M] V \Omega V^{-1} \tag{3.227}$$

where ξ is the damping coefficient that is applied to all modes, and the matrices V and Ω are found from the eigenvalue decomposition of $[M_M]^{-1} [K_M]$

$$[M_M]^{-1} [K_M] = V \Omega^2 V^{-1} \tag{3.228}$$

This formulation assumes that all modes have the same damping.

Equations (3.209) and (3.226) are the finite element coupled piezothermoelastic equations governing the plate motion and temperature. These equations can be combined into one set of first order differential equations as follows. Define a new generalized state variable

$$q = \begin{Bmatrix} \{\tilde{u}\} \\ \{\dot{\tilde{u}}\} \\ \{\Theta\} \end{Bmatrix} \tag{3.229}$$

Assuming that $\{\tilde{u}\}$ has n_m elements and $\{\Theta\}$ has n_t elements, then q has $2n_m + n_t$ elements. Using this formulation, Equations (3.209) and (3.225) can be combined to yield

$$\mathcal{M}\{\dot{q}\} = \mathcal{K}\{q\} - \mathcal{F}_{MP}\{V\} - \mathcal{F}_{QP}\left\{\dot{V}\right\} - \mathcal{F}_M - \mathcal{F}_Q \tag{3.230}$$

where

$$\mathcal{M} = \begin{bmatrix} I_{n_m} & 0_{n_m \times n_m} & 0_{n_m \times n_t} \\ 0_{n_m \times n_m} & [M_M] & 0_{n_m \times n_t} \\ 0_{n_t \times n_m} & 0_{n_t \times n_m} & [M_T] \end{bmatrix} \tag{3.231}$$

$$\mathcal{K} = \begin{bmatrix} 0_{n_m \times n_m} & I_{n_m} & 0_{n_m \times n_t} \\ -[K_M] & -[C_M] & [K_{MT}] \\ 0_{n_t \times n_m} & -[C_{TM}] & -[K_T] \end{bmatrix} \tag{3.232}$$

$$\mathcal{F}_{MP} = \begin{bmatrix} 0_{n_m \times N_A} \\ [F_{MP}] \\ 0_{n_t \times N_A} \end{bmatrix} \tag{3.233}$$

$$\mathcal{F}_{QP} = \begin{bmatrix} 0_{n_m \times N_A} \\ 0_{n_m \times N_A} \\ [F_{QP}] \end{bmatrix} \tag{3.234}$$

$$\mathcal{F}_M = \begin{bmatrix} 0_{n_m \times 1} \\ \{F_M\} \\ 0_{n_t \times 1} \end{bmatrix} \tag{3.235}$$

$$\mathcal{F}_Q = \begin{bmatrix} 0_{n_m \times 1} \\ 0_{n_m \times 1} \\ \{F_Q\} \end{bmatrix} \tag{3.236}$$

In these equations, I_{n_m} represents the n_m by n_m identity matrix, and $0_{n \times m}$ represents a zero matrix of size n by m. Since this problem is properly constrained, the matrix $\mathcal{M}$ is invertible, which allows the problem to be written in state-space form

$$\{\dot{q}\} = \mathcal{A}\{q\} + \mathcal{B}_V\{V\} + \mathcal{B}_{\dot{V}}\left\{\dot{V}\right\} + \{w\} \tag{3.237}$$

where

$$\mathcal{A} = \mathcal{M}^{-1}\mathcal{K} \tag{3.238}$$

$$\mathcal{B}_V = \mathcal{M}^{-1}\mathcal{F}_{MP} \tag{3.239}$$

$$\mathcal{B}_{\dot{V}} = \mathcal{M}^{-1}\mathcal{F}_{QP} \tag{3.240}$$

$$\{w\} = \mathcal{M}^{-1}(\mathcal{F}_M + \mathcal{F}_Q) \tag{3.241}$$

In this formulation, the variable $\{w\}$ is considered a disturbance input to the system.

3.2.5 Imposing Essential Boundary Conditions

At this point, essential temperature and displacement boundary conditions should be imposed on the system given by Equation (3.237). The temperature essential boundary conditions at the edge of the plate are:

- Zero temperature edge: $\Theta = 0$
- Fixed temperature edge: $\Theta = \Theta_0$

Assume that q_i, $2n_m < i \leq 2n_m + n_t$, is associated with a thermal finite element node located on the boundary. To apply the boundary condition for the case where $q_i \equiv 0$, the differential equation associated with $\dot{q}_i$ is eliminated from the system, since $\dot{q}_i = 0$, and the column of the $\mathcal{A}$ matrix associated with q_i is deleted from the matrix as shown below

$$\{\dot{\bar{q}}\} = \bar{\mathcal{A}}\{\bar{q}\} + \bar{\mathcal{B}}_V\{V\} + \bar{\mathcal{B}}_{\dot{V}}\left\{\dot{V}\right\} + \{\bar{w}\} \tag{3.242}$$

where

$$\{\bar{q}\} = \left\{ \begin{array}{cccccc} q_1 & \cdots & q_{i-1} & q_{i+1} & \cdots & q_{2n_m-n_t} \end{array} \right\}^T \tag{3.243}$$

$$\{\bar{w}\} = \left\{ \begin{array}{cccccc} w_1 & \cdots & w_{i-1} & w_{i+1} & \cdots & w_{2n_m-n_t} \end{array} \right\}^T \tag{3.244}$$

$$\bar{\mathcal{A}} = \begin{bmatrix} \mathcal{A}_{11} & \cdots & \mathcal{A}_{1(i-1)} & \mathcal{A}_{1(i+1)} & \cdots & \mathcal{A}_{1(2n_m-nt)} \\ \vdots & \ddots & \vdots & \vdots & \ddots & \vdots \\ \mathcal{A}_{(i-1)1} & \cdots & \mathcal{A}_{(i-1)(i-1)} & \mathcal{A}_{(i-1)(i+1)} & \cdots & \mathcal{A}_{(i-1)(2n_m-nt)} \\ \mathcal{A}_{(i+1)1} & \cdots & \mathcal{A}_{(i+1)(i-1)} & \mathcal{A}_{(i+1)(i+1)} & \cdots & \mathcal{A}_{(i+1)(2n_m-nt)} \\ \vdots & \ddots & \vdots & \vdots & \ddots & \vdots \\ \mathcal{A}_{(2n_m-nt)1} & \cdots & \mathcal{A}_{(2n_m-nt)(i-1)} & \mathcal{A}_{(2n_m-nt)(i+1)} & \cdots & \mathcal{A}_{(2n_m-nt)(2n_m-nt)} \end{bmatrix} \tag{3.245}$$

$$\bar{\mathcal{B}}_V = \begin{bmatrix} \mathcal{B}_{V11} & \cdots & \mathcal{B}_{V1N_A} \\ \vdots & \ddots & \vdots \\ \mathcal{B}_{V(i-1)1} & \cdots & \mathcal{B}_{V(i-1)N_A} \\ \mathcal{B}_{V(i+1)1} & \cdots & \mathcal{B}_{V(i+1)N_A} \\ \vdots & \ddots & \vdots \\ \mathcal{B}_{V(2n_m-n_t)1} & \cdots & \mathcal{B}_{V(2n_m-n_t)N_A} \end{bmatrix} \tag{3.246}$$

$$\bar{\mathcal{B}}_{\dot{V}} = \begin{bmatrix} \mathcal{B}_{\dot{V}11} & \cdots & \mathcal{B}_{\dot{V}1N_A} \\ \vdots & \ddots & \vdots \\ \mathcal{B}_{\dot{V}(i-1)1} & \cdots & \mathcal{B}_{\dot{V}(i-1)N_A} \\ \mathcal{B}_{\dot{V}(i+1)1} & \cdots & \mathcal{B}_{\dot{V}(i+1)N_A} \\ \vdots & \ddots & \vdots \\ \mathcal{B}_{\dot{V}(2n_m-n_t)1} & \cdots & \mathcal{B}_{\dot{V}(2n_m-n_t)N_A} \end{bmatrix} \tag{3.247}$$

To apply the boundary condition for the case where $q_i = \Theta_0 \neq 0$. the differential equation associated with $\dot{q}_i$ is eliminated from the system. since $\dot{q}_i = 0$. and the column of the $\mathcal{A}$ matrix associated with q_i is multiplied by Θ_0. and the resulting vector is added to the disturbance vector. In this case. the $\mathcal{A}$ matrix is still modified as shown in Equation (3.245). Thus. Equation (3.237) becomes

$$\{\dot{\bar{q}}\} = \bar{\mathcal{A}}\{\bar{q}\} + \bar{\mathcal{B}}_V\{V\} + \bar{\mathcal{B}}_{\dot{V}}\left\{\dot{V}\right\} + \{\bar{w}\} \tag{3.248}$$

and

$$\{\hat{w}\} = \{\bar{w}\} - \left\{ \begin{array}{c} \mathcal{A}_{1i} \\ \vdots \\ \mathcal{A}_{(i-1)i} \\ \mathcal{A}_{(i+1)i} \\ \vdots \\ \mathcal{A}_{(2n_m+n_t)i} \end{array} \right\} \Theta_0 \tag{3.249}$$

The displacement essential boundary conditions at the edge of the plate are:

- Clamped edge: $u^0 = v^0 = w^0 = \psi_x = \psi_y = 0$
- Simply supported edge:

  parallel to x-axis: $w^0 = \psi_x = 0$
  parallel to y-axis: $w^0 = \psi_y = 0$

- Fixed simply supported edge:

  parallel to x-axis: $v^0 = w^0 = \psi_x = 0$
  parallel to y-axis: $u^0 = w^0 = \psi_y = 0$

- Symmetric edge:

  parallel to x-axis: $v^0 = \psi_y = 0$
  parallel to y-axis: $u^0 = \psi_x = 0$

- Free edge: none

To apply the boundary condition for the case where $q_i = 0$, $1 < i \leq n_m$, is associated with a displacement finite element, the following row and column operations are applied. The differential equations associated with $\dot{q}_i$ and $\dot{q}_{i+n_m} = \ddot{q}_i$ are eliminated from the system, since $\dot{q}_i = \ddot{q}_i = 0$, and the columns of the $\mathcal{A}$ matrix associated with q_i and $\dot{q}_{i+n_m}$ are deleted from the matrix as shown below

$$\left\{\dot{\hat{q}}\right\} = \hat{\mathcal{A}}\{\hat{q}\} + \hat{\mathcal{B}}_V\{V\} + \hat{\mathcal{B}}_{\dot{V}}\left\{\dot{V}\right\} + \{\hat{w}\} \tag{3.250}$$

where

$$\{\hat{q}\} = \left\{ \begin{array}{cccccccc} q_1 & \cdots & q_{i-1} & q_{i+1} & \cdots & q_{i+n_m-1} & q_{i+n_m-1} & \cdots & q_{2n_m+n_t} \end{array} \right\}^T \tag{3.251}$$

$$\{\hat{w}\} = \left\{ \begin{array}{cccccccc} w_1 & \cdots & w_{i-1} & w_{i+1} & \cdots & w_{i+n_m-1} & w_{i+n_m-1} & \cdots & w_{2n_m+n_t} \end{array} \right\}^T \tag{3.252}$$

$$\hat{\mathcal{A}} = \begin{bmatrix} \hat{\mathcal{A}}_{11} & \hat{\mathcal{A}}_{12} & \hat{\mathcal{A}}_{13} \\ \hat{\mathcal{A}}_{21} & \hat{\mathcal{A}}_{22} & \hat{\mathcal{A}}_{23} \\ \hat{\mathcal{A}}_{31} & \hat{\mathcal{A}}_{32} & \hat{\mathcal{A}}_{33} \end{bmatrix} \tag{3.253}$$

$$\hat{\mathcal{A}}_{11} = \begin{bmatrix} \mathcal{A}_{11} & \cdots & \mathcal{A}_{1(i-1)} \\ \vdots & \ddots & \vdots \\ \mathcal{A}_{(i-1)1} & \cdots & \mathcal{A}_{(i-1)(i-1)} \end{bmatrix} \tag{3.254}$$

$$\hat{\mathcal{A}}_{12} = \begin{bmatrix} \mathcal{A}_{1(i+1)} & \cdots & \mathcal{A}_{1(i+n_m-1)} \\ \vdots & \ddots & \vdots \\ \mathcal{A}_{(i-1)(i+1)} & \cdots & \mathcal{A}_{(i-1)(i+n_m-1)} \end{bmatrix} \tag{3.255}$$

$$\hat{\mathcal{A}}_{13} = \begin{bmatrix} \mathcal{A}_{1(i+n_m+1)} & \cdots & \mathcal{A}_{1(2n_m+n_t)} \\ \vdots & \ddots & \vdots \\ \mathcal{A}_{(i-1)(i+n_m+1)} & \cdots & \mathcal{A}_{(i-1)(2n_m+n_t)} \end{bmatrix} \tag{3.256}$$

$$\hat{\mathcal{A}}_{21} = \begin{bmatrix} \mathcal{A}_{(i+1)1} & \cdots & \mathcal{A}_{(i+1)(i-1)} \\ \vdots & \ddots & \vdots \\ \mathcal{A}_{(i+n_m-1)1} & \cdots & \mathcal{A}_{(i+n_m-1)(i-1)} \end{bmatrix} \tag{3.257}$$

$$\hat{\mathcal{A}}_{22} = \begin{bmatrix} \mathcal{A}_{(i+1)(i+1)} & \cdots & \mathcal{A}_{(i+1)(i+n_m-1)} \\ \vdots & \ddots & \vdots \\ \mathcal{A}_{(i+n_m-1)(i+1)} & \cdots & \mathcal{A}_{(i+n_m-1)(i+n_m-1)} \end{bmatrix} \tag{3.258}$$

$$\hat{\mathcal{A}}_{23} = \begin{bmatrix} \mathcal{A}_{(i+1)(i+n_m+1)} & \cdots & \mathcal{A}_{(i+1)(2n_m+n_t)} \\ \vdots & \ddots & \vdots \\ \mathcal{A}_{(i+n_m-1)(i+n_m+1)} & \cdots & \mathcal{A}_{(i+n_m-1)(2n_m+n_t)} \end{bmatrix} \tag{3.259}$$

$$\hat{\mathcal{A}}_{31} = \begin{bmatrix} \mathcal{A}_{(i+n_m+1)1} & \cdots & \mathcal{A}_{(i+n_m+1)(i-1)} \\ \vdots & \ddots & \vdots \\ \mathcal{A}_{(2n_m+n_t)1} & \cdots & \mathcal{A}_{(2n_m+n_t)(i-1)} \end{bmatrix} \tag{3.260}$$

$$\hat{\mathcal{A}}_{32} = \begin{bmatrix} \mathcal{A}_{(i+n_m+1)(i+1)} & \cdots & \mathcal{A}_{(i+n_m+1)(i+n_m-1)} \\ \vdots & \ddots & \vdots \\ \mathcal{A}_{(2n_m+n_t)(i+1)} & \cdots & \mathcal{A}_{(2n_m+n_t)(i+n_m-1)} \end{bmatrix} \tag{3.261}$$

$$\hat{\mathcal{A}}_{33} = \begin{bmatrix} \mathcal{A}_{(i+n_m+1)(i+n_m+1)} & \cdots & \mathcal{A}_{(i+n_m+1)(2n_m+n_t)} \\ \vdots & \ddots & \vdots \\ \mathcal{A}_{(2n_m+n_t)(i+n_m+1)} & \cdots & \mathcal{A}_{(2n_m+n_t)(2n_m+n_t)} \end{bmatrix} \tag{3.262}$$

$$\hat{\mathcal{B}}_{V} = \begin{bmatrix} \mathcal{B}_{V11} & \cdots & \mathcal{B}_{V1N_A} \\ \vdots & \ddots & \vdots \\ \mathcal{B}_{V(i-1)1} & \cdots & \mathcal{B}_{V(i-1)N_A} \\ \mathcal{B}_{V(i+1)1} & \cdots & \mathcal{B}_{V(i+1)N_A} \\ \vdots & \ddots & \vdots \\ \mathcal{B}_{V(i+n_m-1)1} & \cdots & \mathcal{B}_{V(i+n_m-1)N_A} \\ \mathcal{B}_{V(i+n_m+1)1} & \cdots & \mathcal{B}_{V(i+n_m+1)N_A} \\ \vdots & \ddots & \vdots \\ \mathcal{B}_{V(2n_m+n_t)1} & \cdots & \mathcal{B}_{V(2n_m+n_t)N_A} \end{bmatrix} \tag{3.263}$$

$$\hat{\mathcal{B}}_{\dot{V}} = \begin{bmatrix} \mathcal{B}_{\dot{V}11} & \cdots & \mathcal{B}_{\dot{V}1N_A} \\ \vdots & \ddots & \vdots \\ \mathcal{B}_{\dot{V}(i-1)1} & \cdots & \mathcal{B}_{\dot{V}(i-1)N_A} \\ \mathcal{B}_{\dot{V}(i+1)1} & \cdots & \mathcal{B}_{\dot{V}(i+1)N_A} \\ \vdots & \ddots & \vdots \\ \mathcal{B}_{\dot{V}(i+n_m-1)1} & \cdots & \mathcal{B}_{\dot{V}(i+n_m-1)N_A} \\ \mathcal{B}_{\dot{V}(i+n_m+1)1} & \cdots & \mathcal{B}_{\dot{V}(i+n_m+1)N_A} \\ \vdots & \ddots & \vdots \\ \mathcal{B}_{\dot{V}(2n_m+n_t)1} & \cdots & \mathcal{B}_{\dot{V}(2n_m+n_t)N_A} \end{bmatrix} \tag{3.264}$$

Using these three methods to apply the thermal and displacement plate essential boundary conditions yields a state-space model that is suitable for open loop control. Note that, while these methods are mathematically correct. numerically it is best to apply the essential boundary conditions to Equations (3.225) and (3.209) using methods similar to those presented in this section. multiply the resulting reduced-order differential equations by the inverse of the reduced-order mass matrices $\hat{M}_M^{-1}$ and $\hat{M}_T^{-1}$. respectively. then form the state space system associated with the generalized coordinate q. This is because the reduced order matrices used in the computations improve the numerical results. For closed loop control analysis. a sensor model needs to be added.

3.2.6 Sensor Equation

This subsection develops the output equations for the k^{th} piezoelectric sensor. Substitution of $[e]^k = [d]^k [C]^k$ into Equation (3.2) yields

$$\{D\}^k = [d]^k [C]^k \{\hat{\varepsilon}\}^k + [\epsilon]^k \{E\}^k - \{\hat{p}\}^k \Theta^k \tag{3.265}$$

In the plate sensor configuration. charge is only collected in the z-direction. and the applied electric field $\{E\}^k$ is zero. Introducing these constraints along with Equation (3.12). one can write Equation (3.265) as

$$D_3^k = \{d\}^k [C]^k \{\hat{\varepsilon}\}^k + \{p_z\}^k \Theta^k \tag{3.266}$$

Transforming $\{\hat{\varepsilon}\}^k$ into $\{\varepsilon\}^k$. the Equation (3.266) becomes

$$D_3^k = \{d\}^k \left[\bar{C}\right]^k \{\varepsilon\}^k + \{p_z\}^k \Theta^k \tag{3.267}$$

where

$$\left[\bar{C}\right]^k = [C]^k [R] [T]^k [R]^{-1} \tag{3.268}$$

For the case where a temperature gradient exists in the 3-direction (z). Equation (3.267) is modified to average the temperature over the thickness of the piezoelectric sensor

$$D_3^k = \{d\}^k \left[\bar{C}\right]^k \{\varepsilon\}^k + \{p_z\}^k \frac{1}{h_k} \int_{z_{k-1}}^{z_k} \Theta^k dz \tag{3.269}$$

where z_{k-1} and z_k are the z distance from the midplane to the bottom and top surfaces of the sensor and $h_k = z_k - z_{k-1}$ is the thickness of the sensor. Substituting Equation (3.57) into Equation

(3.269) gives

$$D_3^k = \left(\{d\}^k\right)^T \left[\tilde{C}\right]^k \left(\{\varepsilon^0\} + z_k^0 \{\varkappa\}\right) + \{p_z\}^k \frac{1}{h_k} \int_{z_{k-1}}^{z_k} \Theta^k dz \tag{3.270}$$

where z_k^0 is the z distance from the midplane of the laminate to the midplane of the k^{th} layer piezoelectric sensor patch. The closed circuit charge measured through the electrodes of a sensor patch in the k^{th} layer is [23]

$$\mathrm{q}^k = \frac{1}{2}\left[\int_R D_z^k dA\big|_{z=z_k} - \int_R D_z^k dA\big|_{z=z_{k-1}}\right] \tag{3.271}$$

where R is the effective surface electrode, which defines the integration domain where all the points are covered with surface electrode on both sides of the piezoelectric patch. The electric charge generated by mechanical strain and temperature changes will be detected only if the charge is collected through the effective surface electrode. In the present work, it is assumed that the effective surface electrode is the entire area of the piezoelectric sensor patch. Use of Equation (3.269) in Equation (3.271) yields

$$\mathrm{q}^k = \int_R \left\langle \left(\{d\}^k\right)^T \left[\tilde{C}\right]^k \left(\{\varepsilon^0\} + z_k^0 \{\varkappa\}\right) + \{p_z\}^k \frac{1}{h_k} \int_{z_{k-1}}^{z_k} \Theta^k dz \right\rangle dA \tag{3.272}$$

which can be written as

$$\mathrm{q}^k = \int_R \left(\{d\}^k\right)^T \left[\tilde{C}\right]^k \mathcal{H}\{\bar{u}\}\, dA - \int_R \{p_z\}^k \frac{1}{h_k} \int_{z_{k-1}}^{z_k} \Theta^k dz dA \tag{3.273}$$

where $\mathcal{H}$ is an operator matrix defined by

$$\mathcal{H} = \begin{bmatrix} \frac{\partial}{\partial x} & 0 & 0 & z_k^0 \frac{\partial}{\partial x} & 0 \\ 0 & \frac{\partial}{\partial y} & 0 & 0 & z_k^0 \frac{\partial}{\partial y} \\ 0 & 0 & 0 & 0 & 0 \\ 0 & 0 & \frac{\partial}{\partial y} & 0 & 1 \\ 0 & 0 & \frac{\partial}{\partial x} & 1 & 0 \\ \frac{\partial}{\partial y} & \frac{\partial}{\partial x} & 0 & z_k^0 \frac{\partial}{\partial y} & z_k^0 \frac{\partial}{\partial x} \end{bmatrix} \tag{3.274}$$

Since $\{d\}^k$, $\left[\tilde{C}\right]^k$, and $\{p_3\}^k$ are constants, they can be removed from under the integral sign, so Equation (3.273) can be written as

$$\mathrm{q}^k = \left(\{d\}^k\right)^T \left[\tilde{C}\right]^k \int_R \mathcal{H}\{\bar{u}\}\, dA - \{p_z\}^k \frac{1}{h_k} \int_R \int_{z_{k-1}}^{z_k} \Theta^k dz dA \tag{3.275}$$

In terms of the finite element model, Equation (3.275) becomes

$$q^k = \left(\{d\}^k\right)^T \left[\tilde{C}\right]^k \bar{\mathcal{H}}\{\tilde{u}\}^k + \{p_z\}^k \bar{\mathcal{J}}\{\Theta\}^k \tag{3.276}$$

where

$$\bar{\mathcal{H}} = \sum_{e=1}^{N_{sm}} \int_{A_e} \mathcal{H}[N^e]\, dA \tag{3.277}$$

$$\bar{\mathcal{J}} = \sum_{k=1}^{N_{st}} \int_{V_e} \frac{1}{h_k}\left[H_T^k\right] dV \tag{3.278}$$

and $\{\tilde{u}\}^k$, $\{\Theta\}^k$, N_{sm}, and N_{st} represent the nodal displacements, temperatures, number of mechanical finite elements, and number of thermal finite elements associated with the k^{th} sensor patch, respectively. The current associated with the k^{th} sensor patch is given by

$$i^k(t) = \frac{dq^k}{dt} \tag{3.279}$$

In terms of the finite element model, Equation (3.279) becomes

$$i^k = \left(\{d\}^k\right)^T \left[\tilde{C}\right]^k \bar{\mathcal{H}}\{\dot{\tilde{u}}\}^k - \{p_z\}^k \bar{\mathcal{J}}\left\{\dot{\Theta}\right\}^k \tag{3.280}$$

Solving Equation (3.209) for $\dot{\Theta}$ and substituting into Equation (3.280) yields

$$i^k = \left(\{d\}^k\right)^T \left[\tilde{C}\right]^k \bar{\mathcal{H}}\{\dot{\tilde{u}}\}^k - \{p_z\}^k \bar{\mathcal{J}}\left\{[M_T]^{-1}\left(-[K_T]\{\Theta\} - [C_{TM}]\{\dot{\tilde{u}}\} - \{F_Q\}\right)\right\}^k \tag{3.281}$$

In terms of the generalized state variable defined in Equation (3.229), Equations (3.276) and (3.281) for the k^{th} piezoelectric sensor become

$$q^k = \mathcal{C}_q^k\{q^k\} \tag{3.282}$$

$$i^k = \mathcal{C}_i^k\{q^k\} - \{p_z\}^k \bar{\mathcal{J}}\left([M_T]^k\right)^{-1}\{F_Q\}^k \tag{3.283}$$

where

$$\mathcal{C}_q^k = \begin{bmatrix} \left(\{d\}^k\right)^T \left[\tilde{C}\right]^k \bar{\mathcal{H}} & 0_{1\times n_m} & \{p_z\}^k \bar{\mathcal{J}} \end{bmatrix} \tag{3.284}$$

and

$$\mathcal{C}_i^k = \begin{bmatrix} 0_{1\times n_m} & \left(\{d\}^k\right)^T \left[\tilde{C}\right]^k \bar{\mathcal{H}} - \{p_z\}^k \bar{\mathcal{J}}\left([M_T]^k\right)^{-1}[C_{TM}]^k & -\{p_z\}^k \bar{\mathcal{J}}\left([M_T]^k\right)^{-1}[K_T]^k \end{bmatrix} \tag{3.285}$$

Using Equations (3.282) and (3.283), an output equation can be added to the linear model given by Equation (3.237). For the case of N_S sensors, with both charge and current as measured outputs, the output equation, $\{y\}$, is

$$\{y\} = \mathcal{C}\,\{q\} + \{v\} \tag{3.286}$$

where

$$\mathcal{C} = \begin{bmatrix} \mathcal{C}_q^1 \\ \mathcal{C}_i^1 \\ \vdots \\ \mathcal{C}_q^{N_S} \\ \mathcal{C}_i^{N_S} \end{bmatrix} \tag{3.287}$$

and

$$\{v\} = \begin{bmatrix} 0 & v_i^1 & \cdots & 0 & v_i^{N_S} \end{bmatrix}^T \tag{3.288}$$

$$v_i^k = \{p_z\}^k \bar{\mathcal{J}} \left(M_T^{\,k} \right)^{-1} \{F_Q\}^k \tag{3.289}$$

In this formulation, v is treated as sensor noise. Additional outputs, such as the plate center deflection, can be added to Equation (3.286) by including the appropriate row in the $\mathcal{C}$ matrix. With this formulation the state-space model of the system is

$$\{\dot{q}\} = \mathcal{A}\,\{q\} + \mathcal{B}_V\,\{V\} + \mathcal{B}_{\dot{V}}\left\{\dot{V}\right\} + \{w\} \tag{3.290}$$

$$\{y\} = \mathcal{C}\,\{q\} + \{v\} \tag{3.291}$$

Once the essential boundary conditions are applied to Equations (3.237) and (3.286), the resulting state-space model is suitable for control system design and analysis.

3.2.7 Voltage Rate Output

To implement the heat generated in a piezoelectric actuator due to the rate of change of the electric field, we need to determine an expression for the rate of change of the voltage input to the actuator, since

$$\dot{E} = \frac{d}{dt}\left(\frac{V}{h}\right) = \frac{1}{h}\dot{V} \tag{3.292}$$

where h is the actuator thickness and $\dot{V}$ is the time rate of change of the voltage applied to the actuator which, in a closed-loop control system, is the voltage computed by the control law. In the configurations considered in this work, the control voltage is a function of the sensor charge and current outputs multiplied by their respective feedback gains and summed. Therefore, the time rate of change of the voltage is a function of the current output multiplied by the charge feedback gain summed with the time rate of change of the current multiplied by the current feedback gain. The expression for the current output of the sensor is given by Equation (3.283). The expression for the time rate of change of the current can be found by taking the derivative with respect to time of Equation (3.281)

$$\frac{di^k}{dt} = \left(\{d\}^k\right)^T \left[\bar{C}\right]^k \bar{\mathcal{H}} \left\{\dddot{u}\right\}^k - \{p_z\}^k \bar{\mathcal{J}} \left\{[M_T]^{-1} \left(-[K_T]\left\{\dot{\Theta}\right\} - [C_{TM}]\left\{\ddot{u}\right\} - \left\{\frac{dF_Q}{dt}\right\}\right)\right\}^k \tag{3.293}$$

Using Equation (3.226) to solve for $\left\{\dddot{u}\right\}^k$ yields

$$\left\{\dddot{u}\right\}^k = \left\{[M_M]^{-1}\left(-[C_M]\left\{\ddot{u}\right\} - [K_M]\{\dot{u}\} + [F_{MP}]\{V\} - [K_{MT}]\{\Theta\} - \{F_M\}\right)\right\}^k \tag{3.294}$$

For a piezoelectric sensor layer, the applied voltage, V, is zero which yields

$$\left\{\dddot{u}\right\}^k = \left\{[M_M]^{-1}\left(-[C_M]\left\{\ddot{u}\right\} - [K_M]\{\dot{u}\} + [K_{MT}]\{\Theta\} + \{F_M\}\right)\right\}^k \tag{3.295}$$

Substitution for $\left\{\ddot{\bar{u}}\right\}^k$ and $\left\{\dot{\Theta}\right\}^k$ yields

$$\begin{aligned}
\frac{di^k}{dt} = & -\left(\{d\}^k\right)^T \left[\bar{C}\right]^k \bar{\mathcal{H}} \left([M_M]^k\right)^{-1} \left([K_M]^k \{\bar{u}\}^k + [C_M]^k \{\dot{\bar{u}}\}^k\right) \\
& + \{p_z\}^k \bar{\mathcal{J}} \left([M_T]^k\right)^{-1} [C_{TM}]^k \left([M_M]^k\right)^{-1} \left([K_M]^k \{\bar{u}\}^k + [C_M]^k \{\dot{\bar{u}}\}^k\right) \\
& - \left(\{d\}^k\right)^T \left[\bar{C}\right]^k \bar{\mathcal{H}} \left([M_M]^k\right)^{-1} [K_{MT}]^k \{\Theta\}^k \\
& - \{p_z\}^k \bar{\mathcal{J}} \left([M_T]^k\right)^{-1} [C_{TM}]^k \left([M_M]^k\right)^{-1} [K_{MT}]^k \{\Theta\}^k \\
& + \{p_z\}^k \bar{\mathcal{J}} \left([M_T]^k\right)^{-1} [K_T]^k \left([M_T]^k\right)^{-1} [C_{TM}]^k \{\dot{\bar{u}}\}^k \\
& - \{p_z\}^k \bar{\mathcal{J}} \left([M_T]^k\right)^{-1} [K_T]^k \left([M_T]^k\right)^{-1} [K_T]^k \{\Theta\}^k \\
& - \left(\{d\}^k\right)^T \left[\bar{C}\right]^k \bar{\mathcal{H}} \left([M_M]^k\right)^{-1} \{F_M\}^k \\
& - \{p_z\}^k \bar{\mathcal{J}} \left([M_T]^k\right)^{-1} [C_{TM}]^k \left([M_M]^k\right)^{-1} \{F_M\}^k \\
& - \{p_z\}^k \bar{\mathcal{J}} \left([M_T]^k\right)^{-1} [K_T]^k \{F_Q\}^k \\
& - \{p_z\}^k \bar{\mathcal{J}} \left([M_T]^k\right)^{-1} \left\{\frac{dF_Q}{dt}\right\}^k
\end{aligned} \tag{3.296}$$

If the plate is exposed to an external thermal heat source, this model requires an estimate of $\left\{\frac{dF_Q}{dt}\right\}$. In terms of the generalized state variable defined in Equation (3.229), Equation (3.296) for the k^{th} piezoelectric sensor becomes.

$$\begin{aligned}
\frac{di^k}{dt} = & \; C^k_{\frac{di}{dt}} \{q^k\} - \left(\{d\}^k\right)^T \left[\bar{C}\right]^k \bar{\mathcal{H}} \left([M_M]^k\right)^{-1} \{F_M\}^k \\
& - \{p_z\}^k \bar{\mathcal{J}} \left([M_T]^k\right)^{-1} [C_{TM}]^k \left([M_M]^k\right)^{-1} \{F_M\}^k \\
& - \{p_z\}^k \bar{\mathcal{J}} \left([M_T]^k\right)^{-1} [K_T]^k \{F_Q\}^k \\
& - \{p_z\}^k \bar{\mathcal{J}} \left([M_T]^k\right)^{-1} \left\{\frac{dF_Q}{dt}\right\}^k
\end{aligned} \tag{3.297}$$

$$C^k_{\frac{di}{dt}} = \left[\begin{array}{ccc} {}_1C^k_{\frac{di}{dt}} & {}_2C^k_{\frac{di}{dt}} & {}_3C^k_{\frac{di}{dt}} \end{array}\right] \tag{3.298}$$

$${}_1C^k_{\frac{di}{dt}} = \left(-\left(\{d\}^k\right)^T \left[\bar{C}\right]^k \bar{\mathcal{H}} \left([M_M]^k\right)^{-1} + \{p_z\}^k \bar{\mathcal{J}} \left([M_T]^k\right)^{-1} [C_{TM}]^k \left([M_M]^k\right)^{-1}\right) [K_M]^k \tag{3.299}$$

$$\begin{aligned}
{}_2C^k_{\frac{di}{dt}} = & \left(-\left(\{d\}^k\right)^T \left[\bar{C}\right]^k \bar{\mathcal{H}} \left([M_M]^k\right)^{-1} - \{p_z\}^k \bar{\mathcal{J}} \left([M_T]^k\right)^{-1} [C_{TM}]^k \left([M_M]^k\right)^{-1}\right) [C_M]^k \\
& + \{p_z\}^k \bar{\mathcal{J}} \left([M_T]^k\right)^{-1} [K_T]^k \left([M_T]^k\right)^{-1} [C_{TM}]^k
\end{aligned} \tag{3.300}$$

$$
{}_3C^k_{\frac{dv}{dt}} = \left(\left(\{d\}^k\right)^T \left[\bar{C}\right]^k \bar{\mathcal{H}} \left([M_M]^k\right)^{-1} - \{p_z\}^k \bar{\mathcal{J}} \left([M_T]^k\right)^{-1} [C_{TM}]^k \left([M_M]^k\right)^{-1}\right) [K_{MT}]^k + \{p_z\}^k \bar{\mathcal{J}} \left([M_T]^k\right)^{-1} [K_T]^k \left([M_T]^k\right)^{-1} [K_T]^k \tag{3.301}
$$

To incorporate the voltage rate output into Equation (A.77), Equations (3.287), (3.288), and (3.289) become

$$
C = \begin{bmatrix} C^1_q \\ C^1_i \\ C^1_{\frac{dv}{dt}} \\ \vdots \\ C^{N_S}_q \\ C^{N_S}_i \\ C^{N_S}_{\frac{dv}{dt}} \end{bmatrix} \tag{3.302}
$$

$$
\{v\} = \begin{bmatrix} 0 & v^1_i & v^1_{\frac{dv}{dt}} & \cdots & 0 & v^{N_S}_i & v^{N_S}_{\frac{dv}{dt}} \end{bmatrix}^T
$$

$$
\begin{aligned}
v^k_{\frac{dv}{dt}} = {} & \{p_z\}^k \bar{\mathcal{J}} \left([M_T]^k\right)^{-1} \{F_Q\}^k - \left(\{d\}^k\right)^T \left[\bar{C}\right]^k \bar{\mathcal{H}} \left([M_M]^k\right)^{-1} \{F_M\}^k \\
& - \{p_z\}^k \bar{\mathcal{J}} \left([M_T]^k\right)^{-1} [C_{TM}]^k \left([M_M]^k\right)^{-1} \{F_M\}^k \\
& - \{p_z\}^k \bar{\mathcal{J}} \left([M_T]^k\right)^{-1} [K_T]^k \{F_Q\}^k \\
& - \{p_z\}^k \bar{\mathcal{J}} \left([M_T]^k\right)^{-1} \left\{\frac{dF_Q}{dt}\right\}^k
\end{aligned} \tag{3.303}
$$

3.3 Numerical Results

In the present study, all computations are carried out in double precision on a Micron Millenium Max 733 MHz Pentium III with 768 MB of RAM using MATLAB V6.1 [48]. To verify the current finite element model two case studies were performed.

1. A model of a simply supported aluminum plate subjected to a thermal impact was analyzed. The mechanical and steady state thermal responses are compared with the results generated using the analytical solution developed in Chapter 2. An aluminum plate was chosen for this study because the mechanical response reaches steady-state much quicker than a

graphite/epoxy plate. which reduces the time required to simulate the response to steady-state. See Figures 2.1 and 2.6 for a comparison of the quasistatic response of an aluminum and graphite/epoxy plate.

2. A model of a clamped smart plate composed of graphite/epoxy and PZT layers subjected to a mechanical impulse was analyzed. The open loop and closed loop responses are compared with the results published in [24].

3.3.1 Case Study 1: Simply Supported Aluminum Plate Subject to a Thermal Shock

To validate the model for the study of coupled thermomechanical problems. a finite element model of a simply supported aluminum plate was developed using the equations derived in this chapter. The plate dimensions. mechanical properties. thermal properties (see Table 2.1 for material properties). and all boundary conditions [Equations (2.6) and (2.7)] were the same as those used in Chapter 2. Because of biaxial symmetry only a quarter of the plate was analyzed. The quarter plate was modeled by a $4 \times 4 \times 12$ mesh (x. y. and z directions. respectively) resulting in 405×405 global mechanical mass and stiffness matrices. 1053×1053 global thermal mass and stiffness matrices. and thermo-mechanical coupling matrices of consistent dimensional size. To insure that the fully coupled model contained no spurious right half-plane poles due to lack of numerical precision. mechanical damping was added to the model using Equation (3.227). For better comparison to the analytical solution results of Chapter 2. which assumed no material damping. a very small damping coefficient $\zeta = 0.00001$ (0.001%) on all mechanical vibration modes was assumed. Applying the mechanical and thermal essential boundary conditions. and forming the coupled thermo-mechanical model yielded a state-space sytem with 1504 states. The input to the model was the heat flux at the top of the plate. and the outputs were the center plate deflection and the temperature at the thermal nodes at the center of the plate. For better comparison. the analytical solution model used 12 finite elements in the z direction instead of 24 finite elements as used in Chapter 2. Both models were subjected to a unit heat flux of $1\frac{\mathrm{Btu}}{\mathrm{h\,ft^2}}$. and the mechanical and thermal responses were compared. Figures 3.4 and 3.5 show a comparison of the vertical displacement (*inches*) at the center of the plate using the two different solution methods. Figure 3.4 indicates that the quasistatic deflection shows good agreement, and the dynamic response shows good agreement initially but diverges as time progresses. Figure 3.5 details the response from 0.09 seconds to 0.1 seconds illustrating the divergence of the responses. Figure 3.6 shows a comparison of the power spectral density of the two responses compared in Figure 3.4. This plot illustrates that the responses share the same power spectral density at low frequencies but diverge starting around 2500 Hz, with significant divergence above 12500 Hz. This is mainly due to the differences between classical plate theory and the 1^{st} order shear theory used in the finite element model. Figure 3.7 shows a comparison of the change in temperature ($^\circ F$) as a function of z at the center of the plate using the two different solution methods for $t = 0.1$ seconds. Note that the difference between the two changes in temperature is nearly constant as a function of z and averages 2.7%. This difference is attributable to the more accurate modeling of the thermal heat flux in the x and y directions in the finite element model.

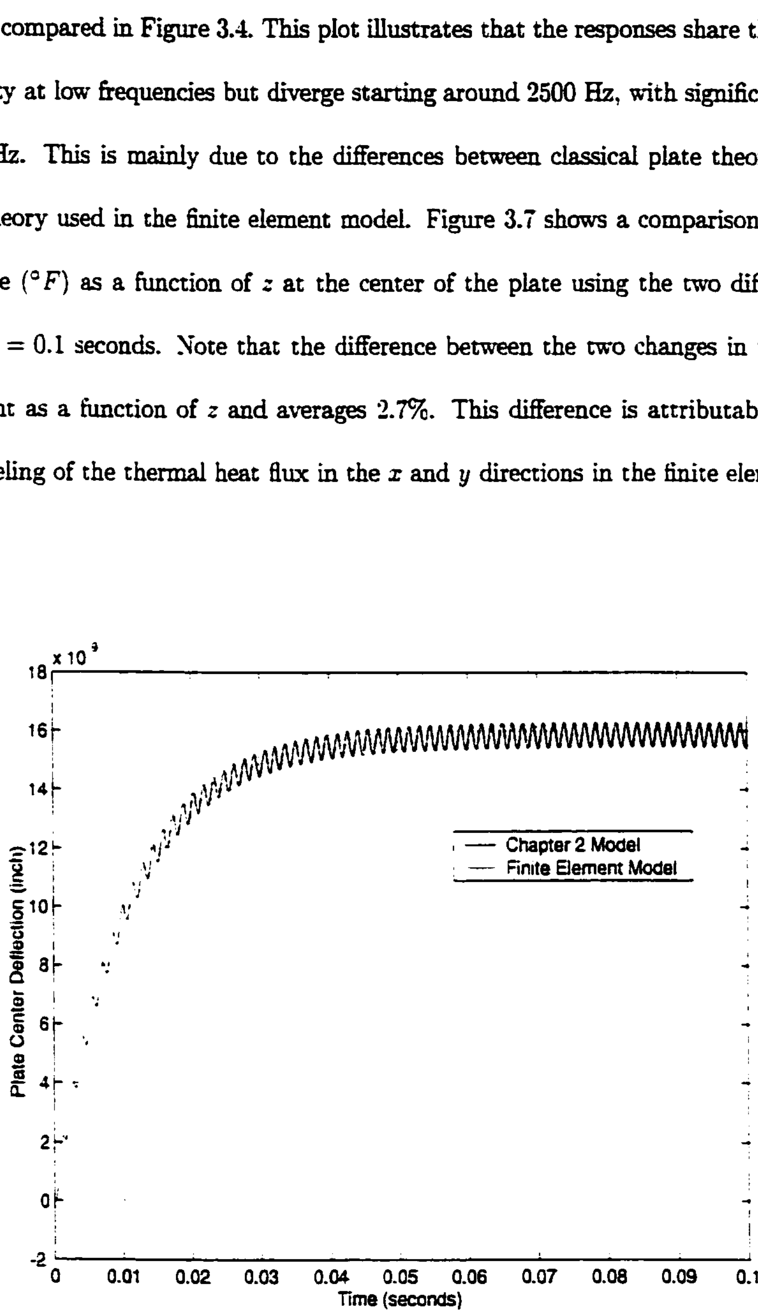

Figure 3.4: Comparison of the analytical and the finite element solutions: plate vertical deflection (in) per unit heat flux $\left(\frac{\mathrm{Btu}}{\mathrm{h\,ft^2}}\right)$ at the plate center.

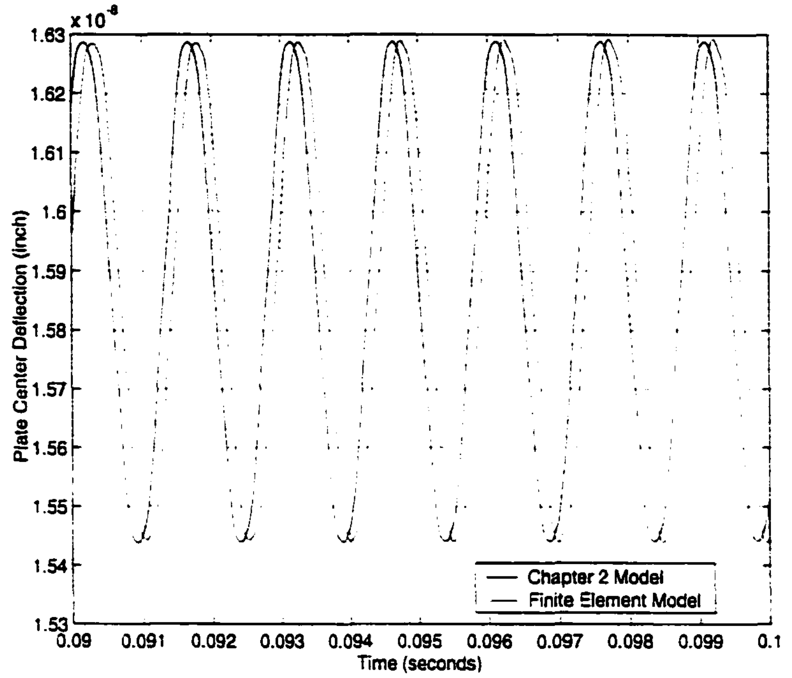

Figure 3.5: Comparison of the analytical and the finite element solutions: plate vertical deflection (in) per unit heat flux $\left(\frac{\text{Btu}}{\text{h ft}^2}\right)$ at the plate center for time 0.09 to 0.1 seconds.

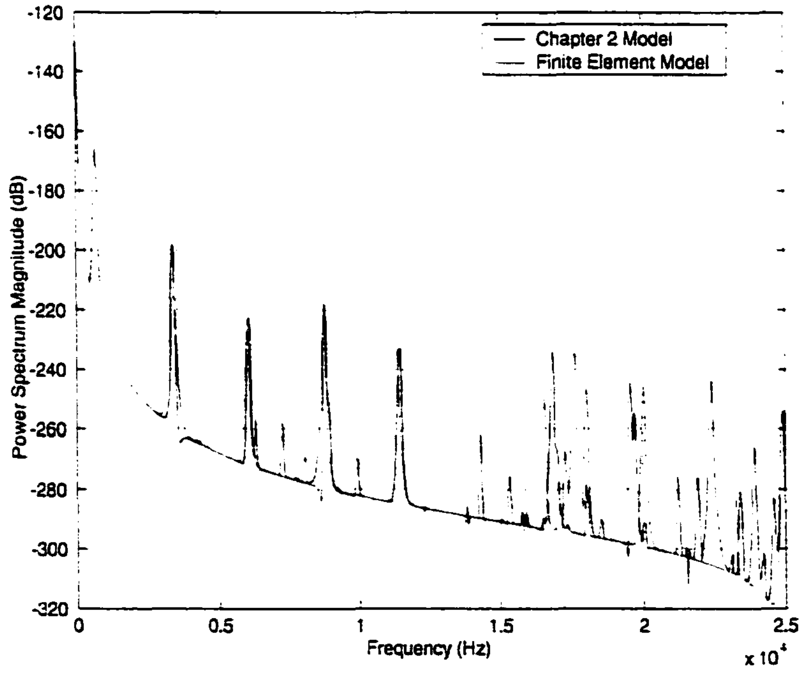

Figure 3.6: Comparison of the analytical and the finite element solutions: power spectral density of the responses shown in Figure 3.4.

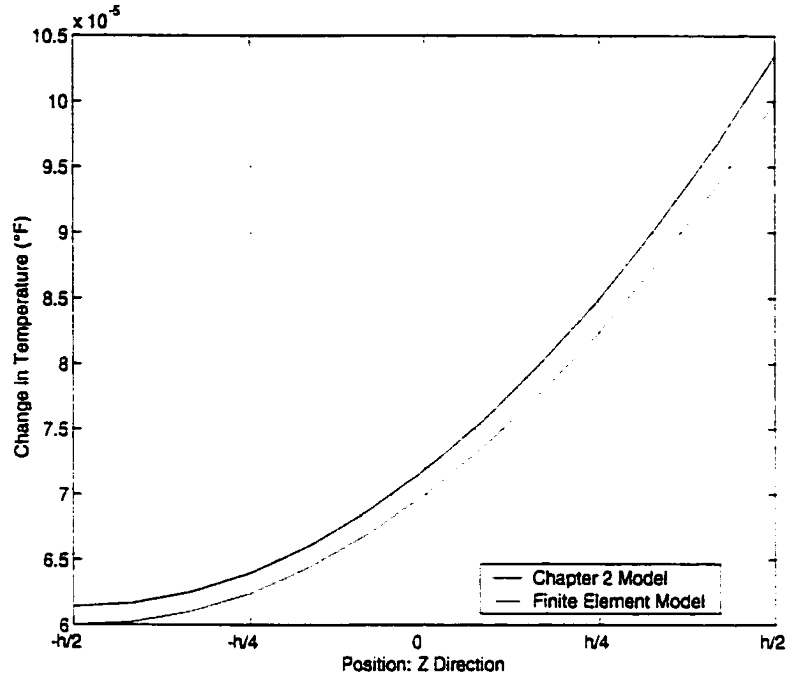

Figure 3.7: Comparison of the analytical and the finite element solutions: change in temperature (°F) per unit heat flux $\left(\frac{\mathrm{Btu}}{\mathrm{h\,ft^2}}\right)$ as a function of the plate vertical coordinate at the plate center for $t = 0.1$ seconds.

The results presented in Figures 3.4 through 3.7 corroborate the finite element model and the computer code for the coupled thermomechanical model. The validity of the model for the study of dynamic vibration control is presented in the next section.

3.3.2 Case Study 2: Clamped Graphite/Epoxy/PZT Smart Plate Subjected to a Mechanical Impulse

To validate the current model for the study of vibration control, a comparison is made with the work published by Chandrashekhara and Agarwal [24]. Their work did not include thermoelastic effects and for comparitive purposes it is ignored in this case study. They analyzed a clamped plate with collocated sensors and actuators as shown in Figure 3.8. The insulating layer required between the sensor and actuator was ignored in their analysis as it was in the current work. The plate was a four layer 0/90/90/0 graphite-epoxy laminate with the lamina mechanical properties listed in Table 3.1. The piezoceramic mechanical and piezoelectric properties are also listed in Table 3.1.

The plate dimensions were: $a = b = 0.254$ m, $h = 2.54 \times 10^{-3}$ m, and the piezoceramic sensor and actuator dimensions were 0.127 m long, 0.127 m wide and 2.0×10^{-4} m thick. The sensors and actuators were centered on the plate. Due to biaxial symmetry only a quarter of the plate was analyzed. The quarter plate was modeled by a 4×4 finite element mesh which resulted in 405×405 global mass and stiffness matrices. To obtain a good comparison with the work published in [24], a damping coefficient of $\zeta = 0.005$ (0.5%) on all mechanical vibration modes was assumed. Applying the mechanical essential boundary conditions, and forming the state-space model, yielded a system with 576 states. Due to the length of elapsed time since publication (1993), the data used to generate the figures in [24] were not available for easy comparison.

Table 3.1: Smart Plate Graphite/Epoxy and Piezoceramic Mechanical and Piezoelectric Properties

AS/3501-6 Graphite/Epoxy		**PZT G1195**	
E_1	144.23×10^9 Pa	E	63.0×10^9 Pa
E_2	9.65×10^9 Pa	ν	0.28
G_{12}, G_{13}	4.14×10^9 Pa	ρ	7600 $\frac{\mathrm{kg}}{\mathrm{m}^3}$
G_{23}	3.45×10^9 Pa	d_{31}, d_{32}	$-180 \cdot 10^{-12}$ $\frac{\mathrm{m}}{\mathrm{V}}$
ν_{12}	0.3		
ρ	1389.23 $\frac{\mathrm{kg}}{\mathrm{m}^3}$		

The plate was subjected to a uniformly distributed load over the entire surface of the plate for a duration of 1.6×10^{-3} seconds. The magnitude of the load was 2.5×10^4 N/m^2. This mechanical impulse was designed to excite the first mode of the plate. The transient response of the plate without the piezoceramic sensors and actuators, referred to as the original plate, is shown in Figure 3.9. The transient response of the plate with the piezoceramic sensors and actuators, referred to as the smart plate, is shown in Figure 3.10. The two responses are different because the mass and stiffness of the piezoceramic elements are included in the model of the smart plate. Both these responses compare very favorably with the results shown in Figure 5 of [24], which is expected as the mechanical portion of the finite element model developed in this chapter was based on the work by Chandrashekhara and Agarwal. Figure 3.11 illustrates the closed-loop response using negative rate feedback with a gain of 1000 Volts/Ampere (V / A). This response is damped considerably compared to the response shown in Figure 3.10. but is different than the response for a negative rate feedback gain of 1000 V / A shown in Figure 6 of [24]. The response compares much more favorably with the response for a negative rate feedback gain of 500 V / A shown in Figure 6 of [24]. Figure 3.12 illustrates the closed-loop response using positive position feedback with a gain of 4.0×10^6 Volts/Coulomb (V / C). This response differs only slightly from the response shown in Figure 3.10. and is considerably different from the response for a positive position feedback gain of 4.0×10^6 V / C shown in Figure 8 of [24]. According to Chandrashekhara and Agarwal. positive position feedback reduces the stiffness. which is expected. and increases damping. which is counter-intuitive. To test this hypothesis. the closed-loop response with a positive position feedback gain of 4.0×10^7 V / C was generated and is illustrated in Figure 3.13. This response displays considerably less plate stiffness than the response in Figure 3.10. but displays absolutely no damping characteristics. This indicates that there were errors in the material presented in [24]. Since positive position feedback reduces stiffness. negative position feedback increases stiffness. To insure that the current model displays this behavior. the closed-loop response with a negative position feedback gain of 4.0×10^7 V / C was generated and is illustrated in Figure 3.14. As expected. this response shows considerably more stiffness than the response shown in Figure 3.10.

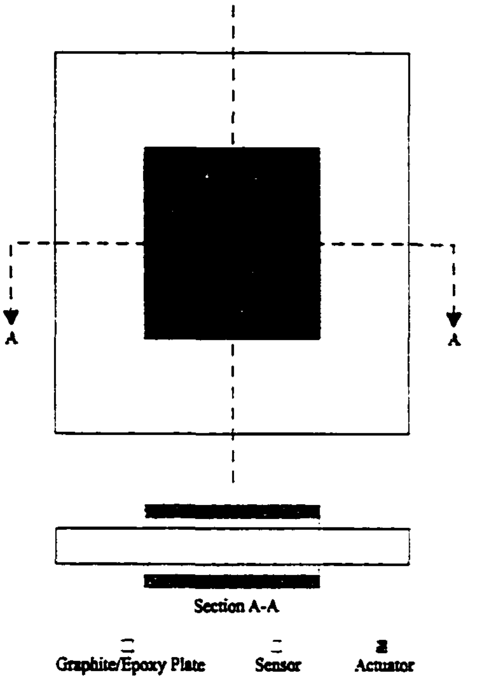

Figure 3.8: Graphite/Epoxy plate with collocated PZT sensors and actuators. PZT sensors and actuators are centered on the graphite/epoxy plate and cover $\frac{1}{4}$ of the plate.

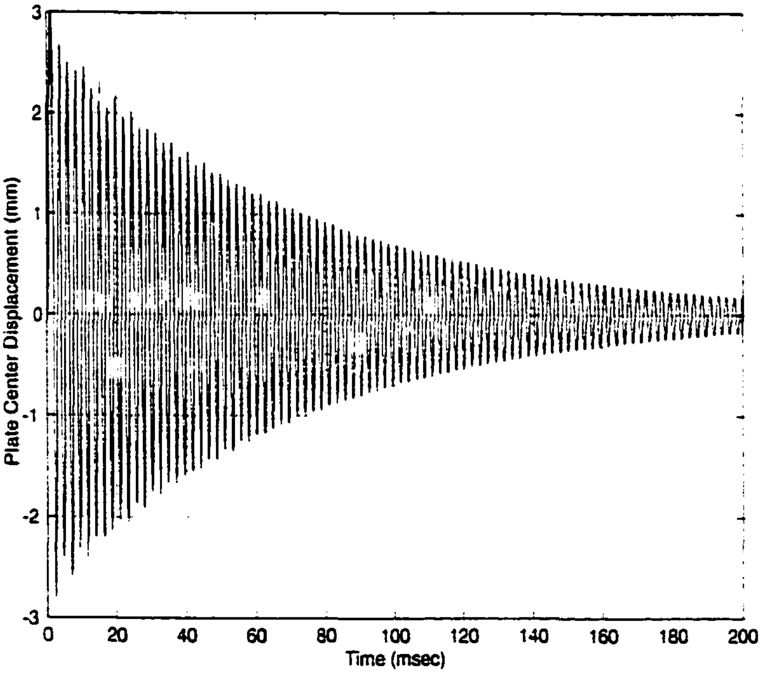

Figure 3.9: Original plate response.

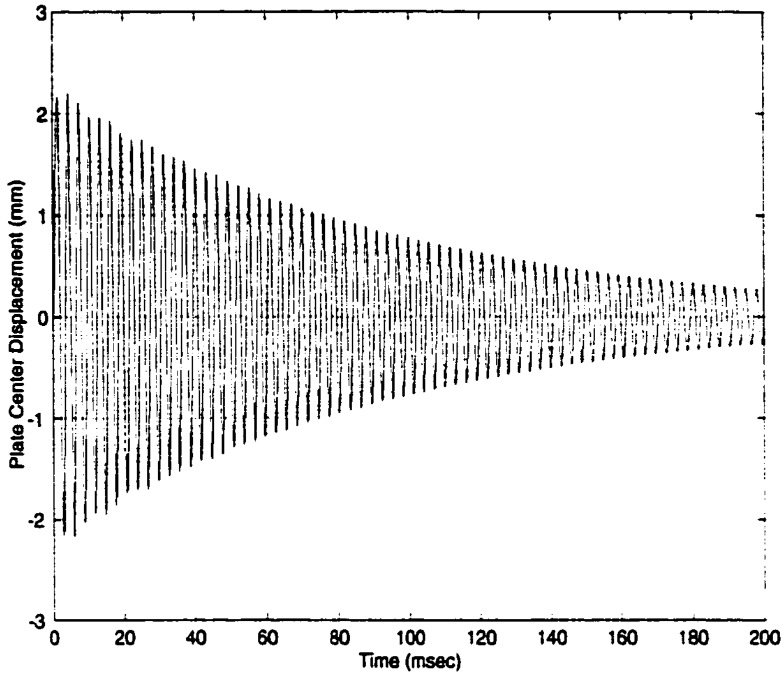

Figure 3.10: Smart plate open-loop response.

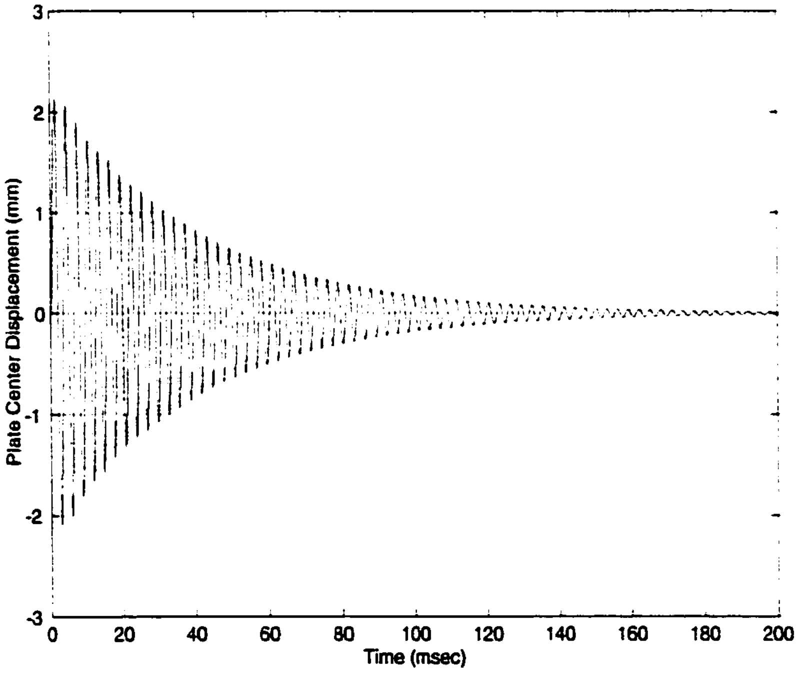

Figure 3.11: Smart plate closed-loop response using a negative rate feedback gain of 1000 V/A.

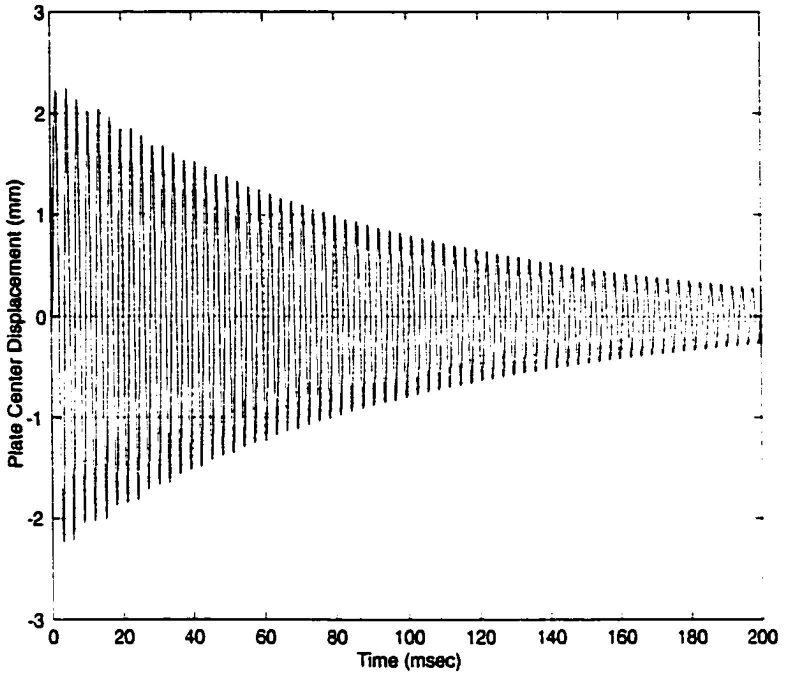

Figure 3.12: Smart plate response using a positive position feedback gain of 4.0×10^6 V/C.

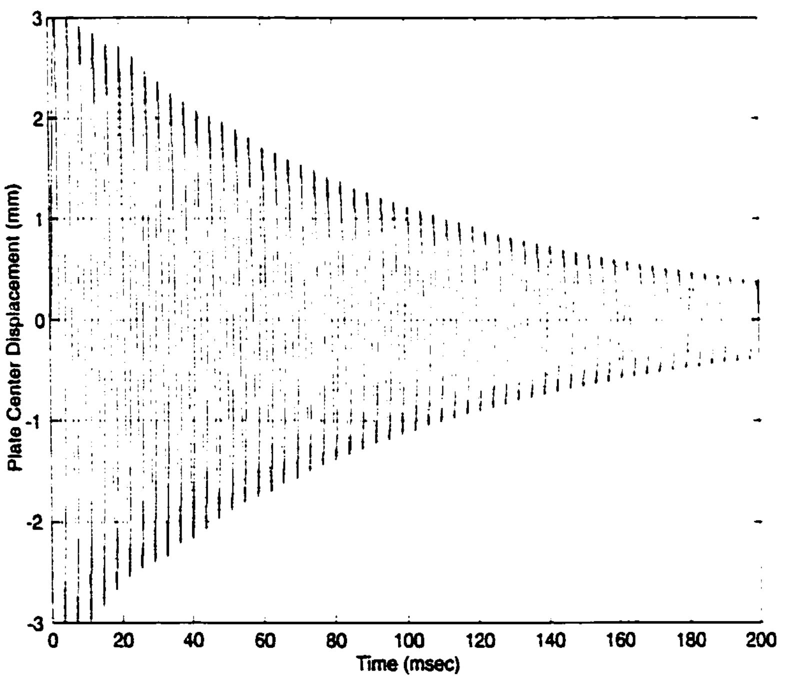

Figure 3.13: Smart plate response using a positive position feedback gain of 4.0×10^7 V/C.

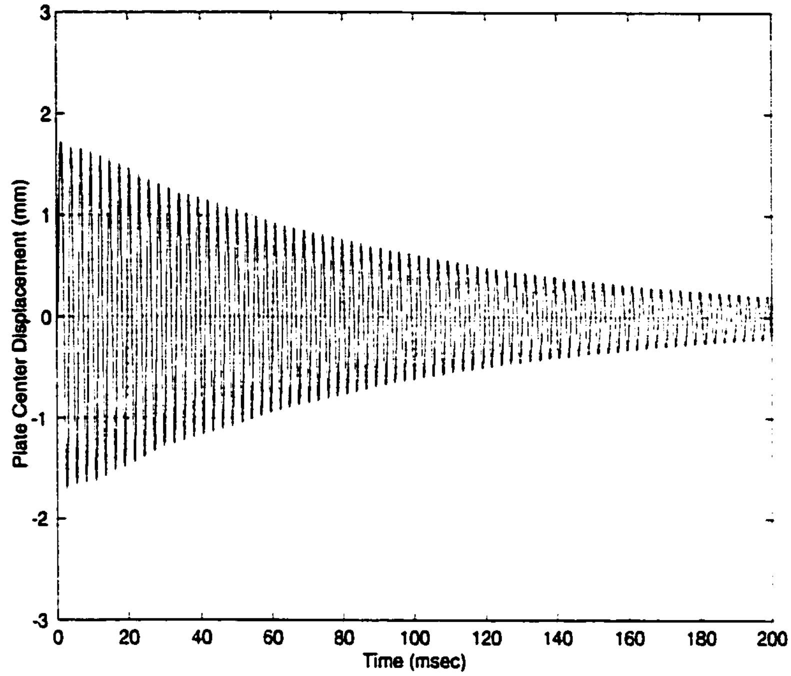

Figure 3.14: Smart plate response using a negative position feedback gain of 4.0×10^7 V/C.

Although there are discrepancies between the closed-loop responses predicted by the finite element model in this work and the work by Chandreshekhara and Agarwal, the model in this work displays the correct behavior to negative rate and negative position feedback and is suitable for closed-loop control studies.

3.4 Summary

A new finite element based method of solving coupled thermo-elastic plate problems has been developed. This method combines the accuracy and flexibility of solving the thermal portion of the plate problem using 3–dimensional finite elements with the computationally efficient method of solving the mechanical portion of the plate problem using 2–dimensional finite elements. This finite element model has several advantages compared to the model developed by [9] which assumed the thermal distribution is a cubic function of z:

1. More general thermal boundary conditions can be applied.

2. Internal heat sources are easily incorporated.

The main disadvantage is the large number of states required by this modeling technique. The model was extended to include piezoelectric elements suitable for closed loop vibration control of plates subjected to mechanical and thermal loads.

CHAPTER 4

CONTROLLER DESIGNS

4.1 Introduction

In Chapter 3, a finite element model of a "Smart Plate" was developed that was suitable for feedback control. Feedback is used in control systems to improve the dynamics of the system compared to the open loop dynamics, and to reduce the sensitivity of the system to disturbances and model uncertainty. This chapter presents an overview of some of the issues facing the control system designers and presents one general method for designing an optimal controller using classical control analysis techniques. Two design studies are presented to demonstrate this method.

4.2 Control Design Issues

Controls designers are usually faced with competing requirements, imposed on tracking (*steady-state error and lag*), disturbance rejection, and robustness to system uncertainty. Other issues facing the control system designer are:

1. The impact of anti-aliasing filters required to attenuate higher frequency modes before down-sampling in digital control systems. This issue has become more important over the last two decades. As a result of the dramatic improvement and cost effectiveness of digital technology combined with high order language software, more digital controllers are being used. This approach also allows more sophisticated controllers to be implemented.

2. The order of the system (*i.e., number of states*) and available outputs can dictate the applicable control design methodologies. LQG is often not feasible because it requires full-state feedback or a state-estimator must be employed. If there is a significant number of states requiring estimation, the resulting controller will be of significant order which may not be practical. Also, the estimator response must be faster than the plant response which may require large gains to achieve. Systems with large gains are usually sensitive to uncertainty which limits their use. The applicability of H_∞ optimal design methodology is also impacted

by the order of the system to be controlled. With this method. the order of the resulting controller is the order of the plant plus the order of the frequency domain weighting functions used to manipulate the design. Application of model reduction can reduce the order of the controller at the expense of optimality.

3. A major issue with control design is nonlinearities in the plant. There are two major types of nonlinearites: functional and hard. Functional nonlinearity refers to the fact that the differential equations governing the dynamics of the plant are nonlinear but continuous and differentiable. An example of functional nonlinearity is the six-degree-of-freedom equations describing the motion of a rigid body. A typical approach to handle functional nonlinearities is to design multiple linear controllers about a collection of trim conditions or operating points. then interpolate the gains and filters as the system dynamics move between these operating points. Recent advances in nonlinear control. such as feedback linearization and dynamic inversion. have focused on this type of nonlinearity. Hard nonlinearity refers to effects that are not continuously differentiable. Examples of hard nonlinearity are: actuator saturation. signal limiting. backlash. and stiction. Care must be exercised when designing a dynamic controller (*a control system with states or integrators*) that controls a system with actuator saturation and/or signal limiting. To avoid lags due to integrator wind-up in the controller when the plant has saturated or limited a signal. the integrators in the plant should be reset to be consistent with the saturated/limited signal.

In the current work. item number 2 is the most relevant due to the order of the plate model. However. piezoelectric actuators are subject to damage if the negative applied electric field is too large [49]. To avoid this problem. a voltage limiter is placed in the controller to prevent the applied negative voltage from exceeding the following limit

$$V_{\min} = E_{\min} \times h_p \tag{4.1}$$

where $E_{\min}$ is the negative applied electric field limit. and h_p is the piezoelectric actuator thickness. Since only constant gain feedback controllers are designed in this work. this nonlinearity does not introduce integrator wind-up issues, but does limit performance.

4.3 Optimal Classical Controller

Classical control theory was developed for single-input single-output (SISO) sytems. Typical time domain performance measures are rise time, settling time, steady-state error, overshoot with respect to step inputs, and input signal tracking of arbitrary inputs. Typical frequency domain robustness measures include gain margins, phase margins, and structural mode peak gain attenuation. Two common design methods are the Root Locus Method and open-loop frequency-domain loop shaping using lead-lag controller designs. These design methods usually require manually iterating the controller design and checking it against the performance and robustness requirements. The proposed design method automates this process through the use of an optimization routine.

4.3.1 Optimal Classical Controller Design Methodology

This section describes a controller design mehodology for designing optimal controllers using classical control performance and robustness metrics. This method is outlined in the following four steps.

1. Determine the controller structure and the design parameters to optimize. Typical design parameters are the control gains and the compensation filter parameters.

2. Choose the design metric to optimize. Ideally this metric should relate directly to the performance requirements imposed on the system. For example, a hard disk read/write head is positioned using step responses, so the the systems step response should be optimized. A metric to optimize the step response is

$$\min \int_{t_o}^{t_f} |e(t)|\, dt \tag{4.2}$$

where $e(t)$ is the error between the command and the measured response. This metric penalizes all errors evenly. A better metric to optimize step responses is

$$\min \int_{t_o}^{t_f} t\, |e(t)|\, dt \tag{4.3}$$

This metric time weights the errors so initial errors have less penalty, and steady-state errors have more penalty. This metric is also well suited to step response optimization of non-minimum phase systems which exhibit wrong way effects.

3. Determine the design constraints. These design constraints should follow from the requirements imposed on the system. Typical time domain constraints are rise time (sometimes referred to as the time constant), settling time, percent overshoot, and steady-state error. For non-minimum phase systems, the magnitude of the wrong way effect (undershoot) may also be constrained. Typical frequency domain constraints are gain and phase margins, bandwidth, and peak gain attenuation. Note that it is possible to include modern control robustness measures such as the Sandberg-Zames Small Gain Theorem [50], the sensitivity and complementary sensitivity function peak gain [51], the multivariable gain and phase margins developed by Bar-on and Jonckheere [52] [53], or Doyle's structured singular value [54], μ, as constraints on the design.

4. Use a constrained optimization algorithm to iterate the design parameters to get an optimal control design. There are several classes of optimizers currently available. Two popular classes of optimization algorithms are gradient based algorithms and genetic algorithms. Gradient based optimization algorithms require an initial guess of the solution. If the solution set is tightly constrained, it may be hard to find an initial guess that satisfies the constraints, and the gradient based algorithm may not be able to find a solution that satisfies the constraints, let alone find an optimal solution. Also, gradient based optimizers are subject to getting stuck in locally optimal solutions instead of finding the globally optimal solution. However, if the locally optimal solution satisfies all of the design requirements it is still valid, although not optimal. See Luenberger [55] for a general treatment of gradient based optimization algorithms. Genetic algorithm based optimizers do not require an initial guess to start, but require the range of the design parameters to be specified. Genetic algorithms are not prone to getting stuck in locally optimal solutions as are gradient based algorithms. However, if the solution set is tightly constrained, genetic algorithm based optimizers will test many solutions that do not

satisfy the constraints. If each design can be evaluated quickly (*i.e.*, on the order of a design per second), then a genetic algorithm will probably yield satisfactory results. See Goldberg [56] for a general treatment of genetic algorithms applied to search, optimization, and machine learning.

The following section presents two design studies that use the controller design methodology outlined above to design constant gain feedback controllers for two different "Smart Plate" applications.

4.4 Design Studies

In this section, two design studies are presented to illustrate the design process outlined in Section 4.3.2. The first design study was concerned with designing a set of feedback gains for a clamped graphite/epoxy/PZT smart plate subjected to a mechanical impulse. This study compared feedback gains designed without consideration of the magnitude of the electric field applied to the piezoelectric actuators, to two designs that limited the magnitude of the electric field applied to the actuators. The second design study was concerned with designing a set of feedback gains to control thermoelastic vibrations induced in a simply supported graphite/epoxy/PZT smart plate by a thermal impact.

4.4.1 Design Study 1: Clamped Graphite/Epoxy/PZT Smart Plate Subjected to a Mechanical Impulse

This design study was concerned with designing a set of feedback gains to minimize the vibration response of a clamped graphite/epoxy/PZT smart plate subjected to a mechanical impulse. The graphite/epoxy/PZT smart plate and mechanical impulse used in this study were described in Section 3.3.2. See Figure 3.10 for the open loop impulse response of the smart plate. Three different designs were compared. Design 1 usee a linear controller with two different fixed gains: a charge, or position, feedback gain, K_p, and an amperage, or rate, feedback gain, K_r. Due to the plate symmetry the gains for the top and bottom piezoelectric sensor/actuator pair were the same. The response to be minimized was

$$J = \min_{K_r\ K_p} \int_0^{0.05} |w(t)|\, dt \tag{4.4}$$

where $w(t)$ is the plate center displacement. A classical SISO frequency domain constraint, the closest point of approach of the Nyquist plot to the critical point, -1, was used to insure robustness of the design to model uncertainty. This design parameter, a_0, was required to be ≥ 0.6. Figure 4.1 illustrates the linear Simulink [57] model used to simulate the time domain response of the closed loop system. Figure 4.2 illustrates the linear SISO model used for robustness analysis. Due to symmetry, only the robustness of the top sensor/actuator feedback loop was checked. Note that robustness was checked with the bottom sensor/actuator feedback loop closed. This is an example of one-loop at a time robustness analysis, which is the only method possible with classical SISO control theory.

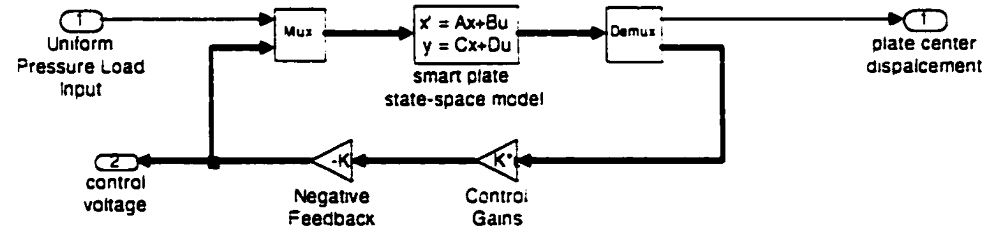

Figure 4.1: Linear Simulink model used to simulate design 1 closed loop response. The thick lines represent vector signals.

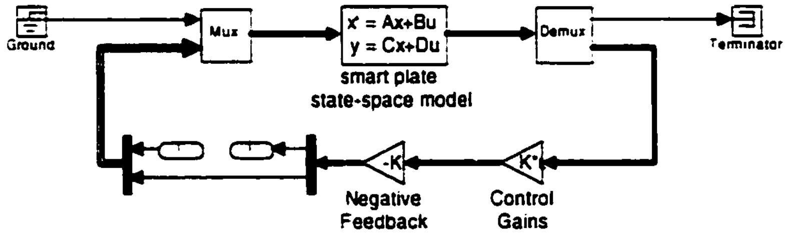

Figure 4.2: Linear Simulink model used to check robustness of designs 1, 2, and 3.

This design did not limit the electric field strength applied to the actuators. Since PZT can be depolarized by a strong electric field with polarity opposite to the original poling voltage, this design can result in damage to the piezoelectric actuators. Designs 2 and 3 were the same as design 1 except they limited the negative electric field applied to the actuators to avoid damaging the actuators. Design 2 limited the negative electric field to $\geq -500\frac{V}{mm}$ and design 3 limited the negative electric field to $\geq -1000\frac{V}{mm}$, which were the lower and upper bounds recommended in the Morgan Matroc Piezoelectric Ceramic Data Book for Designers [49]. Figure 4.3 illustrates the non-linear Simulink model used to simulate the closed-loop time-domain response of designs 2 and 3. These designs also used the model shown in Figure 4.2 for robustness analysis.

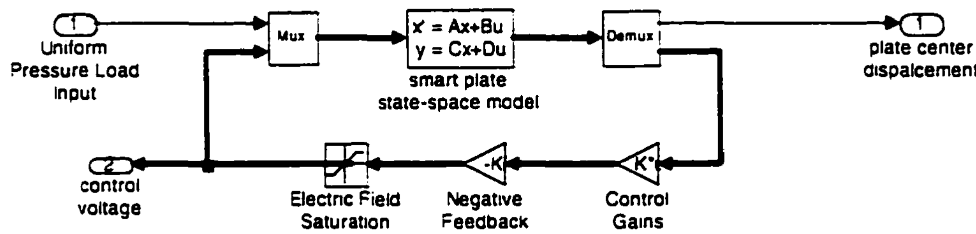

Figure 4.3: Non-linear Simulink model used to simulate designs 2 and 3 closed loop response. The thick lines represent vector signals.

All three designs minimized the cost, J, using Design Optimization Tools [58], or DOT, a gradient based FORTRAN optimizer that utilizes the Modified Feasible Direction Algorithm [59]. A MATLAB script was used to set up the optimization parameters to call a MATLAB MEX-File [60] version of DOT, and to simulate the appropriate Simulink model. The initial gains used to start the optimization process were $K_p = 4 \times 10^7 \, \frac{V}{C}$ and $K_r = 1 \times 10^4 \, \frac{V}{A}$, and the upper and lower bounds on the relative change in the gains were set to 1×10^{10} and 1×10^{-10}, respectively. Note that DOT requires that the constraints be normalized. For these designs, the normalized constraint was

$$g = 1 - \frac{a_0}{0.6} \tag{4.5}$$

Therefore, the constraint is satisfied for $g \leq 0$, *i.e.*, $a_0 \geq 0.6$. Table 4.1 compares the designs after optimization, and also lists the pertinent performance metrics of the open loop response. This table contains values for the feedback gains, K_p and K_r, the cost, J, the constraint, g, the maximum absolute center plate deflection, $\max|w(t)|$, and the maximum and minimum applied electric fields.

Table 4.1: Design Study 1 Results

Design	K_p $\frac{V}{C}$	K_r $\frac{V}{A}$	J mm · ms	g NA	max $\lvert w(t)\rvert$ mm	max E $\frac{V}{mm}$	min E $\frac{V}{mm}$
Open-Loop	NA	NA	55.03	NA	2.20	NA	NA
1	4×10^{-3}	1.17×10^5	2.13	$-\frac{2}{3}$	1.17	8.6×10^3	-8.6×10^3
2	4×10^{-3}	1.88×10^5	2.58	$-\frac{2}{3}$	1.32	1.58×10^4	-5×10^2
3	4×10^{-3}	1.72×10^5	2.59	$-\frac{2}{3}$	1.33	1.51×10^4	-1×10^3

E. Notice that for all three designs the optimized value for K_p was limited by the lower bound on the relative change in gain. This was a result of optimizing the plate's impulse response. The applied pressure impulse excited vibrations but produced near zero average deflection. In this case, rate feedback was more effective at minimizing J than was position feedback. If the system was optimized with respect to an input that yielded a non-zero average deflection, say a step response, the stiffness added by the position feedback gain would help minimize J. As expected, design 1 yielded the lowest cost, K_r gain, and maximum plate deflection, but exceeded the recommended negative electric field limit by 800%. Designs 2 and 3 had similar cost, maximum deflection, and maximum positive applied electric fields, but design 2 had a 9.4% larger K_r. This larger gain helped to offset the additional limiting imposed on the applied negative electric field. Figures 4.4 through 4.8 graphically compare the three designs. Figure 4.4 shows the closed loop response of the center plate deflection for all three initial designs. Figure 4.5 shows the closed loop response of the center plate deflection for all three optimal designs. As noted above, this figure demonstrates that design 1 had the best response and designs 2 and 3 were indistinguishable. Comparison of Figures 4.4 and 4.5 illustrates that the optimized design performed significantly better than the initial designs. Figures 4.6 and 4.7 show the applied electric field for the top and bottom actuators, respectively. These figures illustrate that design 1 drastically exceeded the recommended negative electric field, and would be unsuitable in any long-term application. Figure 4.8 compares the Power Spectral Density (PSD) of the three responses illustrated in Figure 4.4. This figure shows that the nonlinear feedback controller excited the natural vibration modes more that the linear feedback controller, especially the second mode. This was the primary reason that designs 2 and 3 had 20% greater cost compared to design 1. Lastly note that all three designs were not affected by the frequency domain constraint. Therefore, the optimal K_r gains were affected only by the cost. In this case, a larger K_r only served to excite the vibrations which increased the cost. This is shown in Figure 4.9 which compares the plate center displacement for the optimal design 1 gains, and a design with gains twice as large. Figure 4.10 compares the PSD of the two responses illustrated in Figure 4.9. This figure shows that increasing the gains from optimal increased the first and second vibration modes.

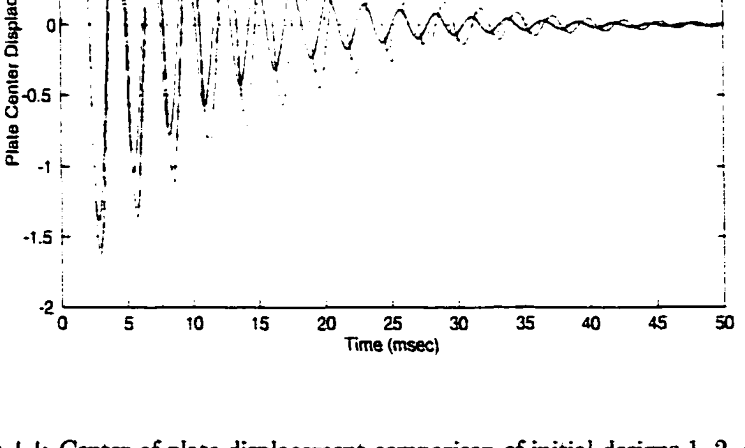

Figure 4.4: Center of plate displacement comparison of initial designs 1, 2, and 3.

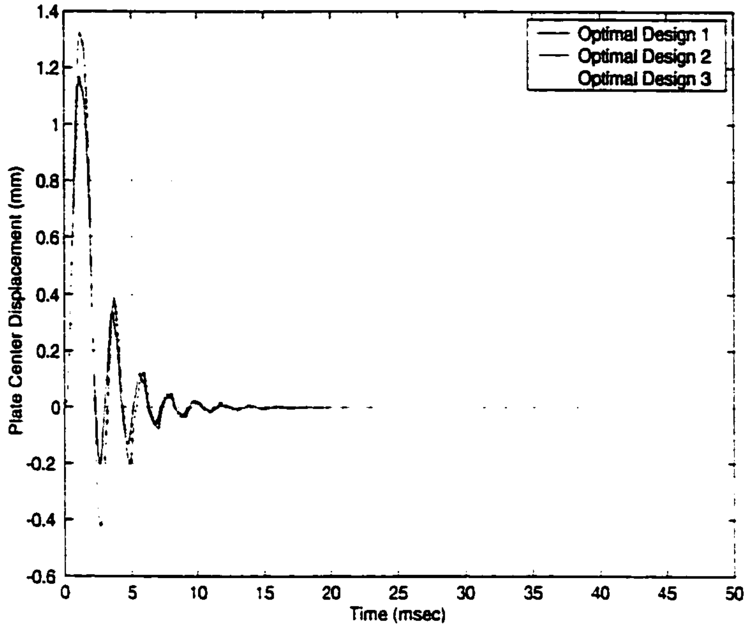

Figure 4.5: Center of plate displacement comparison of optimal designs 1, 2, and 3.

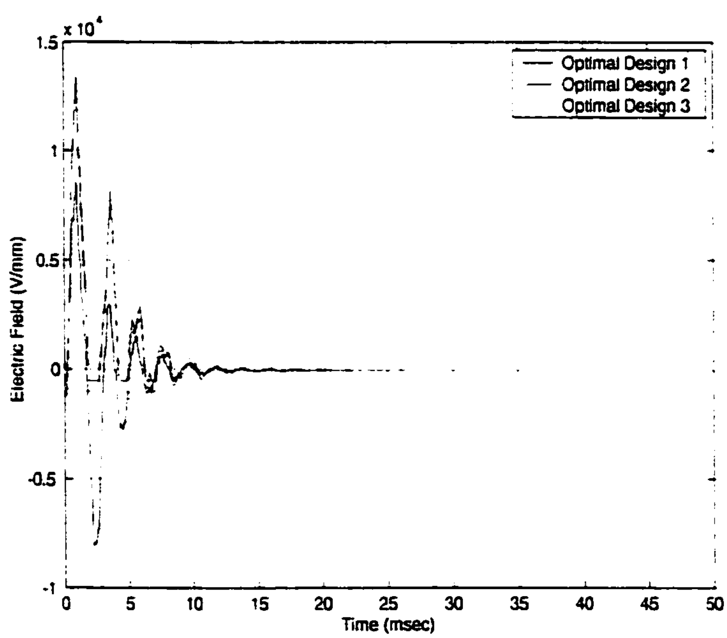

Figure 4.6: Top actuator applied electric field comparison of optimal designs 1, 2, and 3.

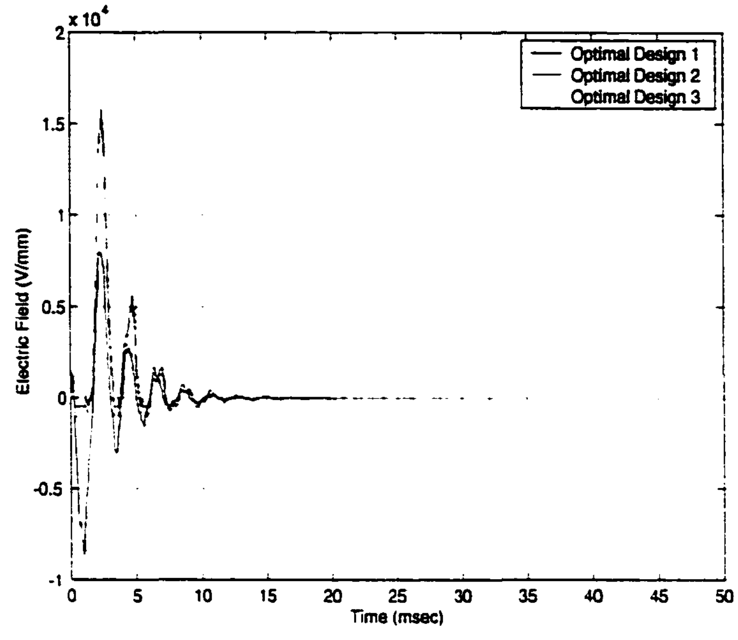

Figure 4.7: Bottom actuator applied electric field comparison of optimal designs 1. 2. and 3.

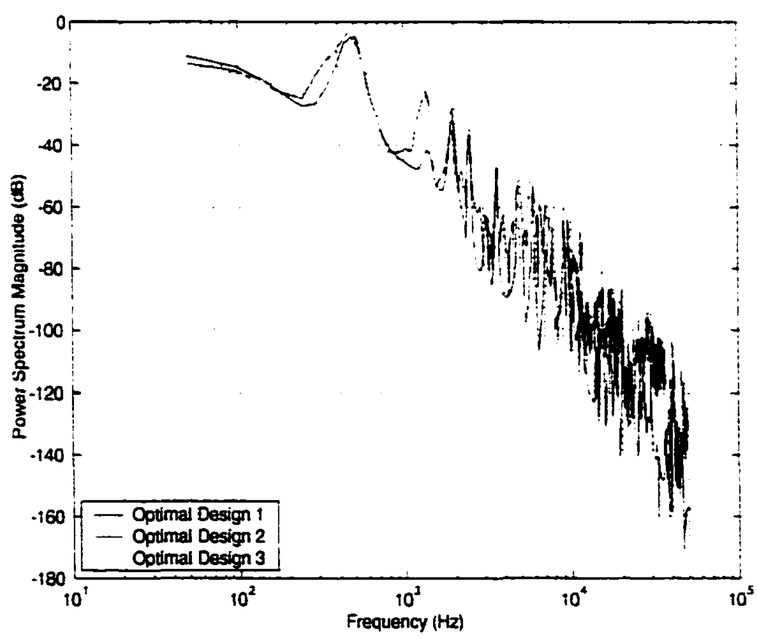

Figure 4.8: Power Spectral Density comparison of the center of plate deflection of optimal designs 1, 2, and 3.

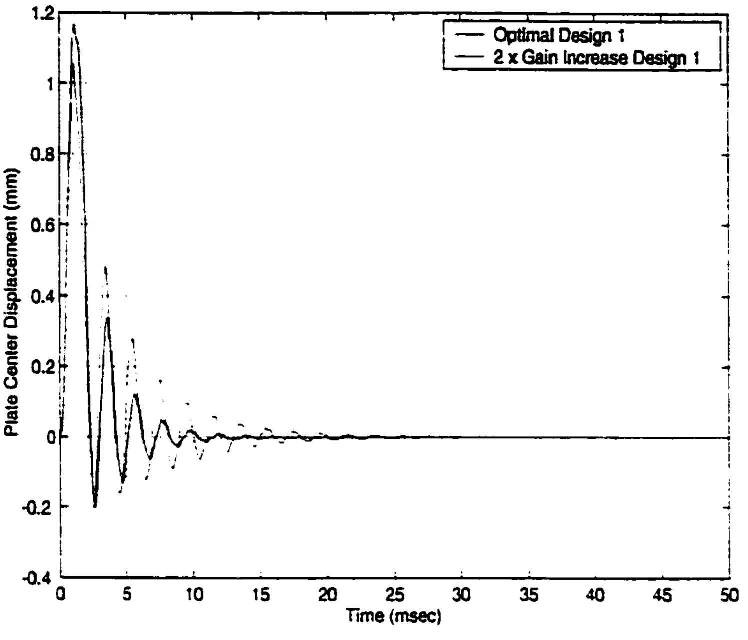

Figure 4.9: Effect of a factor of 2 gain increase from optimal on center of plate displacement (design 1).

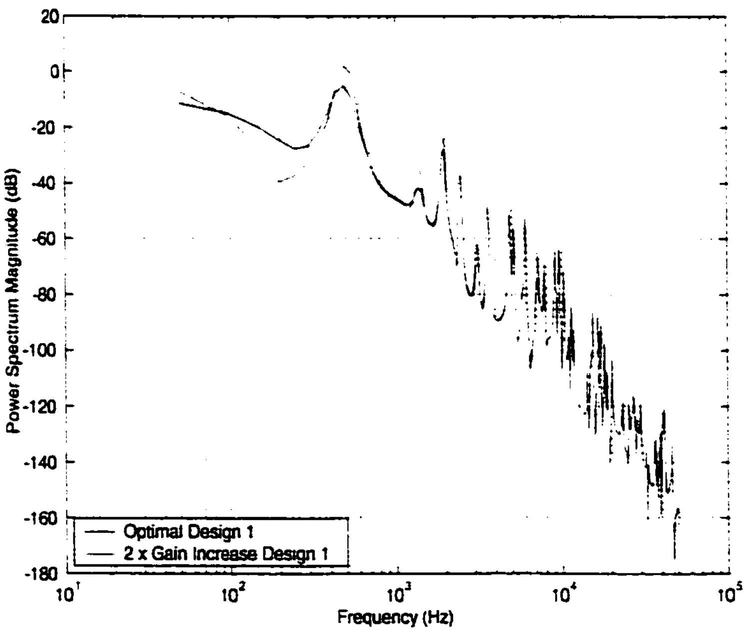

Figure 4.10: Effect of a factor of 2 gain increase from optimal on Power Spectral Density (design 1).

4.4.2 Design Study 2: Simply-Supported Graphite/Epoxy/PZT Smart Plate Subjected to a Thermal Shock

This design study was concerned with designing a set of feedback gains to minimize the impulse response of a simply supported graphite/epoxy/PZT smart plate subjected to a thermal impulse on its top surface. The bottom of the plate was insulated and the temperature at the boundary of the plate was constant. The plate was initially at rest and at the same temperature as the boundary. Figure 4.11 illustrates that the sensors and actuators were collocated. The insulating layer required between the sensor and actuator was ignored in this analysis. The plate was a four-layer 0/90/90/0 graphite-epoxy laminate with the lamina mechanical properties listed in Table 4.2. The piezoceramic mechanical and piezoelectric properties are also listed in Table 3.1. Note that the pyroelectric constant is negative and is relatively large which will result in significant coupling between the displacement, thermal and electric fields. The plate dimensions were: $a = b = 6.0$ inches, $h = 0.125$ inches, the piezoceramic sensors and actuators fully covered the plate, and each piezoceramic element was 0.015625 inches thick.

Table 4.2: Mechanical and Thermal Properties of a Graphite-Epoxy Lamina

Mechanical		Thermal	
Elastic Moduli		Conductivities	
E_{11}	$19.72 \times 10^6 \frac{\text{lb}}{\text{in}^2}$	k_{11}	$30.5 \frac{\text{Btu}}{\text{h ft} \cdot ^\circ\text{F}}$
E_{22}, E_{33}	$1.236 \times 10^6 \frac{\text{lb}}{\text{in}^2}$	k_{22}, k_{33}	$0.392 \frac{\text{Btu}}{\text{h ft} \cdot ^\circ\text{F}}$
G_{12}	$0.641 \times 10^6 \frac{\text{lb}}{\text{in}^2}$		
Poisson's Ratios		Expansion Coefficients	
ν_{12}	0.278	α_{11}	$-1.028 \times 10^{-8} \frac{\text{in}}{\text{in} ^\circ\text{F}}$
ν_{21}	0.017	α_{22}, α_{33}	$2.097 \times 10^{-5} \frac{\text{in}}{\text{in} ^\circ\text{F}}$
Density		Specific Heat	
ρ	$1.763 \times 10^{-3} \frac{\text{slug}}{\text{in}^3}$	C_v	$6.917 \frac{\text{Btu}}{\text{slug} ^\circ\text{F}}$

Table 4.3: Mechanical, Thermal, Piezoelectric, and Pyroelectric Properties of PZT

Mechanical		**Thermal**	
Elastic Moduli		Conductivities	
E	$9.137 \times 10^6 \frac{\text{lb}}{\text{in}^2}$	k_{11}, k_{22}	$1.213 \frac{\text{Btu}}{\text{h ft} ^\circ\text{F}}$
G	$3.568 \times 10^6 \frac{\text{lb}}{\text{in}^2}$		
Poisson's Ratios		Expansion Coefficients	
ν	0.28	α_{11}, α_{22}	$5.00 \times 10^{-7} \frac{\text{in}}{\text{in} ^\circ\text{F}}$
Density		Specific Heat	
ρ	$8.534 \times 10^{-3} \frac{\text{slug}}{\text{in}^3}$	C_v	$3.228 \frac{\text{Btu}}{\text{slug} ^\circ\text{F}}$
Piezoelectric Constant		Pyroelectric Constant	
d_{31}, d_{32}	$9.843 \times 10^{-9} \frac{\text{in}}{\text{V}}$	p_3	$-7.168 \times 10^{-8} \frac{\text{C}}{\text{in} ^\circ\text{F}}$

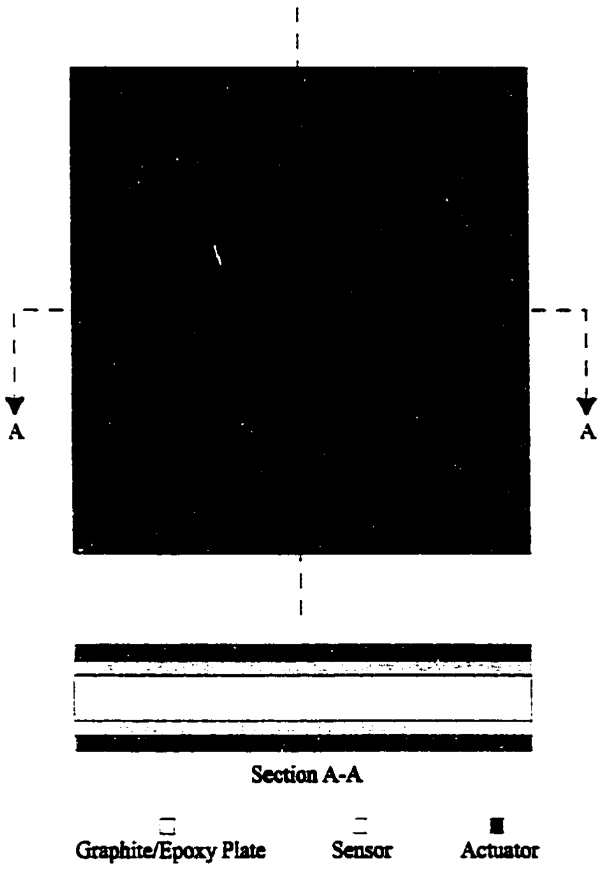

Figure 4.11: Graphite/Epoxy plate with collocated PZT sensors and actuators. PZT sensors and actuators fully cover the plate.

Because of biaxial symmetry, only a quarter of the plate was analyzed. The quarter plate was modeled by a $4 \times 4 \times 12$ mesh (x, y, and z directions, respectively), resulting in 405×405 global mechanical mass and stiffness matrices, 1053×1053 global thermal mass and stiffness matrices, and thermo-mechanical coupling matrices of consistent dimensional size. Mechanical damping with $\zeta = 0.001$ (0.1%) was added to all the mechanical vibration modes using Equation (3.227). This model had 1504 states, 5 inputs, and 9 outputs. The five inputs were:

1. Top of plate uniform heat flux, Btu / s / in^2.
2. Top piezoelectric actuator voltage, V.
3. Bottom piezoelectric actuator voltage, V.
4. Top piezoelectric actuator voltage rate, V / s.
5. Bottom piezoelectric actuator voltage rate, V / s.

The nine outputs were:

1. Center of plate vertical displacement, in.
2. Top piezoelectric sensor charge, C.
3. Top piezoelectric sensor current, A.
4. Top piezoelectric sensor current rate, A / s.
5. Bottom piezoelectric sensor charge, C.
6. Bottom piezoelectric sensor current, A.
7. Bottom piezoelectric sensor current rate, A / s.
8. Top center of plate temperature change, °F
9. Bottom center of plate temperature change, °F

The number of states in this model made it time consuming to simulate the response of the system to arbitrary inputs. To reduce the number of states in the model, Balanced Model Reduction, see Appendix A section A.4, was applied to this model. This yielded a system with 789 states, which required $\sim$ 72% less computation to simulate. To test the validity of the reduced model, a comparison of the plate response to a thermal impulse was performed. The models were subjected to a uniformly distributed thermal load over the top surface of the entire plate for a duration of 2.5×10^{-2} seconds. The magnitude of the pulse was -1×10^{3} $\frac{\text{Btu}}{\text{h ft}^2}$, (positive heat flux was out of the plate). Figures 4.12 through 4.20 show a comparison of the heat flux impulse response of the full state model and the reduced model. The only signals with significant error ($\sim$ 0.1%) was the bottom sensor charge and bottom center of plate temperature change. All other signals had insignificant errors. Figures 4.21 and 4.22 show a comparison of the singular values for both models. These comparisons indicate that the reduced state model accurately captured the significant dynamics of the full state model, and was suitable for controller design.

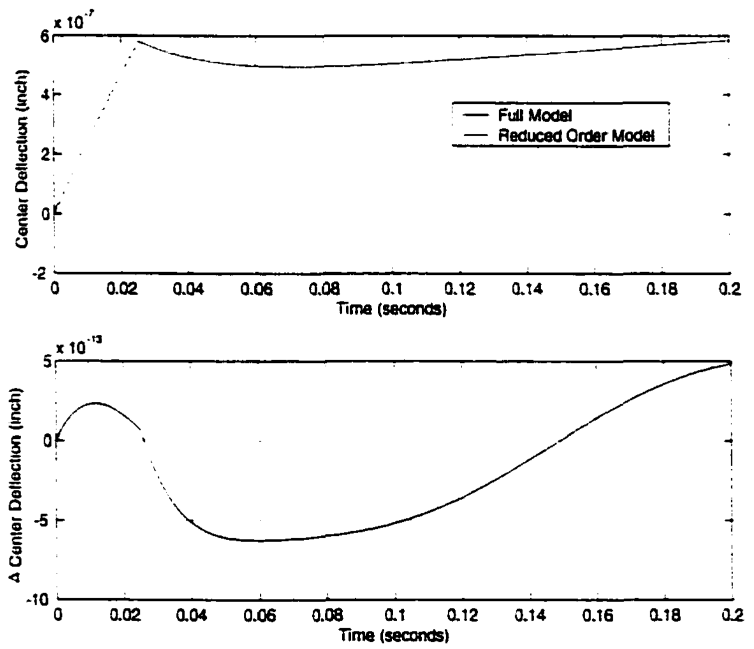

Figure 4.12: Top: Comparison of the full state model and the reduced state model plate center vertical displacement due to a heat flux impulse. Bottom: Difference between the full state model and the reduced state model plate center vertical displacement due to a heat flux impulse.

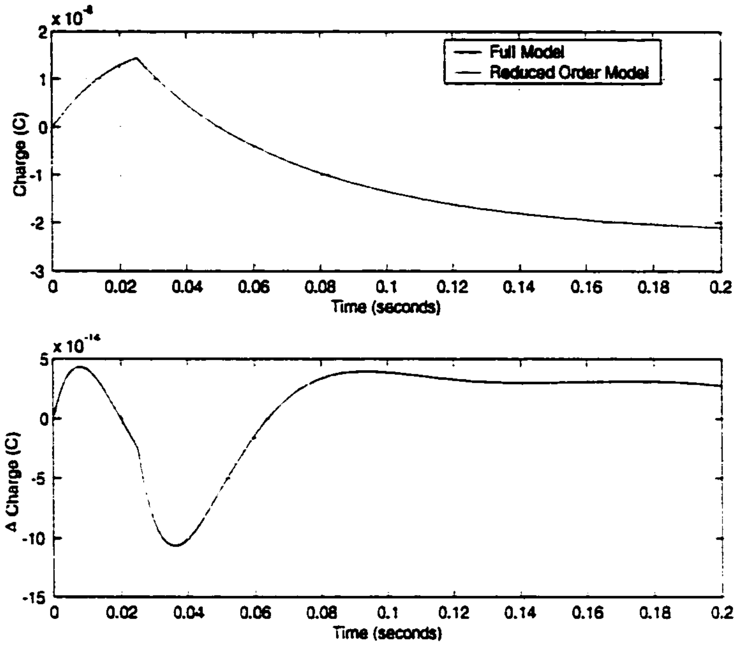

Figure 4.13: Top: Comparison of the full state model and the reduced state model top thermopiezoelectric sensor charge output due to a heat flux impulse. Bottom: Difference between the full state model and the reduced state model top thermopiezoelectric sensor charge output due to a heat flux impulse.

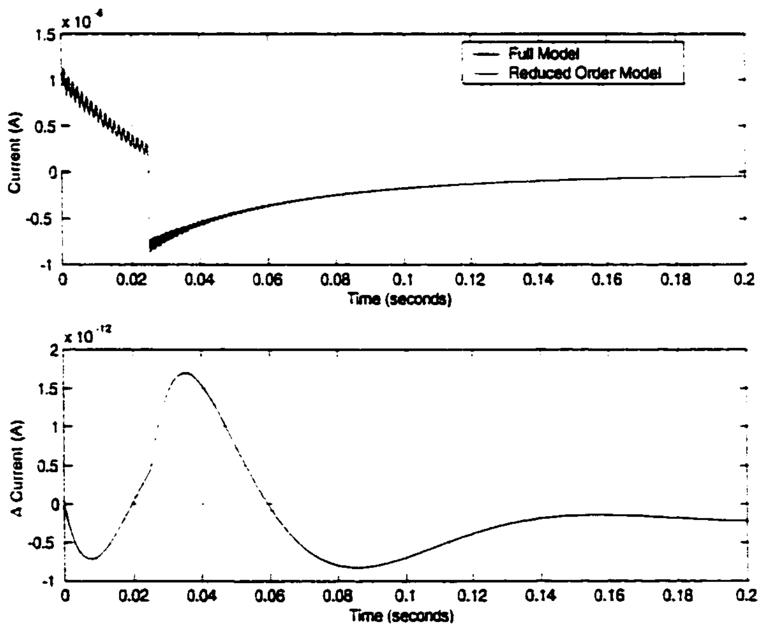

Figure 4.14: Top: Comparison of the full state model and the reduced state model top thermopiezoelectric sensor current output due to a heat flux impulse. Bottom: Difference between the full state model and the reduced state model top thermopiezoelectric sensor current output due to a heat flux impulse.

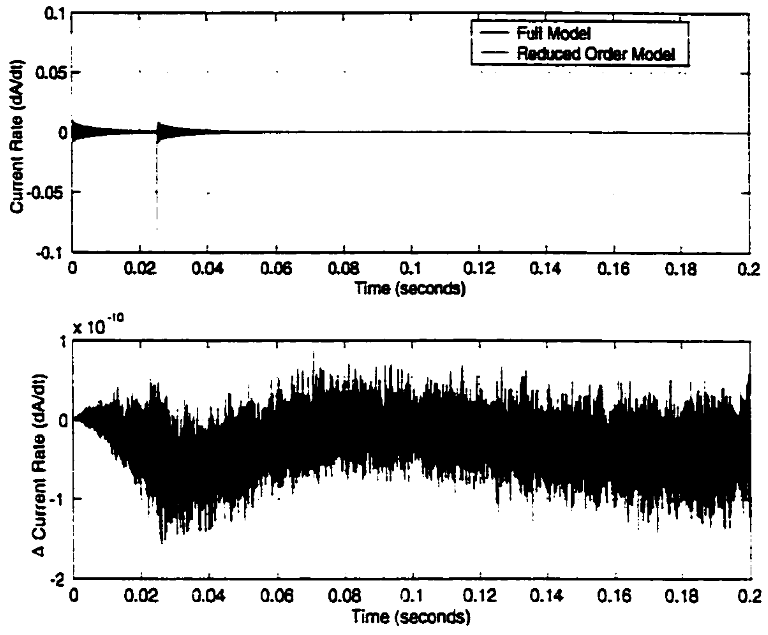

Figure 4.15: Top: Comparison of the full state model and the reduced state model top thermopiezoelectric sensor current rate output due to a heat flux impulse. Bottom: Difference between the full state model and the reduced state model top thermopiezoelectric sensor current rate output due to a heat flux impulse.

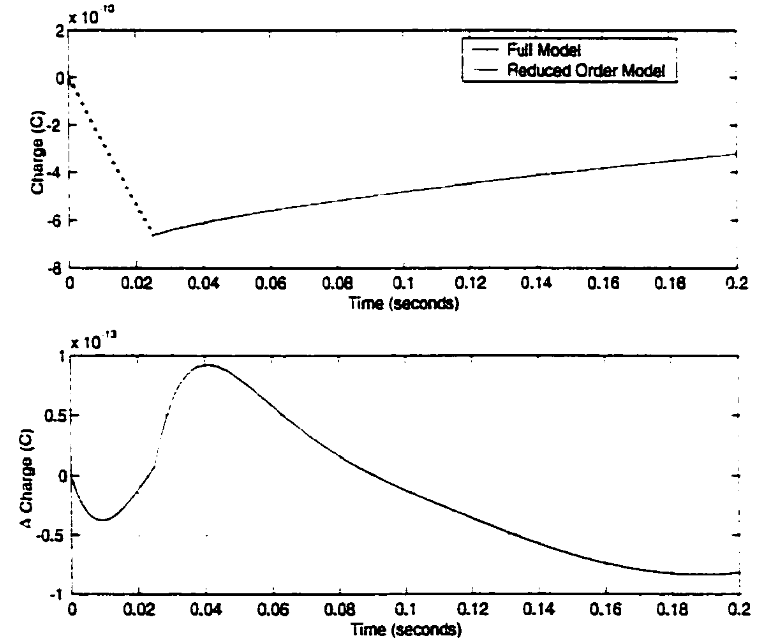

Figure 4.16: Top: Comparison of the full state model and the reduced state model bottom thermopiezoelectric sensor charge output due to a heat flux impulse. Bottom: Difference between the full state model and the reduced state model bottom thermopiezoelectric sensor charge output due to a heat flux impulse.

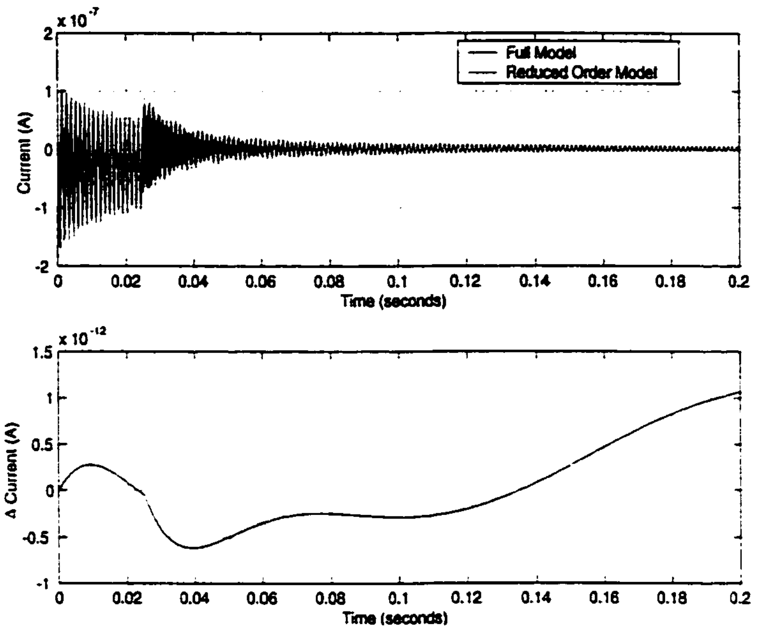

Figure 4.17: Top: Comparison of the full state model and the reduced state model bottom thermopiezoelectric sensor current output due to a heat flux impulse. Bottom: Difference between the full state model and the reduced state model bottom thermopiezoelectric sensor current output due to a heat flux impulse.

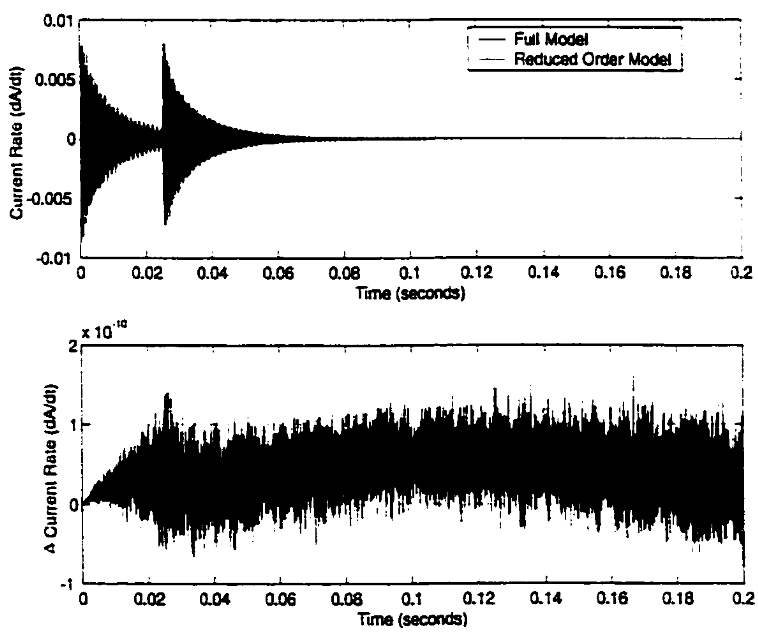

Figure 4.18: Top: Comparison of the full state model and the reduced state model bottom thermopiezoelectric sensor current rate output due to a heat flux impulse. Bottom: Difference between the full state model and the reduced state model bottom thermopiezoelectric sensor current rate output due to a heat flux impulse.

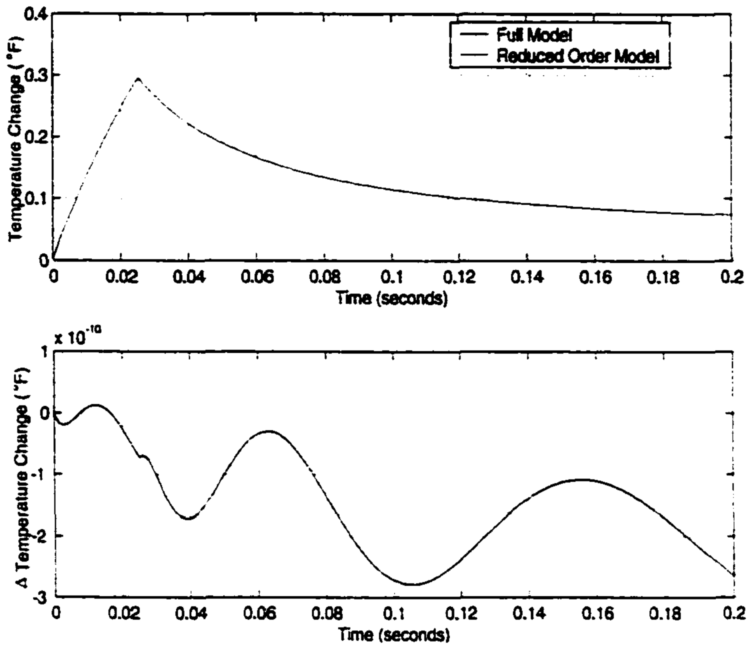

Figure 4.19: Top: Comparison of the full state model and the reduced state model plate top center temperature change due to a heat flux impulse. Bottom: Difference between the full state model and the reduced state model plate top center temperature change due to a heat flux impulse.

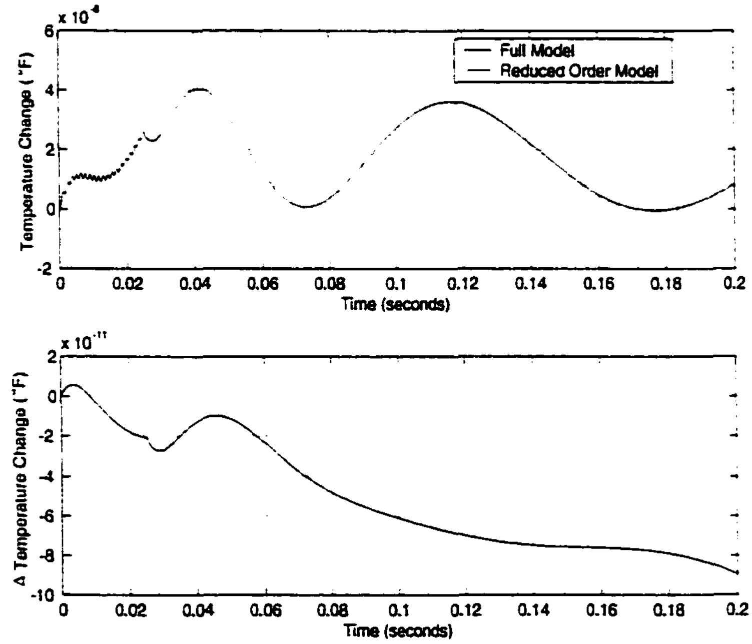

Figure 4.20: Top: Comparison of the full state model and the reduced state model plate bottom center temperature change due to a heat flux impulse. Bottom: Difference between the full state model and the reduced state model plate bottom center temperature change due to a heat flux impulse.

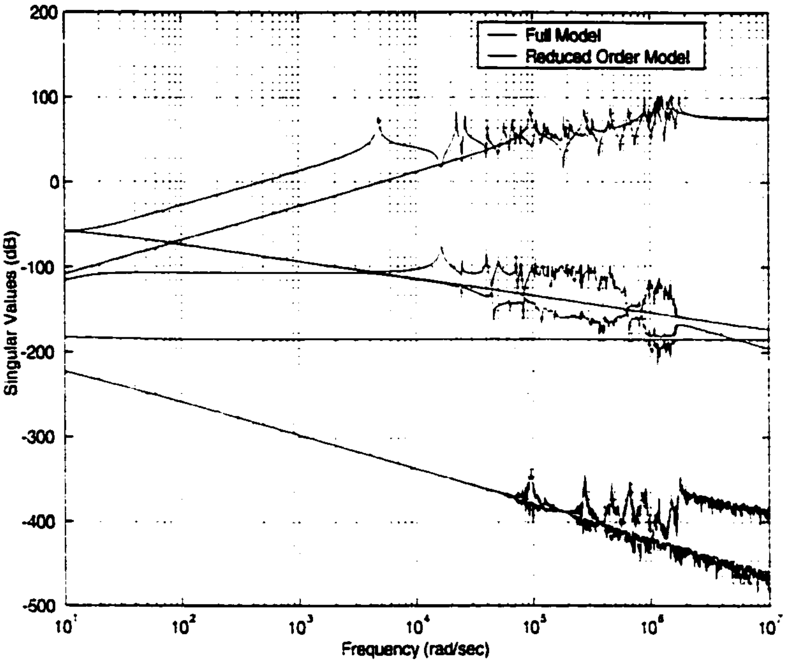

Figure 4.21: Comparison of the full state model and the reduced state model singular values.

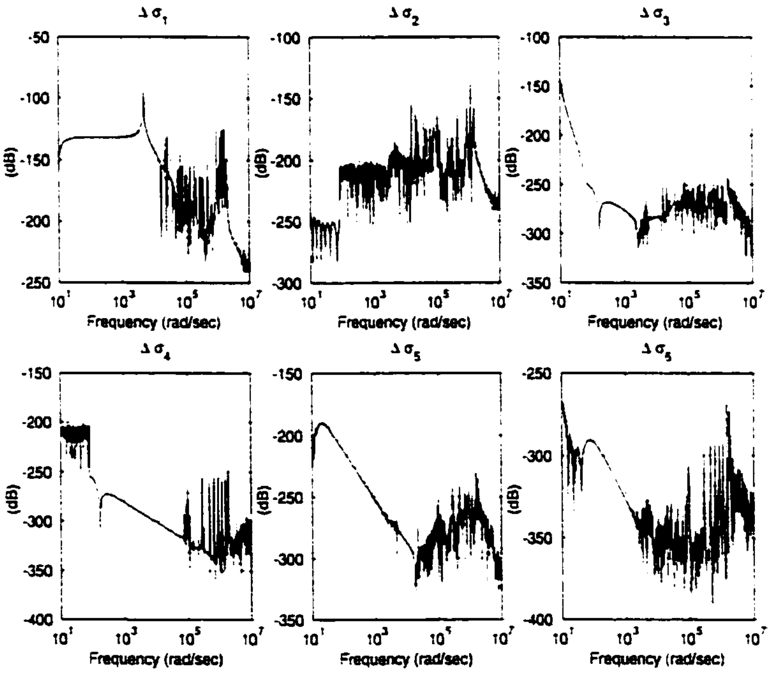

Figure 4.22: Difference between the full state model and the reduced state model singular values.

This design used a linear controller with four different fixed gains: top actuator charge, or position, feedback gain, K_{pt}, top actuator amperage, or rate, feedback gain, K_{rt}, bottom actuator charge, or position, feedback gain, K_{pb}, bottom actuator amperage, or rate, feedback gain, K_{rb}. A linear controller was acceptable in this case since the feedback voltages were small. Due to the polarization of the sensors and actuators this model used positive feedback. The response to be minimized was

$$J = \min_{K_{rt}\ K_{pt}\ K_{rb}\ K_{pb}} \int_0^{0.2} t\,|w(t)|\,dt \tag{4.6}$$

where $w(t)$ is the plate center displacement. The same SISO frequency domain constraint described in Section 4.4.1, Design Study 1, was applied to the control and voltage rate feedback loops of this design to insure a robust design. Figure 4.23 shows the linear SISO model used for robustness analysis. To use this robustness measure requires that only one loop be broken. For example, to check the robustness of loop one in Figure 4.23, close loops two through four and determine a_0. To check the robustness of loop two, close loops, one, three, and four and calculate a_0. Repeat this process to check the robustness of loops three and four. This process is referred to as successive loop closure. As in Design Study 1, DOT, MATLAB, and Simulink were used to solve the constrained optimization problem. The initial constant feedback gains used to start the optimization process were $K_{pt} = 4 \times 10^7\ \frac{\mathrm{V}}{\mathrm{C}}$, $K_{rt} = 1 \times 10^4\ \frac{\mathrm{V}}{\mathrm{A}}$, $K_{pb} = 4 \times 10^7\ \frac{\mathrm{V}}{\mathrm{C}}$, and $K_{rb} = 1 \times 10^4\ \frac{\mathrm{V}}{\mathrm{A}}$. The upper and lower bounds on the relative change in the gains were set to 1×10^{10} and -1×10^{10}, respectively. Figure 4.24 illustrates the linear Simulink model used to simulate the time domain response of the closed loop system. Note that both models incorporated free convective heat loss through the top surface of the plate, and used a convective heat transfer coefficient, h_c, of 5 $\frac{\mathrm{Btu}}{\mathrm{h\,ft^2\,{}^\circ F}}$ [61]. Assuming that the air surrounding the plate was at the plate inital temperature and that the temperature change was sinusoidally distributed, the heat loss over the top surface could be approximated using the top center of the plate temperature change as

$$\begin{aligned} q &= \frac{h_c \Theta_c}{ab} \int_0^b \int_0^a \sin\left(\frac{\pi x}{a}\right) \sin\left(\frac{\pi y}{b}\right) dx dy \\ &= \frac{4 h_c \Theta_c}{\pi^2} \end{aligned} \tag{4.7}$$

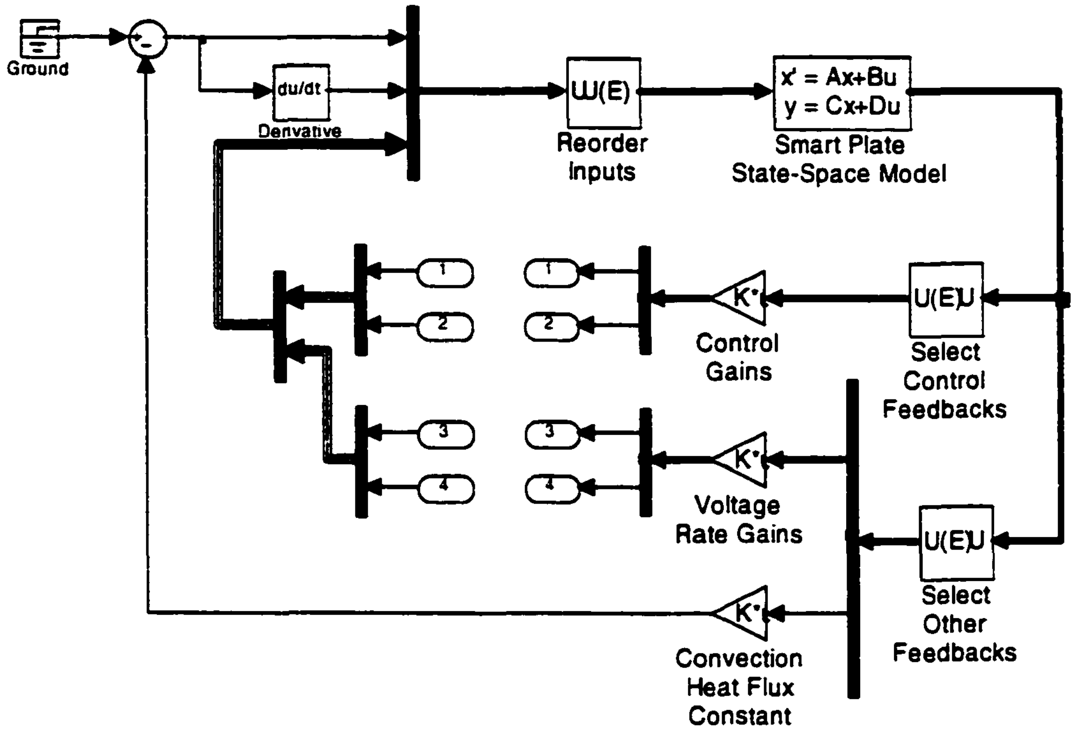

Figure 4.23: Linear Simulink model used to check robustness of design. The thick lines represent vector signals.

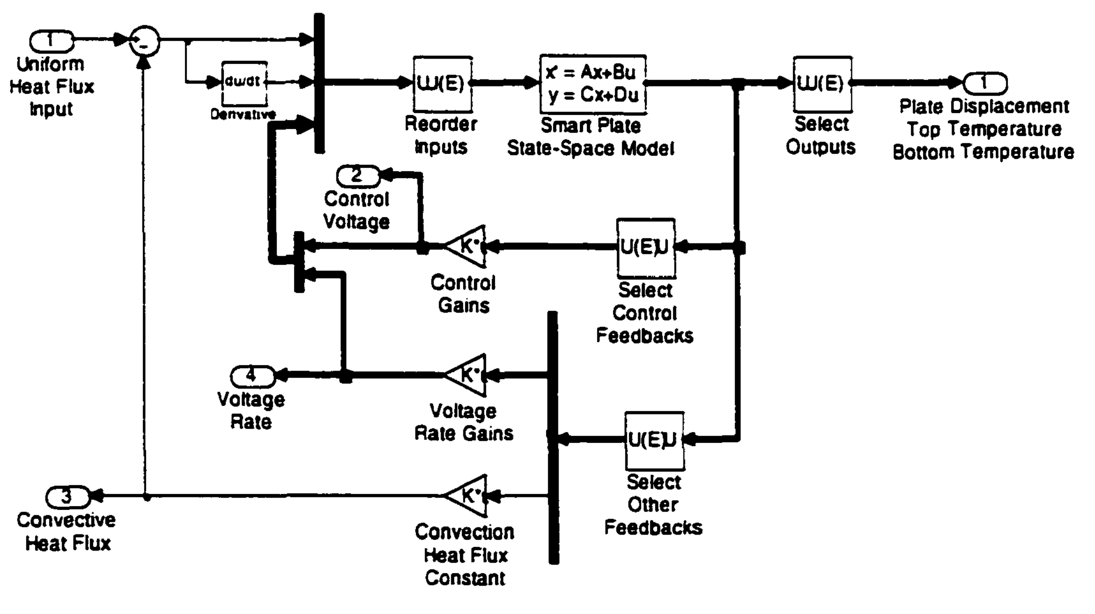

Figure 4.24: Linear Simulink model used to simulate thermal impulse closed loop response. The thick lines represent vector signals.

Table 4.4: Design Study 2 Results

Design	J μin · ms	max g NA	max $\lvert w(t)\rvert$ μin	max E $\frac{V}{in}$	min E $\frac{V}{in}$
Open-Loop	1.071×10^4	NA	0.5834	NA	NA
Initial Closed-Loop	3.492×10^4	−0.6667	2.2478	13.56	−19.84
Optimal Closed-Loop	2.258×10^3	−0.4227	0.9758	7.15	−5.38

After optimization, the constant feedback gains were $K_{pt} = -4.3532 \times 10^6 \frac{V}{C}$, $K_{rt} = 9.9796 \times 10^3 \frac{V}{A}$, $K_{pb} = 4.4804 \times 10^7 \frac{V}{C}$, and $K_{rb} = 1.0001 \times 10^4 \frac{V}{A}$. In this case the top position feedback gain is negative, which goes against intuition. Table 4.4 compares the open-loop response (with convective heat loss included), the initial closed-loop response, and the optimized closed-loop response. This table contains values for the cost, J, the constraint, g, the maximum absolute center plate deflection, max $|w(t)|$, and the maximum and minimum applied electric fields, E. Note that the initial design had a worse cost and significantly worse maximum absolute deflection than the open-loop design. This was a direct result of the complex interaction of the displacement, electrical, and thermal fields introduced by the pyroelectric constant. The optimal design had a significantly better cost than the open-loop design but a worse maximum absolute deflection. This was achieved by changing the sign on the position feedback gain for the top sensor/actuator pair. The other gains were not significantly changed. The net result of this design was to balance the thermal and control moments as time progressed. Figures 4.25 through 4.27 graphically compare the three designs. Figure 4.25 shows the center plate deflection for all three designs, in which the initial closed-loop design clearly had the worst response. The open loop response was also bad in that it did not decay very fast with time. This was a function of the poor conductivity of the graphite/epoxy and PZT. Figure 4.26 illustrates the change in temperature of the top center of the plate, which was dominated by the heat flux input and the conductive heat loss. The slight difference between the closed-loop responses and the open loop response was due to the voltage rate coupling. The initial design slightly lowered the peak temperature change, but added to the temperature as time increased. The optimal design slightly increased the peak temperature, but decreased the temperature as time increased. The two closed-loop designs had opposite effects due to the opposite sign on K_{pt}. Figure 4.27 illustrates the change in temperature of the bottom center of the plate. Both closed-loop designs had significantly more temperature change than the open-loop design, which was because of the coupling between the voltage rate and the thermal field in the actuator. The voltage rates were opposite due to the opposite direction of deflection between the two designs. Figures 4.28 and 4.29 compare the control voltages of the two closed-loop designs, which clearly indicates that the two designs used opposite control voltages to control the plate deflection. This design study clearly indicates that a controller designed for mechanically induced deflections/vibrations may be unsuitable to control thermally induced deflections/vibartions.

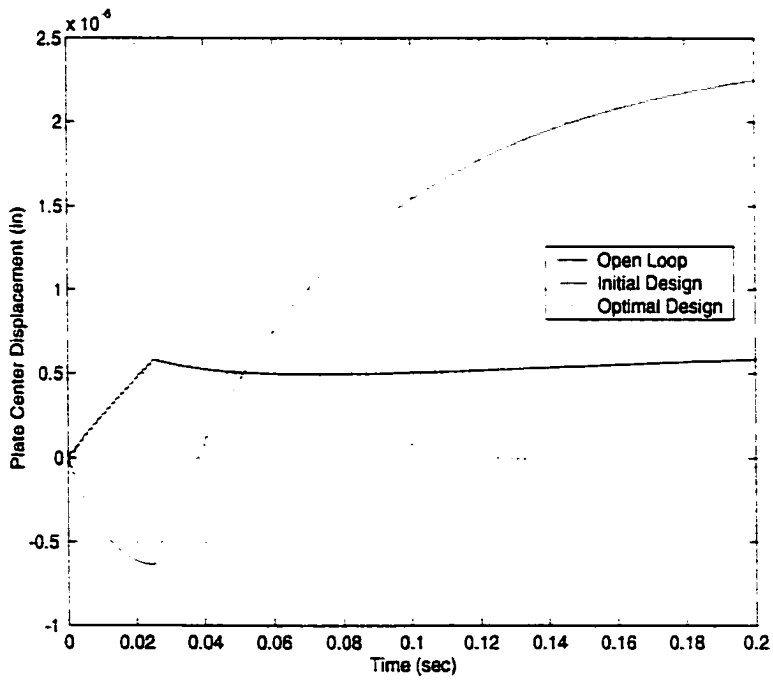

Figure 4.25: Comparison of plate center vertical displacement due to a heat flux impulse.

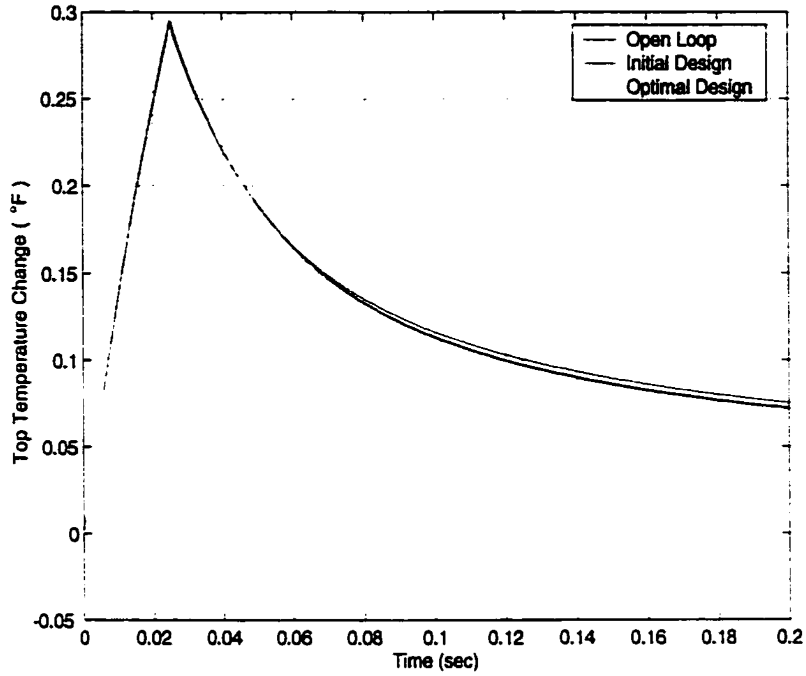

Figure 4.26: Comparison of plate top-center temperature change due to a heat flux impulse.

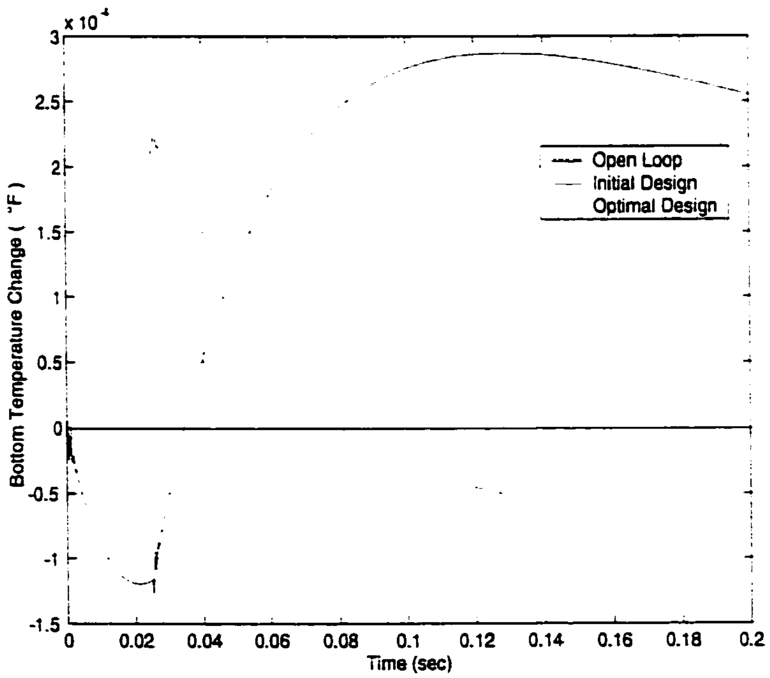

Figure 4.27: Comparison of plate bottom-center temperature change due to a heat flux impulse.

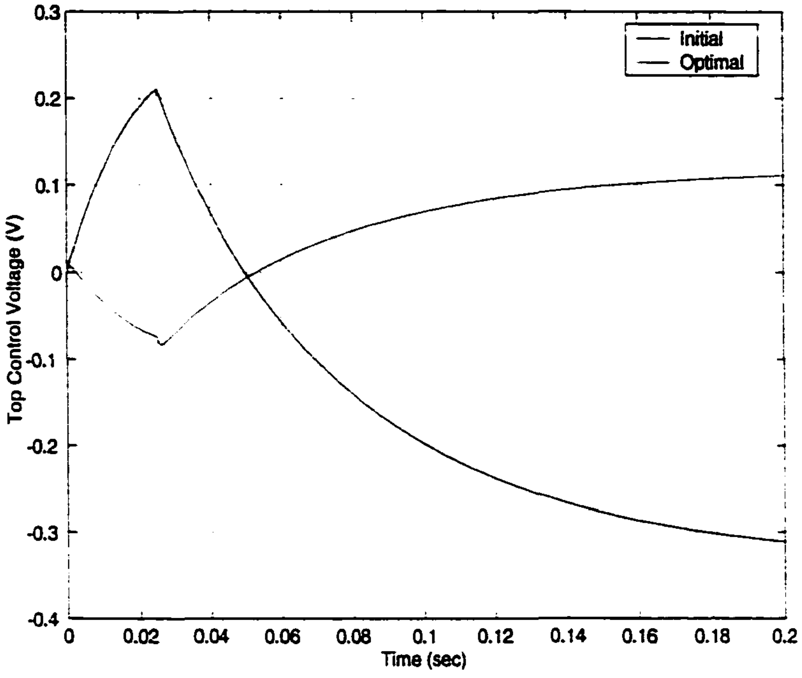

Figure 4.28: Top actuator control voltage comparison, initial closed-loop, and optimal closed-loop designs.

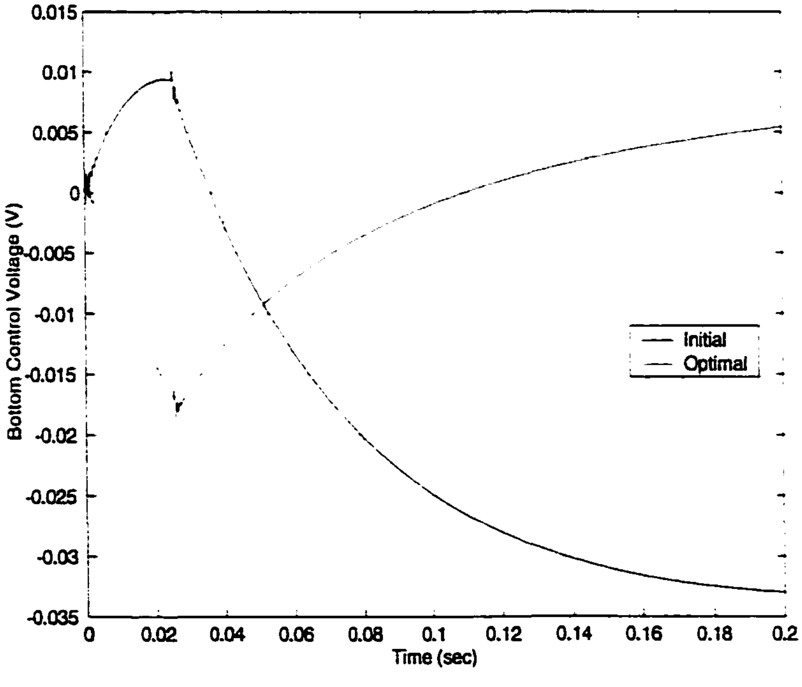

Figure 4.29: Bottom actuator control voltage comparison, initial closed-loop, and optimal closed-loop designs.

4.5 Summary

An approach for designing optimal controllers using classical performance and robustness measures was presented. This method automates the iterative design process by utilizng constrained optimization software to find a design that optimizes the required performance metric and meets the other design requirements by treating them as constraints. This method was demonstrated for two different smart plate control design problems: (i) a clamped graphite/epoxy/PZT smart plate subjected to a mechanical impulse, and (ii) a simply-supported graphite/epoxy/PZT smart plate subjected to a thermal impulse. The latter design study showed that the coupling between the displacement, electrical, and thermal fields, in a system excited by thermal inputs, can complicate the feedback control design.

CHAPTER 5

CONCLUSIONS AND FUTURE RESEARCH

5.1 Conclusions

From the results of the theory and the mathematical simulations described in the previous chapters, it is reasonalbe to conclude:

1. A theoretical solution was developed for the dynamic response of a symmetric, cross-ply, laminated composite plate subject to a thermal shock. The solution was validated by using it to determine the response of a homogeneous isotropic plate and comparing it to the response obtained from a solution derived specifically for homogeneous isotropic plates. Comparing the solution for the symmetric, cross-ply, laminated composite plate to the solution for an isotropic plate indicates that they have a very similar form. The main difference is that an explicit summation in the isotropic solution has been replaced by implied summations resulting from vector inner product multiplications in the composite solution.

2. A new finite element based method of solving coupled thermoelastic plate problems was developed. This method combines the accuracy and flexibility of solving the thermal portion of the plate problem using three-dimensional finite elements with the computationally efficient method of solving the mechanical portion of the plate problem using two-dimensional finite elements. The use of three-dimensional finite elements for the thermal portion of the model makes it possible to handle general thermal boundary conditions and internal heat sources. The main disadvantage is the large number of states required by this modeling technique which translates into more time required to perform simulations. This disadvantage can be partially overcome by applying advances in model reduction techniques developed by the control system theorists and advances in computer technology, which has produced inexpensive personal computers with sufficient computational horsepower and memory to handle high-order models.

3. An approach for designing optimal controllers using classical performance and robustness measures was presented. This method automates the iterative design process by utilizng optimiza-

tion software to find a design that optimizes the required performance metric and meets the design requirements.

5.2 Suggestions for Future Work

Subjects for further research related to the current work include:

1. Develop laboratory experiments to verify the coupled thermoelastic models developed in Chapters 2 and 3, and the smart plate feedback control designs developed in Chapter 4. Refine the models to account for differences in the experimental and theoretical results.

2. Extend the theoretical solution developed in Chapter 2 to nonsymmetric laminated composites which will have bending-extension coupling resulting in a set of four coupled partial differential equations. To extend this approach, the x and y boundary conditions must be consistent with modal expansion techniques.

3. Apply the coupled thermomechanical finite element model approach developed in Chapter 3 to include

   - Other plate geometries and shells
   - Internal heating
   - Anisotropic material properties, including anisotropic damping
   - Higher order plate theories
   - Higher order thermal theories.

4. Extend the finite element model developed in Chapter 3 to include the differential equations governing the electric potential. Compare the response of this higher fidelity model to mechanical and thermal loads to the response of the model developed in Chapter 3 and the model developed by Zhou *et al* [9]. This analysis will determine the validity of the assumptions and modeling approach applied in this work.

5. Develop modeling techniques to properly handle large changes in temperature. These techniques will have to account for the non-linearities in the governing thermal equations as well as the change of the material properties, mechanical, thermal, piezoelectric, and pyroelectric, with temperature.

6. Develop smart plate models that include the sensor and actuator dynamics including non-linear effects such as hysteresis and delays due to viscoelastic effects of the bonding material. Develop dynamic digital controllers and control system design methods that work with the non-linear effects incorporated into the smart plate model.

REFERENCES CITED

1. S. S. Rao and M. Sunar. Piezoelectricity and its use in disturbance sensing and control of flexible structures: A survey. Applied Mechanics Reviews. 47(4):113–123. 1994.

2. E. F. Crawley. Intelligent structures for aerospace: A technology overview and assessment. AIAA Journal. 32(8):1689–1699. 1994.

3. B. K. Wada. J. I. Fanson. and E. F. Crawley. Adaptive structures. Journal of Intelligent Material Systems and Structures. 1(2):157–174. 1990.

4. K. Chandrashekhara and K. Bhatia. Enhancement of buckling loads of laminated plates using piezoelectric devices. Composite Materials and Structures. ASME AMD-179:163–173. 1993.

5. T. R. Tauchert. Piezothermoelastic behavior of a laminate plate. Journal of Thermal Stresses. 15:25–37. 1992.

6. H. S. Tzou and R. V. Howard. A piezoelectric thin shell theory applied to active structures. Journal of Vibration and Acoustics. 116:295–302. 1994.

7. K. Chandrashekhara and M. Kolli. Thermally induced vibration of doubly curved composite shells with piezoelectric devices. In 36th AIAA/ASME/ASCE/AHS/ASC Structures, Structural Dynamics, and Materials Conference. pages 1628–1636. New Orleans. LA. 1995. AIAA.

8. Y. Y. Tang and K. Xu. Dynamic analysis of a piezothermoelastic laminated plate. Journal of Thermal Stresses. 18:87–104. 1995.

9. X. Zhou. A. Chattopadhyay. and H. Gu. Dynamic responses of smart composites using a coupled thermo-piezoelectric-mechanical model. AIAA Journal. 38(10):1939–1948. 2000.

10. B. A. Boley and J. H. Weiner. Theory of Thermal Stresses. Wiley. New York. 1960.

11. A. D. Kovalenko and V. G. Kharnaukhov. Vibrations of a circular plate induced by a thermal shock. Dokl. Akad. Nauk URSR. A(2). 1968.

12. V. I. Kozlov. Thermoelastic vibrations of a rectangular plate. Prikladnaya Mekhanika. 8(4):445–48. 1972.

13. T. J. Chung. Thermomechanical vibrations. Shock and Vibration Digest. 10(11):17–25. 1978.

14. J. Ignaczak. Linear dynamic thermoelasticity - a survey. Shock and Vibration Digest. 13(9):3–8. 1981.

15. J. Ignaczak. Linear dynamic thermoelasticity: A survey 1981-1984. Shock and Vibration Digest. 19(6):11-17. 1987.

16. T. R. Tauchert. Thermally induced flexure. buckling. and vibration of plates. Applied Mechanics Reviews. 44(8):347-360. 1991.

17. K. Chandrashekhara. Thermal buckling of laminated plates using a shear flexible finite element. Finite Elements in Analysis and Design. 12:51–61. 1992.

18. N. Mukherjee and P. K. Sinha. Thermal shocks in composite plates: A coupled thermoelastic finite element analysis. Composite Structures. 34:1–12. 1996.

19. K. K. Tamma and R. R. Namburu. Computational approaches with application to non-classical and classical thermomechanical problems. Applied Mechanics Reviews. 50(9):514–551. 1997.

20. J. R. Blandino and E. A. Thornton. Thermally induced vibration of an internally heated beam. ASME Journal of Vibration and Acoustics. 123:67–75. 2001.

21. E. F. Crawley and E. H. Anderson. Detailed models of piezoceramic actuation of beams. Journal of Intelligent Material Systems and Structures. 1:4–25. 1990.

22. E. F. Crawley and K. B. Lazarus. Induced strain actuation of isotropic and anisotropic plates. AIAA Journal. 29(6):944–951. 1991.

23. C. K. Lee. Piezoelectric laminates: Theory and experiments for distributed sensors and actuators. In H. S. Tzou and G. L. Anderson, editors, Intelligent Structural Systems, pages 75–167. Kluwer Academic Publishers, Dordrecht, The Netherlands, 1992.

24. K. Chandrashekhara and A. N. Agarwal. Active vibration control of laminated composite plates using piezoelectric devices: A finite element approach. Journal of Intelligent Material Systems and Structures, 4:496–508, 1993.

25. H. S. Tzou and H. Q. Fu. A study of segmentation of distributed piezoelectric sensors and actuators, part i: Theoretical analysis. Journal of Sound and Vibration, 172(2):247–259, 1994.

26. H. S. Tzou and H. Q. Fu. A study of segmentation of distributed piezoelectric sensors and actuators, part II: Parametric study and active vibration controls. Journal of Sound and Vibration, 172(2):261–275, 1994.

27. R. Barrett. Active plate and missile wing development using directionally attached piezoelectric elements. AIAA Journal, 32(3):601–609, 1994.

28. E. H. Anderson and N. W. Hagood. Simultaneous piezoelectric sensing/actuation: Analysis and application to controlled structures. Journal of Sound and Vibration, 174(5):617–639, 1994.

29. Y. Gu, R. L. Clark, C. R. Fuller, and A. C. Zander. Experiments on active control of plate vibration using piezoelectric actuators and polyvinylidene flouride (PVDF) modal sensors. ASME Journal of Vibration and Acoustics, 116:303–308, 1994.

30. J. A. Main and E. Garcia. Design impact of piezoelectric actuator nonlinearities. Journal of Guidance, Control, and Dynamics, 20(2):327–332, 1997.

31. P. C. Chen and I. Chopra. Wind tunnel test of a smart rotor model with individual blade twist control. Journal of Intelligent Material Systems and Structures, 8(5):414–425, 1997.

32. R. M. Barrett, R. S. Gross, and F. T. Brozoski. Design and testing of a subsonic all-moving adaptive flight control surface. AIAA Journal, 35(7):1217–1219, 1997.

33. W. Nowacki. Dynamic Problems of Thermoelasticity. Noordhoff International Publishing. Leyden. The Netherlands, 1975.

34. H. Lee and D. A. Saravanos. Coupled layerwise analysis of thermopiezoelectric composite beams. AIAA Journal, 34(6):1231-1237, 1996.

35. W. Smittakorn and P. R. Heyliger. A discrete-layer model of laminated hygrothermopiezoelectric plates. Mechanics of Composite Materials and Structures, 7:79–104, 2000.

36. Y. W. Kwon and H. Bang. The Finite Element Method using MATLAB, chapter 2, pages 31–45. CRC Press LLC, Boca Raton, 1997.

37. E. D. Sontag. Mathematical Control Theory, pages 359–364. Springer-Verlag, New York, 1990.

38. G. S. Larionov. Investigation of the vibrations of relaxing systems by the averaging method. Mekhanika Polimerov, (5):806–813, 1969.

39. J. E. Shigley and C. R. Mischke. Mechanical Engineering Design, page 729. McGraw-Hill Inc., New York, fifth edition, 1989.

40. Staff of Reasearch and Education Association. Handbook of Mathematical, Scientific, and Engineering Formulas, Tables, Functions, Graphs, Transforms, page 844. Research and Education Association, New York, 1984.

41. J. W. Weeton, D. M. Peters, and K. L. Thomas. Engineers' Guide to Composite Materials. American Society for Metals, 1987.

42. R. M. Jones. Mechanics of Composite Materials, Appendix A, pages 321–326. Hemisphere Publishing, New York, 1975.

43. M. N. Ozisik. Boundary Value Problems of Heat Conduction. Dover Publications, Mineola, N.Y., 1989.

44. P. C. Yang, C. H. Norris, and Y. Stavsky. Elastic wave propagation in heterogeneous plates. International Journal of Solids and Structures, 2:665–684, 1966.

45. C. W. Bert. Simplified analysis of static shear factors for beams of nonhomogeneous cross section. Journal of Composite Materials, 7:525–529, 1973.

46. J. N. Reddy. Energy and Variational Methods in Applied Mechanics. John Wiley and Sons, Inc., New York, 1984.

47. A. W. Al-Khafaji and J. R. Tooley. Numerical Methods in Engineering Practice, chapter 11, pages 393–406. Holt, Rinehart and Winston, Inc., 1986.

48. MATLAB : High Performance Numeric Computation and Visualization Software. The MathWorks, Natick, MA, 2000.

49. Piezoelectric Ceramics Data Book for Designers. Morgan Matroc Limited, Worcestershire, England.

50. R. Y. Chiang and M. G. Safonov. Robust Control Toolbox. The Mathworks, Inc., Natick, MA, 1992.

51. S. Skogestad and I. Postlethwaite. Multivariable Feedback Control Analysis and Design. John Wiley and Sons, New York, NY 10158-0012, USA, 1996.

52. J. R. Bar-on and E. A. Jonckheere. Phase margins for mutlivariable control systems. International Journal of Control, 52(2):485–498, 1990.

53. J. R. Bar-on and E. A. Jonckheere. The multivariable gain margin. International Journal of Control, 54(2):100–110, 1991.

54. G. J. Balas, J. C. Doyle, K. Glover, A. Packard, and R. Smith. μ-Analysis and Synthesis Toolbox. The Mathworks, Inc., Natick, MA, 1991.

55. D. G. Luenberger. Optimization by Vector Space Methods. John Wiley and Sons, New York, 1969.

56. D. E. Goldberg. Genetic Algorithms in Search, Optimization, and Machine Learning. Addison-Wesley, Reading, MA, 1989.

57. SIMULINK. The MathWorks, Natick, MA. 1994.

58. G. N. Vanderplaats and S. R. Hansen. DOT User's Manual, Version 2.04. VMA Engineering, 1989.

59. G.N. Vanderplaats. Numerical Optimization Techniques for Engineering Design: With Applications. McGraw Hill, New York, 1984.

60. MATLAB Application Program Interface Guide, Version 5. The MathWorks, Inc., Natick MA.

61. A. J. Chapman. Heat Transfer, Fourth Edition. Macmillan Publishing Co., New York, 1984.

62. G. S. Larionov. Solution of some dynamic problems of viscoelasticity theory by the averaging method. Mekhanika Polimerov, (2):246–252, 1970.

63. K. Zhou, J. C. Doyle, and K. Glover. Robust and Optimal Control. Prentice Hall, Englewood Cliffs, New Jersey, 1996.

64. R. A. Horn and C. R. Johnson. Topics In Matrix Analysis. Cambridge University Press, Cambridge, United Kingdom, 1991.

65. K. Bathe. Finite Element Procedures in Engineering Analysis. Prentice Hall, Englewood Cliffs, N.J., 1996.

APPENDIX A

ADDITIONAL DERIVATIONS AND SUPPLEMENTAL MATERIAL

A.1. Derivation of Dimensionless Differential Equations

Plate displacement equation

$$D_{11}\frac{\partial^4 w}{\partial x^4} + 2D_k\frac{\partial^4 w}{\partial x^2 \partial y^2} + D_{22}\frac{\partial^4 w}{\partial y^4} + m\frac{\partial^2 w}{\partial t^2} + \frac{\partial^2 m_{Tx}}{\partial x^2} + \frac{\partial^2 m_{Ty}}{\partial y^2} = 0 \tag{A.1}$$

Plate thermal equation

$$k_x\frac{\partial^2 T}{\partial x^2} + k_y\frac{\partial^2 T}{\partial y^2} + \frac{\partial}{\partial z}\left(k_z\frac{\partial T}{\partial z}\right) - \rho C_v\frac{\partial T}{\partial t} +$$
$$T_0 z\frac{\partial}{\partial t}\left[\left(Q_{11}\alpha_x + Q_{12}\alpha_y\right)\frac{\partial^2 w}{\partial x^2} + \left(Q_{12}\alpha_x + Q_{22}\alpha_y\right)\frac{\partial^2 w}{\partial y^2}\right] = 0 \tag{A.2}$$

where

$$D_k = D_{12} + 2D_{66} \tag{A.3}$$

$$m = \int_{-\frac{h}{2}}^{\frac{h}{2}} \rho dz = \sum_{i=1}^{N} h_i \rho_i \tag{A.4}$$

$$m_{Tx} = \int_{-\frac{h}{2}}^{\frac{h}{2}} \left(Q_{11}\alpha_x + Q_{12}\alpha_y\right)\left(T - T_0\right) z dz \tag{A.5}$$
$$m_{Ty} = \int_{-\frac{h}{2}}^{\frac{h}{2}} \left(Q_{12}\alpha_x + Q_{22}\alpha_y\right)\left(T - T_0\right) z dz$$

subject to the following initial and boundary conditions

$$\begin{aligned}
&w = 0; \quad \frac{\partial w}{\partial t} = 0; \quad T = T_0 \quad (t = 0);\\
&w = 0; \quad \frac{\partial^2 w}{\partial x^2} = 0 \quad (x = 0,\ x = a);\\
&w = 0; \quad \frac{\partial^2 w}{\partial y^2} = 0 \quad (y = 0,\ y = b);\\
&k_z\frac{\partial T}{\partial z} = q \quad (z = \frac{h}{2}); \quad \frac{\partial T}{\partial z} = 0 \quad (z = -\frac{h}{2});\\
&T = T_0 \quad (x = 0,\ x = a,\ y = 0,\ y = b).
\end{aligned} \tag{A.6}$$

To facilitate the solution, the following dimensionless quantities are introduced

$$\begin{aligned}
&\xi = \frac{x}{a}; \qquad \eta = \frac{y}{b}; \qquad \zeta = \frac{z}{h};\\
&\tau = \bar{k}_z\frac{t}{h^2\bar{\rho}\bar{C}_v}; \quad \Theta = \bar{k}_z\frac{T - T_0}{qh}; \quad W = \bar{k}_z\frac{w}{q\bar{\alpha}_x a^2};
\end{aligned} \tag{A.7}$$

where

$$\bar{k}_z = \frac{1}{h}\sum_{i=1}^{N} h_i k_{zi}; \quad \bar{\alpha}_x = \frac{1}{h}\sum_{i=1}^{N} h_i \alpha_{xi} \quad \bar{\rho} = \frac{1}{h}\sum_{i=1}^{N} h_i \rho_i \quad \bar{C}_v = \frac{1}{h}\sum_{i=1}^{N} h_i C_{vi} \tag{A.8}$$

Substitution of the appropriate terms from Equation $(A.7)$ into Equation $(A.1)$ yields

$$\frac{\partial^4 w}{\partial x^4} = \frac{q\bar{\alpha}_x}{a^2\bar{k}_z}\frac{\partial^4 W}{\partial \xi^4} \tag{A.9}$$

$$\frac{\partial^4 w}{\partial x^2 \partial y^2} = \frac{q\bar{\alpha}_x}{b^2\bar{k}_z}\frac{\partial^4 W}{\partial \xi^2 \partial \eta^2} \tag{A.10}$$

$$\frac{\partial^4 w}{\partial y^4} = \frac{q\bar{\alpha}_x a^2}{b^4\bar{k}_z}\frac{\partial^4 W}{\partial \eta^4} \tag{A.11}$$

$$\begin{aligned}\frac{\partial^2 w}{\partial t^2} &= \left(\frac{\bar{k}_z}{h^2\bar{\rho}\bar{C}_v}\right)^2\left(\frac{q\bar{\alpha}_x a^2}{\bar{k}_z}\right)\frac{\partial^2 W}{\partial \tau^2} \\ &= \frac{\bar{k}_z q\bar{\alpha}_x a^2}{\left(h^2\bar{\rho}\bar{C}_v\right)^2}\frac{\partial^2 W}{\partial \tau^2}\end{aligned} \tag{A.12}$$

$$\frac{\partial^2 m_{Tx}}{\partial x^2} = \frac{qh^3}{a^2\bar{k}_z}\frac{\partial^2}{\partial \xi^2}\int_{\frac{1}{2}}^{-\frac{1}{2}}\left(Q_{11}\alpha_x - Q_{12}\alpha_y\right)\Theta\zeta d\zeta \tag{A.13}$$

$$\frac{\partial^2 m_{Ty}}{\partial y^2} = \frac{qh^3}{b^2\bar{k}_z}\frac{\partial^2}{\partial \eta^2}\int_{\frac{1}{2}}^{-\frac{1}{2}}\left(Q_{12}\alpha_x - Q_{22}\alpha_y\right)\Theta\zeta d\zeta \tag{A.14}$$

Multiplying the resulting equation by $\frac{a^2\bar{k}_z}{D_{11}q\bar{\alpha}_x}$ yields

$$\frac{\partial^4 W}{\partial \xi^4} - 2C_1\frac{\partial^4 W}{\partial \xi^2\partial \eta^2} - C_2\frac{\partial^4 W}{\partial \eta^4} - \frac{1}{B^4}\frac{\partial^2 W}{\partial \tau^2} - \frac{\partial^2 M_{T\xi}}{\partial \xi^2} - \frac{\partial^2 M_{T\eta}}{\partial \eta^2} = 0 \tag{A.15}$$

$$\begin{aligned}&M_{T\xi} = \int_{-\frac{1}{2}}^{\frac{1}{2}} C_3(\zeta)\Theta\zeta d\zeta; &&M_{T\eta} = \int_{-\frac{1}{2}}^{\frac{1}{2}} C_4(\zeta)\Theta\zeta d\zeta; \\ &C_1 = \frac{D_k a^2}{D_{11}b^2}; &&C_2 = \frac{D_{22}a^4}{D_{11}b^4}; \\ &C_3(\zeta) = \frac{h^3}{D_{11}}\left(\frac{Q_{11}\alpha_x}{\bar{\alpha}_x} - \frac{Q_{12}\alpha_y}{\bar{\alpha}_x}\right); &&C_4(\zeta) = \frac{h^3a^2}{D_{11}b^2}\left(\frac{Q_{12}\alpha_x}{\bar{\alpha}_x} - \frac{Q_{22}\alpha_y}{\bar{\alpha}_x}\right)\end{aligned} \tag{A.16}$$

$$B^4 = \frac{D_{11}}{m}\left(\frac{h^2\bar{\rho}\bar{C}_v}{a^2\bar{k}_z}\right)^2 \tag{A.17}$$

The initial and boundary conditions for the non-dimensional displacement differential equation become

$$\begin{aligned}&W = 0; \quad \frac{\partial W}{\partial \tau} = 0; \quad \Theta = 0 \quad (\tau = 0) \\ &W = 0; \quad \frac{\partial^2 W}{\partial \xi^2} = 0 \quad (\xi = 0, \xi = 1) \\ &W = 0; \quad \frac{\partial^2 W}{\partial \eta^2} = 0 \quad (\eta = 0, \eta = 1)\end{aligned} \tag{A.18}$$

Substitution of the appropriate terms from Equation (A.7) into Equation (A.2) yields

$$\frac{\partial^2 T}{\partial x^2} = \frac{qh}{a^2\bar{k}_z}\frac{\partial^2\Theta}{\partial\xi^2} \tag{A.19}$$

$$\frac{\partial^2 T}{\partial y^2} = \frac{qh}{b^2\bar{k}_z}\frac{\partial^2\Theta}{\partial\eta^2} \tag{A.20}$$

$$\frac{\partial}{\partial z}\left(k_z\frac{\partial T}{\partial z}\right) = \frac{qh}{h^2\bar{k}_z}\frac{\partial}{\partial\zeta}\left(k_z\frac{\partial\Theta}{\partial\zeta}\right) \tag{A.21}$$

$$\begin{aligned}\frac{\partial T}{\partial t} &= \left(\frac{qh}{\bar{k}_z}\right)\left(\frac{\bar{k}_z}{h^2\bar{\rho}\bar{C}_v}\right)\frac{\partial\Theta}{\partial\tau}\\ &= \left(\frac{q}{h\bar{\rho}\bar{C}_v}\right)\frac{\partial\Theta}{\partial\tau}\end{aligned} \tag{A.22}$$

$$\begin{aligned}z\frac{\partial^3 w}{\partial t\partial x^2} &= h\left(\frac{\bar{k}_z}{h^2\bar{\rho}\bar{C}_v}\right)\left(\frac{q\bar{\alpha}_x a^2}{a^2\bar{k}_z}\right)\zeta\frac{\partial^3 W}{\partial\tau\partial\xi^2}\\ &= \left(\frac{q\bar{\alpha}_x}{h\bar{\rho}\bar{C}_v}\right)\zeta\frac{\partial^3 W}{\partial\tau\partial\xi^2}\end{aligned} \tag{A.23}$$

$$\begin{aligned}z\frac{\partial^3 w}{\partial t\partial y^2} &= h\left(\frac{\bar{k}_z}{h^2\bar{\rho}\bar{C}_v}\right)\left(\frac{q\bar{\alpha}_x a^2}{b^2\bar{k}_z}\right)\zeta\frac{\partial^3 W}{\partial\tau\partial\eta^2}\\ &= \left(\frac{q\bar{\alpha}_x a^2}{h\bar{\rho}\bar{C}_v b^2}\right)\zeta\frac{\partial^3 W}{\partial\tau\partial\eta^2}\end{aligned} \tag{A.24}$$

multiplying the resulting equation by $\frac{h\bar{\rho}\bar{C}_v}{q\rho C_v}$ yields

$$C_5\frac{\partial^2\Theta}{\partial\xi^2} - C_6\frac{\partial^2\Theta}{\partial\eta^2} - \frac{\partial}{\partial\zeta}\left(C_7\frac{\partial\Theta}{\partial\zeta}\right) - \frac{\partial\Theta}{\partial\tau} - \zeta\frac{\partial}{\partial\tau}\left(C_8\frac{\partial^2 W}{\partial\xi^2} - C_9\frac{\partial^2 W}{\partial\eta^2}\right) = 0 \tag{A.25}$$

$$C_5(\zeta) = \frac{h^2 k_x\bar{\rho}\bar{C}_v}{a^2\bar{k}_z\rho C_v}; \qquad C_6(\zeta) = \frac{h^2 k_y\bar{\rho}\bar{C}_v}{b^2\bar{k}_z\rho C_v}; \qquad C_7(\zeta) = \frac{k_z\bar{\rho}\bar{C}_v}{\bar{k}_z\rho C_v};$$

$$C_8(\zeta) = \frac{T_0 Q_{11}\bar{\alpha}_x}{\rho C_v}(\alpha_x - \nu_{21}\alpha_y); \quad C_9(\zeta) = \frac{T_0 Q_{22}\bar{\alpha}_x a^2}{\rho C_v b^2}(\nu_{12}\alpha_x - \alpha_y). \tag{A.26}$$

Since the boundary condition at z = $\frac{h}{2}$ is nonzero. the transformations of the variables needs to be applied to the boundary condition.

$$\begin{aligned}q &= k_z\frac{\partial T}{\partial z} = k_z\frac{\partial(T - T_0)}{\partial z}\\ &= k_z\left(\frac{qh}{\bar{k}_z h}\right)\frac{\partial\Theta}{\partial\zeta}\end{aligned} \tag{A.27}$$

$$q = q\frac{k_z}{\bar{k}_z}\frac{\partial\Theta}{\partial\zeta} \tag{A.28}$$

$$1 = C_{10}(\zeta)\frac{\partial\Theta}{\partial\zeta} \tag{A.29}$$

$$C_{10}(\zeta) = \frac{k_z}{\bar{k}_z} \tag{A.30}$$

The initial and boundary conditions for the non-dimensional thermal differential equation become

$$C_{10}(\zeta)\frac{\partial\Theta}{\partial\zeta} = 1 \qquad \left(\zeta = \frac{1}{2}\right); \qquad \frac{\partial\Theta}{\partial\zeta} = 0 \qquad \left(\zeta = -\frac{1}{2}\right)$$

$$\Theta = 0 \qquad (\xi = 0, \xi = 1, \eta = 0, \eta = 1) \tag{A.31}$$

A.2. Derivation of Displacement Integro-Differential Equation

The simplified coupled non-dimensional differential equation governing the displacement of a plate subject to a thermal impact. Equation (2.17), is repeated here for convenience

$$\frac{d^2W^*}{d\tau^2} - \omega_1^4 B^4 W^* = B^4 \int_{-\frac{1}{2}}^{\frac{1}{2}} \omega_2^2 \zeta \Theta^* d\zeta \tag{A.32}$$

Substituting Equation (2.25) into Equation (A.32) yields

$$\begin{aligned} \frac{d^2W^*}{d\tau^2} - \omega_1^4 B^4 W^* &= B^4 \sum_e \omega_{2i}^2 \int_{\zeta_i}^{\zeta_{i-1}} \zeta \left\{ \begin{matrix} H_1 & H_1 \end{matrix} \right\} d\zeta \left\{ \begin{matrix} \Theta_i^* \\ \Theta_{i-1}^* \end{matrix} \right\} \\ &= B^4 \sum_e \frac{\omega_{2i}^2 h_i}{6} \left\{ \begin{matrix} \zeta_{i-1} - 2\zeta_i & 2\zeta_{i-1} - \zeta_i \end{matrix} \right\} \left\{ \begin{matrix} \Theta_i^* \\ \Theta_{i-1}^* \end{matrix} \right\} \end{aligned} \tag{A.33}$$

summing over all elements yields

$$\begin{aligned} \frac{d^2W^*}{d\tau^2} - \omega_1^4 B^4 W^* &= -B^4 F \left\{ \begin{matrix} \Theta_1^*(\tau) \\ \Theta_2^*(\tau) \\ \vdots \\ \Theta_{k+1}^*(\tau) \end{matrix} \right\} \\ &= -B^4 F \left(\frac{4}{mn\pi^2} \mathcal{A}^{-1} [\exp(\mathcal{A}\tau) - I] \mathcal{B}_1 - \right. \\ &\quad \left. \int_0^\tau \exp(\mathcal{A}(\tau - \hat{\tau})) \mathcal{B}_2 \frac{dW^*}{d\hat{\tau}} d\hat{\tau} \right) \end{aligned} \tag{A.34}$$

with $\mathcal{A}$, $\mathcal{B}_1$, and $\mathcal{B}_2$ defined in Equation (2.37), and

$$-F = \sum_e \frac{\omega_{2i}^2 h_i}{6} \left\{ \begin{matrix} \zeta_{i+1} + 2\zeta_i & 2\zeta_{i+1} + \zeta_i \end{matrix} \right\} \tag{A.35}$$

In Equation (A.35) the negative sign was included so that Equation (A.34) can be written in a form similar to that of the integro-differential equation (Equation 11) in Kozlov

$$\frac{d^2W^*}{d\tau^2} + \omega_1^4 B^4 W^* = -B^4 \int_0^{\tau} G(\tau - \tilde{\tau}) \frac{dW^*}{d\tilde{\tau}} d\tilde{\tau} + \Phi(\tau) \tag{A.36}$$

where

$$G(\tau) = F \cdot \exp(\mathcal{A}(\tau))\, \mathcal{B}_2 \tag{A.37}$$

$$\Phi(\tau) = \frac{4B^4}{mn\pi^2} F \cdot \mathcal{A}^{-1} [I - \exp(\mathcal{A}\tau)]\, \mathcal{B}_1 \tag{A.38}$$

A.3. Application of Method of Averaging

This derivation will follow Example 1 in the paper by G. S. Larionov [62]. Since $|G(\tau - \tilde{\tau})| \ll \omega_1^4$ the Method of Averaging can be used to solve the integro-differential equation:

$$\frac{d^2W^*}{d\tau^2} + \omega_1^4 B^4 W^* = -B^4 \int_0^{\tau} G(\tau - \tilde{\tau}) \frac{dW^*}{d\tilde{\tau}} d\tilde{\tau} + \Phi(\tau) \tag{A.39}$$

Subject to

$$W^* = 0; \qquad \frac{dW^*}{d\tau} = 0 \qquad (\tau = 0) \tag{A.40}$$

To facilitate the solution of this equation, break the integro-differential equation into three parts.

$$W^* = W_1^* + W_2^* + W_3^* \tag{A.41}$$

where the three parts satisfy the following three differential equations.

$$\frac{d^2W_1^*}{d\tau^2} + \omega_1^4 B^4 W_1^* = -B^4 \int_0^{\tau} G(\tau - \tilde{\tau}) \frac{dW_1^*}{d\tilde{\tau}} d\tilde{\tau} \tag{A.42}$$

$$\frac{d^2W_2^*}{d\tau^2} + \omega_1^4 B^4 W_2^* = \frac{4B^4}{mn\pi^2} F \cdot \mathcal{A}^{-1} \mathcal{B}_1 \tag{A.43}$$

$$\frac{d^2W_3^*}{d\tau^2} + \omega_1^4 B^4 W_3^* = -\frac{4B^4}{mn\pi^2} F \cdot \mathcal{A}^{-1} \exp(\mathcal{A}\tau)\, \mathcal{B}_1 \tag{A.44}$$

For Equation (A.42) the Method of Averaging yields a solution of the following form.

$$W_1^*(\tau) = \exp(-\alpha_1 \tau) \left[c_1 \cos((\lambda\gamma + \alpha_2)\tau) + c_2 \sin((\lambda\gamma + \alpha_2)\tau)\right] \tag{A.45}$$

where

$$
\begin{aligned}
\alpha_1 &= \frac{\gamma^2}{2}\left\{F \cdot \int_0^\infty \exp(\mathcal{A}s)\cos(\lambda\gamma s)\,ds \cdot \mathcal{B}_2\right\} \\
\alpha_2 &= \frac{\gamma^2}{2}\left\{F \cdot \int_0^\infty \exp(\mathcal{A}s)\sin(\lambda\gamma s)\,ds \cdot \mathcal{B}_2\right\} \\
\lambda &= \omega_1^2 \\
\gamma &= B^2
\end{aligned}
\tag{A.46}
$$

and c_1 and c_2 are determined from the initial conditions. Solve the following integral using integration by parts:

$$
\begin{aligned}
\int_0^\infty \exp(\mathcal{A}s)\cos(\lambda\gamma s)\,ds &= \mathcal{A}^{-1}\exp(\mathcal{A}s)\cos(\lambda\gamma s)\big|_{s=0}^{\infty} - \\
&\quad \int_0^\infty \mathcal{A}^{-1}\exp(\mathcal{A}s)\left(-\lambda\gamma\sin(\lambda\gamma s)\right)ds \\
&= \mathcal{A}^{-1}(0 - I) - \lambda\gamma\mathcal{A}^{-1}\int_0^\infty \exp(\mathcal{A}s)\sin(\lambda\gamma s)\,ds \\
&= -\mathcal{A}^{-1} - \lambda\gamma\mathcal{A}^{-1}\left\{\mathcal{A}^{-1}\exp(\mathcal{A}s)\sin(\lambda\gamma s)\big|_{s=0}^{\infty} - \right. \\
&\quad \left. \int_0^\infty \mathcal{A}^{-1}\exp(\mathcal{A}s)\left(\lambda\gamma\cos(\lambda\gamma s)\right)ds\right\} \\
&= -\mathcal{A}^{-1} - \lambda\gamma\mathcal{A}^{-1}\left\{(0-0) - \right. \\
&\quad \left. \lambda\gamma\mathcal{A}^{-1}\int_0^\infty \exp(\mathcal{A}s)\cos(\lambda\gamma s)\,ds\right\} \\
&= -\mathcal{A}^{-1} - \lambda^2\gamma^2\mathcal{A}^{-2}\int_0^\infty \exp(\mathcal{A}s)\cos(\lambda\gamma s)\,ds
\end{aligned}
\tag{A.47}
$$

Rearranging yields

$$
\begin{aligned}
\int_0^\infty \exp(\mathcal{A}s)\cos(\lambda\gamma s)\,ds + \lambda^2\gamma^2\mathcal{A}^{-2}\int_0^\infty \exp(\mathcal{A}s)\cos(\lambda\gamma s)\,ds &= -\mathcal{A}^{-1} \\
\left(I - \lambda^2\gamma^2\mathcal{A}^{-2}\right)\int_0^\infty \exp(\mathcal{A}s)\cos(\lambda\gamma s)\,ds &= -\mathcal{A}^{-1}
\end{aligned}
\tag{A.48}
$$

which yields

$$
\begin{aligned}
\int_0^\infty \exp(\mathcal{A}s)\cos(\lambda\gamma s)\,ds &= -\left(I - \lambda^2\gamma^2\mathcal{A}^{-2}\right)^{-1}\mathcal{A}^{-1} \\
&= -\left(\mathcal{A}^2 - \lambda^2\gamma^2 I\right)^{-1}\mathcal{A}
\end{aligned}
\tag{A.49}
$$

Solve the integral in the definition of α_2 using integration by parts:

$$\begin{aligned}
\int_0^\infty \exp(\mathcal{A}s)\sin(\lambda\gamma s)\,ds &= \mathcal{A}^{-1}\exp(\mathcal{A}s)\sin(\lambda\gamma s)\Big|_{s=0}^{\infty} - \\
&\quad \int_0^\infty \mathcal{A}^{-1}\exp(\mathcal{A}s)(\lambda\gamma\cos(\lambda\gamma s))\,ds \\
&= \mathcal{A}^{-1}(0-0) - \lambda\gamma\mathcal{A}^{-1}\int_0^\infty \exp(\mathcal{A}s)\cos(\lambda\gamma s)\,ds \\
&= -\lambda\gamma\mathcal{A}^{-1}\Big\{\mathcal{A}^{-1}\exp(\mathcal{A}s)\cos(\lambda\gamma s)\Big|_{s=0}^{\infty} - \qquad\qquad (A.50) \\
&\quad \int_0^\infty \mathcal{A}^{-1}\exp(\mathcal{A}s)(-\lambda\gamma\sin(\lambda\gamma s))\,ds\Big\} \\
&= -\lambda\gamma\mathcal{A}^{-1}\{\mathcal{A}^{-1}(0-I) + \\
&\quad \lambda\gamma\mathcal{A}^{-1}\int_0^\infty \exp(\mathcal{A}s)\sin(\lambda\gamma s)\,ds\Big\} \\
&= \lambda\gamma\mathcal{A}^{-2} - \lambda^2\gamma^2\mathcal{A}^{-2}\int_0^\infty \exp(\mathcal{A}s)\sin(\lambda\gamma s)\,ds
\end{aligned}$$

Rearranging yields

$$\begin{aligned}
\int_0^\infty \exp(\mathcal{A}s)\sin(\lambda\gamma s)\,ds + \lambda^2\gamma^2\mathcal{A}^{-2}\int_0^\infty \exp(\mathcal{A}s)\sin(\lambda\gamma s)\,ds &= \lambda\gamma\mathcal{A}^{-2} \\
(I + \lambda^2\gamma^2\mathcal{A}^{-2})\int_0^\infty \exp(\mathcal{A}s)\sin(\lambda\gamma s)\,ds &= \lambda\gamma\mathcal{A}^{-2} \qquad (A.51)
\end{aligned}$$

which yields

$$\begin{aligned}
\int_0^\infty \exp(\mathcal{A}s)\sin(\lambda\gamma s)\,ds &= \lambda\gamma\left(I + \lambda^2\gamma^2\mathcal{A}^{-2}\right)^{-1}\mathcal{A}^{-2} \\
&= \lambda\gamma\left(\mathcal{A}^2 + \lambda^2\gamma^2 I\right)^{-1} \qquad (A.52)
\end{aligned}$$

Substituting Equationa (A.49) and (A.52) into Equation (A.46) yields

$$\begin{aligned}
\alpha_1 &= -\frac{B^4}{2}F\cdot\left(\mathcal{A}^2 + \omega_1^4 B^4 I\right)^{-1}\mathcal{A}\mathcal{B}_2 \\
\alpha_2 &= \frac{\omega_1^2 B^6}{2}F\cdot\left(\mathcal{A}^2 + \omega_1^4 B^4 I\right)^{-1}\mathcal{B}_2 \qquad (A.53)
\end{aligned}$$

The solution of Equation (A.43) has the form of a constant

$$W_2^* = c_3 \qquad (A.54)$$

Substitution into Equation (A.43) yields

$$\begin{aligned}
0 + c_3\omega_1^4 B^4 &= \frac{4B^4}{mn\pi^2}F\cdot\mathcal{A}^{-1}\mathcal{B}_1 \qquad (A.55) \\
c_3 &= \frac{4}{mn\pi^2\omega_1^4}F\cdot\mathcal{A}^{-1}\mathcal{B}_1 \qquad (A.56)
\end{aligned}$$

so

$$W_2^* = \frac{4}{mn\pi^2\omega_1^4} F \cdot \mathcal{A}^{-1}\mathcal{B}_1 \tag{A.57}$$

The solution of Equation ($A.44$) has the form

$$W_3^* = c_4 F \cdot \left(\mathcal{A}^2 + \omega_1^4 B^4 I\right)^{-1} \mathcal{A}^{-1} \exp\left(\mathcal{A}\tau\right) \mathcal{B}_1 \tag{A.58}$$

Substitution into Equation ($A.44$) yields

$$\begin{aligned}
c_4 F \cdot \left(\mathcal{A}^2 + \omega_1^4 B^4 I\right)\left(\mathcal{A}^2 + \omega_1^4 B^4 I\right)^{-1} \mathcal{A}^{-1} \exp\left(\mathcal{A}\tau\right) \mathcal{B}_1 &= -\frac{4B^4}{mn\pi^2} F \cdot \mathcal{A}^{-1} \exp\left(\mathcal{A}\tau\right) \mathcal{B}_1 && \text{(A.59)} \\
c_4 F \cdot \mathcal{A}^{-1} \exp\left(\mathcal{A}\tau\right) \mathcal{B}_1 &= -\frac{4B^4}{mn\pi^2} F \cdot \mathcal{A}^{-1} \exp\left(\mathcal{A}\tau\right) \mathcal{B}_1 && \text{(A.60)} \\
c_4 &= -\frac{4B^4}{mn\pi^2} && \text{(A.61)}
\end{aligned}$$

so

$$\begin{aligned}
W_3^* &= -\frac{4B^4}{mn\pi^2} F \cdot \left(\mathcal{A}^2 + \omega_1^4 B^4 I\right)^{-1} \mathcal{A}^{-1} \exp\left(\mathcal{A}\tau\right) \mathcal{B}_1 \\
&= -\frac{4B^4}{mn\pi^2} F \cdot \left(\mathcal{A}^2 + \omega_1^4 B^4 I\right)^{-1} \exp\left(\mathcal{A}\tau\right) \mathcal{A}^{-1} \mathcal{B}_1 && \text{(A.62)}
\end{aligned}$$

Use initial conditions. Equations (2.43) to determine constants c_1 and c_2.

$$\begin{aligned}
W^*(0) &= 0 && \text{(A.63)} \\
W_1^*(0) + W_2^*(0) + W_3^*(0) &= 0 && \text{(A.64)} \\
c_1 + \frac{4}{mn\pi^2\omega_1^4} F \cdot \mathcal{A}^{-1}\mathcal{B}_1 - \frac{4B^4}{mn\pi^2} F \cdot \left(\mathcal{A}^2 + \omega_1^4 B^4 I\right)^{-1} \mathcal{A}^{-1}\mathcal{B}_1 &= 0 && \text{(A.65)}
\end{aligned}$$

solving for c_1 yields

$$\begin{aligned}
c_1 &= \frac{4}{mn\pi^2} F \cdot \left\{-\frac{1}{\omega_1^4} I + B^4 \left(\mathcal{A}^2 + \omega_1^4 B^4 I\right)^{-1}\right\} \mathcal{A}^{-1}\mathcal{B}_1 \\
&= \frac{4}{mn\pi^2\omega_1^4} F \cdot \left\{-\left(\mathcal{A}^2 + \omega_1^4 B^4 I\right) + \omega_1^4 B^4 I\right\} \left(\mathcal{A}^2 + \omega_1^4 B^4 I\right)^{-1} \mathcal{A}^{-1}\mathcal{B}_1 \\
&= \frac{4}{mn\pi^2\omega_1^4} F \cdot \left\{-\mathcal{A}^2 - \omega_1^4 B^4 I + \omega_1^4 B^4 I\right\} \left(\mathcal{A}^2 + \omega_1^4 B^4 I\right)^{-1} \mathcal{A}^{-1}\mathcal{B}_1 \\
&= -\frac{4}{mn\pi^2\omega_1^4} F \cdot \mathcal{A}^2 \left(\mathcal{A}^2 + \omega_1^4 B^4 I\right)^{-1} \mathcal{A}^{-1}\mathcal{B}_1 \\
&= -\frac{4}{mn\pi^2\omega_1^4} F \cdot \left(\mathcal{A}^2 + \omega_1^4 B^4 I\right)^{-1} \mathcal{A}\mathcal{B}_1 && \text{(A.66)}
\end{aligned}$$

The initial condition on the derivative yields

$$\frac{dW^*(0)}{d\tau} = 0 \tag{A.67}$$

$$\frac{dW_1^*(0)}{d\tau} + 0 + \frac{dW_3^*(0)}{d\tau} = 0 \tag{A.68}$$

$$\frac{4}{mn\pi^2} F \cdot \left(\frac{\alpha_1}{\omega_1^4} \mathcal{A} - B^4 I \right) \left(\mathcal{A}^2 + \omega_1^4 B^4 I \right)^{-1} \mathcal{B}_1 - c_2 \left(\lambda\gamma + \alpha_2 \right) = 0 \tag{A.69}$$

Solving for c_2 yields

$$c_2 = \frac{4}{mn\pi^2 \left(\lambda\gamma + \alpha_2 \right)} F \cdot \left(B^4 I - \frac{\alpha_1}{\omega_1^4} \mathcal{A} \right) \left(\mathcal{A}^2 + \omega_1^4 B^4 I \right)^{-1} \mathcal{B}_1 \tag{A.70}$$

For $\alpha_2 \ll \lambda\gamma$, and $\left\| \frac{\alpha_1}{\omega_1^4} \mathcal{A} \right\| \ll \left\| B^4 I \right\|$, c_2 can be approximated by

$$\begin{aligned} c_2 &\approx \frac{4B^4}{mn\pi^2 \lambda\gamma} F \cdot \left(\mathcal{A}^2 + \omega_1^4 B^4 I \right)^{-1} \mathcal{B}_1 \\ &= \frac{4B^4}{mn\pi^2 \omega_1^2 B^2} F \cdot \left(\mathcal{A}^2 + \omega_1^4 B^4 I \right)^{-1} \mathcal{B}_1 \\ &= \frac{4B^2}{mn\pi^2 \omega_1^2} F \cdot \left(\mathcal{A}^2 + \omega_1^4 B^4 I \right)^{-1} \mathcal{B}_1 \end{aligned} \tag{A.71}$$

Substituting Equations (A.45), (A.57), (A.62), (A.66), and (A.71) into Equation (A.41) yields

$$\begin{aligned} W^* = {} & \exp\left(-\alpha_1 \tau \right) \left[-\frac{4}{mn\pi^2 \omega_1^4} \cos\left(\left(\omega_1^2 B^2 + \alpha_2 \right) \tau \right) F \cdot \left(\mathcal{A}^2 + \omega_1^4 B^4 I \right)^{-1} \mathcal{A} \mathcal{B}_1 - \right. \\ & \left. \frac{4B^2}{mn\pi^2 \omega_1^2} \sin\left(\left(\omega_1^2 B^2 + \alpha_2 \right) \tau \right) F \cdot \left(\mathcal{A}^2 + \omega_1^4 B^4 I \right)^{-1} \mathcal{B}_1 \right] + \\ & \frac{4}{mn\pi^2 \omega_1^4} F \cdot \mathcal{A}^{-1} \mathcal{B}_1 - \frac{4B^4}{mn\pi^2} F \cdot \left(\mathcal{A}^2 + \omega_1^4 B^4 I \right)^{-1} \exp\left(\mathcal{A}\tau \right) \mathcal{A}^{-1} \mathcal{B}_1 \end{aligned} \tag{A.72}$$

Simplifying the above equation yields

$$\begin{aligned} W^* = {} & \frac{4}{mn\pi^2 \omega_1^4} F \cdot \left\langle \left\{ \exp\left(-\alpha_1 \tau \right) \left[-\cos\left(\left(\omega_1^2 B^2 + \alpha_2 \right) \tau \right) \mathcal{A} - \right. \right. \right. \\ & \left. \omega_1^2 B^2 \sin\left(\left(\omega_1^2 B^2 + \alpha_2 \right) \tau \right) I \right] - \omega_1^4 B^4 \mathcal{A}^{-1} \exp\left(\mathcal{A}\tau \right) \Big\} \left(\mathcal{A}^2 + \omega_1^4 B^4 I \right)^{-1} + \\ & \left. \mathcal{A}^{-1} \right\rangle \mathcal{B}_1 \end{aligned} \tag{A.73}$$

The above equation can be further simplified by considering

$$
\begin{aligned}
-\omega_1^4 B^4 \mathcal{A}^{-1} \exp(\mathcal{A}\tau)\left(\mathcal{A}^2+\omega_1^4 B^4 I\right)^{-1} &= \mathcal{A}^{-1}\left[\mathcal{A}^2 \exp(\mathcal{A}\tau)-\mathcal{A}^2 \exp(\mathcal{A}\tau)-\right. \\
&\quad \left.\omega_1^4 B^4 \exp(\mathcal{A}\tau)\right]\left(\mathcal{A}^2+\omega_1^4 B^4 I\right)^{-1} \\
&= \mathcal{A}^{-1}\left[\mathcal{A}^2 \exp(\mathcal{A}\tau)-\exp(\mathcal{A}\tau) \times\right. \qquad (A.74) \\
&\quad \left.\left(\mathcal{A}^2+\omega_1^4 B^4 I\right)\right]\left(\mathcal{A}^2+\omega_1^4 B^4 I\right)^{-1} \\
&= \mathcal{A} \exp(\mathcal{A}\tau)\left(\mathcal{A}^2+\omega_1^4 B^4 I\right)^{-1}-\mathcal{A}^{-1} \exp(\mathcal{A}\tau)
\end{aligned}
$$

Substituting this relationship into the equation for W^* and rearranging yields

$$
\begin{aligned}
W^* &= \frac{4}{mn\pi^2\omega_1^4} F \cdot \left\langle \left\{\exp(-\alpha_1\tau)\left[-\cos\left(\left(\omega_1^2 B^2+\alpha_2\right)\tau\right)\mathcal{A}+\right.\right.\right. \\
&\quad \left.\left.\omega_1^2 B^2 \sin\left(\left(\omega_1^2 B^2+\alpha_2\right)\tau\right) I\right]+\mathcal{A}\exp(\mathcal{A}\tau)\right\}\left(\mathcal{A}^2+\omega_1^4 B^4 I\right)^{-1}- \\
&\quad \left.\mathcal{A}^{-1}(I-\exp(\mathcal{A}\tau))\right\rangle B_1 \qquad (A.75)
\end{aligned}
$$

A.4. Model Reduction by Balanced Truncation

Consider an n^{th} order stable linear time invariant (LTI) state space system

$$\dot{x} = Ax + Bu \qquad (A.76)$$

$$y = Cx + Du \qquad (A.77)$$

and suppose the realization of the system is balanced. *i.e.*, its controllability and observability Gramians are equal and diagonal. Denoting the balanced Gramians by Σ, then this requires that the Gramians satisfy the following Lyapunov equations

$$A\Sigma + \Sigma A^* + BB^* = 0 \qquad (A.78)$$

$$A^*\Sigma + \Sigma A + C^*C = 0. \qquad (A.79)$$

where Equation $(A.78)$ is the controllability Lyapunov equation and Equation $(A.79)$ is the observability Lyapunov equation. The system can also be described using the transfer function form

$$G(s) = C(sI - A)^{-1} B + D \qquad (A.80)$$

or in a more compact notation

$$G(s)=\left[\begin{array}{c|c} A & B \\ \hline C & D \end{array}\right]. \tag{A.81}$$

Partition the balanced Gramian as

$$\Sigma=\begin{bmatrix} \Sigma_1 & 0 \\ 0 & \Sigma_2 \end{bmatrix} \tag{A.82}$$

where

$$\Sigma_1 = diag\,(\sigma_1 I_{s_1}, \sigma_2 I_{s_2}, \ldots, \sigma_r I_{s_r}) \tag{A.83}$$

$$\Sigma_2 = diag\,(\sigma_{r+1} I_{s_{r+1}}, \sigma_{r+2} I_{s_{r+2}}, \ldots, \sigma_N I_{s_N}) \tag{A.84}$$

and

$$\sigma_1 > \sigma_2 > \cdots > \sigma_r > \sigma_{r+1} > \sigma_{r+2} > \cdots > \sigma_N \tag{A.85}$$

where σ_i has multiplicity s_i, $i = 1, 2, \ldots, N$ and $s_1 + s_2 + \cdots + s_N = n$. If the system is partitioned in accordance with the partitioning of the Gramian

$$G(s)=\left[\begin{array}{cc|c} A_{11} & A_{12} & B_1 \\ A_{21} & A_{22} & B_2 \\ \hline C_1 & C_2 & D \end{array}\right] \tag{A.86}$$

then the truncated system

$$G_r(s)=\left[\begin{array}{c|c} A_{11} & B_1 \\ \hline C_1 & D \end{array}\right] \tag{A.87}$$

is balanced and asymptotically stable with the bound on the $\mathcal{L}_\infty$ norm of the error given by

$$\|G(s) - G_r(s)\|_\infty \le 2\,(\sigma_{r+1} + \sigma_{r+2} + \cdots + \sigma_N)\,. \tag{A.88}$$

For a proof of Equation (A.88) and an algorithm for obtaining a balanced state space realization the reader is referred to the text by Zhou et. al. [63]. For a detailed presentation and solutions of Lyapunov equations, the reader is referred to the text by Horn and Johnson [64].

A.5. State-Space Solution Method

This section develops an alternate solution to the thermal impact problem solved in Chapter 2, which will be referred to as the State-Space solution method. The simplified coupled non-dimensional differential equations governing the thermal impact problem, Equations (2.17) and (2.18), are repeated here for convenience

$$\begin{aligned} \frac{d^2W^*}{d\tau^2} - \omega_1^4 B^4 W^* &= B^4 \int_{-\frac{1}{2}}^{\frac{1}{2}} \omega_2^2 \zeta \Theta^* d\zeta \qquad (A.89) \\ \frac{\partial}{\partial \zeta}\left(C_7 \frac{\partial \Theta^*}{\partial \zeta}\right) - \frac{\partial \Theta^*}{\partial \tau} - \omega_3^2 \Theta^* &= \omega_4^2 \zeta \frac{dW^*}{d\tau} \qquad (A.90) \end{aligned}$$

subject to the following initial and boundary conditions

$$\begin{gathered} W^* = 0; \quad \frac{\partial W^*}{\partial \tau} = 0; \quad \Theta^* = 0 \quad (\tau = 0) \\ C_7 \frac{\partial \Theta^*}{\partial \zeta} = \frac{4}{mn\pi^2} \quad (m, n = 1, 3, 5, \ldots) \quad \left(\zeta = \frac{1}{2}\right) \qquad (A.91) \\ \frac{\partial \Theta^*}{\partial \zeta} = 0 \quad \left(\zeta = -\frac{1}{2}\right). \end{gathered}$$

where the boundary condition at $\zeta = \frac{1}{2}$ is for a non-dimensional unit heat flux. Applying the finite element method as outlined in Chapter 2 to Equation (A.90) yields

$$\left\{ \begin{array}{c} \dot{\Theta}_1^* \\ \dot{\Theta}_2^* \\ \vdots \\ \dot{\Theta}_{k-1}^* \end{array} \right\} - A \left\{ \begin{array}{c} \Theta_1^* \\ \Theta_2^* \\ \vdots \\ \Theta_{k-1}^* \end{array} \right\} = B \left\{ \begin{array}{c} \frac{4}{mn\pi^2} \\ \frac{dW^*}{d\tau} \end{array} \right\} \qquad (A.92)$$

Define the following states

$$
\begin{aligned}
x_1 &= W^* \\
x_2 &= \dot{x}_1 = \frac{dW^*}{d\tau} \\
x_3 &= \Theta_1^* \\
x_4 &= \Theta_2^* \\
&\vdots \\
x_{k+2} &= \Theta_k^* \\
x_{k+3} &= \Theta_{k+1}^*
\end{aligned}
\tag{A.93}
$$

which allow us to couple Equation (A.89) with Equation (A.92) to yield

$$
\begin{Bmatrix} \dot{x}_1 \\ \dot{x}_2 \\ \vdots \\ \dot{x}_{k+3} \end{Bmatrix} = \mathbb{A}_{mn} \begin{Bmatrix} x_1 \\ x_2 \\ \vdots \\ x_{k+3} \end{Bmatrix} + \mathbb{B}_{mn}
\tag{A.94}
$$

where

$$
\mathbb{A}_{mn} = \begin{bmatrix} 0 & 1 & \begin{bmatrix} 0 & \cdots & 0 \end{bmatrix} \\ -\omega_1^4 B^4 & 0 & B^4 F \\ 0 & & \\ \vdots & \mathcal{B}_2 & \mathcal{A} \\ 0 & & \end{bmatrix}
\tag{A.95}
$$

$$
\begin{aligned}
F &= \sum_e \left[\int_{\zeta_i}^{\zeta_{i+1}} \omega_{2i}^2 \zeta \begin{Bmatrix} H_1 & H_2 \end{Bmatrix} d\zeta \right] \\
&= \sum_e \frac{\omega_{2i}^2 h_i}{6} \begin{Bmatrix} \zeta_{i+1} + 2\zeta_i & 2\zeta_{i+1} + \zeta_i \end{Bmatrix}
\end{aligned}
\tag{A.96}
$$

$$
\mathbb{B}_{mn} = \begin{bmatrix} 0 \\ 0 \\ \dfrac{4}{mn\pi^2} \mathcal{B}_1 \end{bmatrix}
\tag{A.97}
$$

For improved computational speed during numerical simulation, the order of Equation (A.94) can be reduced using the balanced model reduction technique outlined in the previous section [63]. Note that further reduction in the number of states is possible if the plate is square and the material is homogenous since symmetry yields

$$\mathbb{A}_{ij} = \mathbb{A}_{ji} \tag{A.98}$$

$$\mathbb{B}_{ij} = \mathbb{B}_{ji} \tag{A.99}$$

$$\mathbb{C}_{ij} = \mathbb{C}_{ji} \tag{A.100}$$

To obtain the state-space model for the plate, assemble the modal state and input matrices, $\mathbb{A}_{mn}$ and $\mathbb{B}_{mn}$, respectively, as follows

$$\mathbb{A} = \begin{bmatrix} \mathbb{A}_{11} & & & & \\ & \mathbb{A}_{13} & & & \\ & & \mathbb{A}_{31} & & \\ & & & \ddots & \\ & & & & \mathbb{A}_{ii} \end{bmatrix} \tag{A.101}$$

$$\mathbb{B} = \begin{bmatrix} \mathbb{B}_{11} \\ \mathbb{B}_{13} \\ \mathbb{B}_{31} \\ \vdots \\ \mathbb{B}_{ii} \end{bmatrix} \tag{A.102}$$

where ii is the highest order mode to be incorporated into the model. To obtain the center plate deflection as the output of the system define

$$\mathbb{C} = \begin{bmatrix} \mathbb{C}_{11} & \mathbb{C}_{13} & \mathbb{C}_{31} & & \mathbb{C}_{ii} \end{bmatrix} \tag{A.103}$$

$$\mathbb{C}_{mn} = \begin{bmatrix} 4\sin\left(\frac{m\pi}{2}\right)\sin\left(\frac{n\pi}{2}\right) & 0 & \cdots & 0 \end{bmatrix} \tag{A.104}$$

Other outputs can be obtained such as the non-dimensional temperature at the top center of the plate through appropriate choice of the $\mathbb{C}_{mn}$ matrix. The complete state-space model is

$$\begin{aligned} \dot{x} &= \mathbb{A}x + \mathbb{B}\bar{q}(\tau) && \text{(A.105)} \\ w_0 &= \mathbb{C}x && \text{(A.106)} \end{aligned}$$

where $\bar{q}(\tau)$ represents a non-dimensional heat flux and w_0 represents the displacement at the center of the plate. The solution to Equation (A.105) is obtained using the variation of parameters method [37] and is given by

$$x = \exp(\mathbb{A}\tau)\,x_0 + \int_0^{\tau} \exp(\mathbb{A}(\tau - \hat{\tau}))\,\mathbb{B}\bar{q}\,d\hat{\tau} \tag{A.107}$$

where x_0 is the initial condition of the state vector given by Equation (A.93). For a general non-dimensional time varying input, the integral in Equation (A.107) is not solvable analytically and, therefore, can only be solved numerically. The most common approach to solving the general case of Equation (A.105) is to numerically integrate the differential equations instead of using Equation (A.107). For a constant input $\bar{q}$, Equation (A.107) becomes

$$x = \exp(\mathbb{A}\tau)\,x_0 + \mathbb{A}^{-1}[\exp(\mathbb{A}\tau) - I]\,\mathbb{B}\bar{q} \tag{A.108}$$

and

$$w_0 = \mathbb{C}\left\{\exp(\mathbb{A}\tau)\,x_0 + \mathbb{A}^{-1}[\exp(\mathbb{A}\tau) - I]\,\mathbb{B}\bar{q}\right\} \tag{A.109}$$

where

$$\exp(\mathbb{A}\tau) = P \begin{bmatrix} \exp(\lambda_1\tau) & & & & \\ & \exp(\lambda_2\tau) & & & \\ & & \exp(\lambda_3\tau) & & \\ & & & \ddots & \\ & & & & \exp(\lambda_N\tau) \end{bmatrix} P^{-1} \tag{A.110}$$

The λ_i and P are found from the eigenvalue decomposition of $\mathbb{A}$

$$A = P\Lambda P^{-1} \tag{A.111}$$

$$\Lambda = \begin{bmatrix} \lambda_1 & & & & \\ & \lambda_2 & & & \\ & & \lambda_3 & & \\ & & & \ddots & \\ & & & & \lambda_N \end{bmatrix} \tag{A.112}$$

$$P = \begin{bmatrix} p_1 & p_2 & p_3 & \cdots & p_N \end{bmatrix} \tag{A.113}$$

where the λ_i are the eigenvalues of $\mathbb{A}$ and the p_i are the associated eigenvectors.

A comparison between the solution obtained by Equation (A.109) and the solution for the plate center deflection using the Method of Averaging follows. The solution using Equation (A.109) was obtained for the graphite-epoxy plate described in Chapter 2. $\bar{q} = 1$. $m, n = 1, 3, \ldots, 17$ and balanced model reduction with a total infinity norm error tolerance of 1×10^{-12} applied to the systems defined by $\mathbb{A}_{mn}$, $\mathbb{B}_{mn}$, and $\mathbb{C}_{mn}$ and balanced model reduction with a total infinity norm error tolerance of 1×10^{-11} applied to the systems defined by $\mathbb{A}$, $\mathbb{B}$, and $\mathbb{C}$. This resulted in a system with 386 states. Figure A.1 shows the comparison of the quasi-static center plate deflection for time from 0 to 25 seconds for both solutions. Figure A.2 shows the comparison of the center plate deflection for time from 0 to 0.015 seconds for both solutions. Figure A.3 shows the comparison of the center plate deflection for time from 25 to 25.015 seconds for both solutions. Note that a small (7.82×10^{-10}) steady state offset was removed so that the oscillations could be compared. This offset was due to the error introduced by using fewer modes, 17 vs. 21, and model reduction. This figure illustrates that the dynamic deflection has the same frequency of oscillation and decay for both solutions. These figures illustrate that the two solutions compare favorably.

One advantage of the State-Space solution method over the Method of Averaging solution developed in Chapter 2 is that it can handle more general thermal heat flux inputs and does not require any additional assumptions.

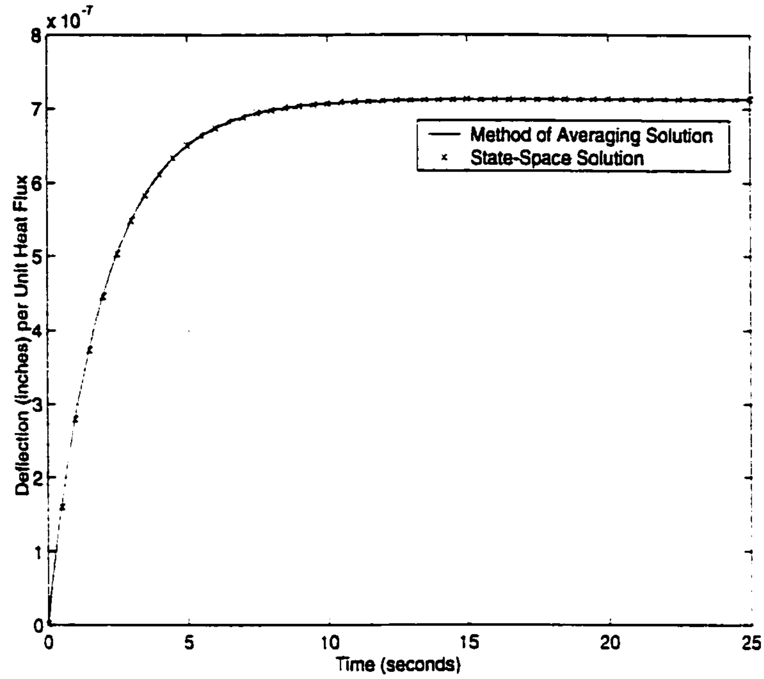

Figure A.1: Comparison of Method of Averaging and State-Space solutions: quasistatic deflection (in) per unit heat flux $\left(\frac{\text{Btu}}{\text{h ft}^2}\right)$ at the plate center.

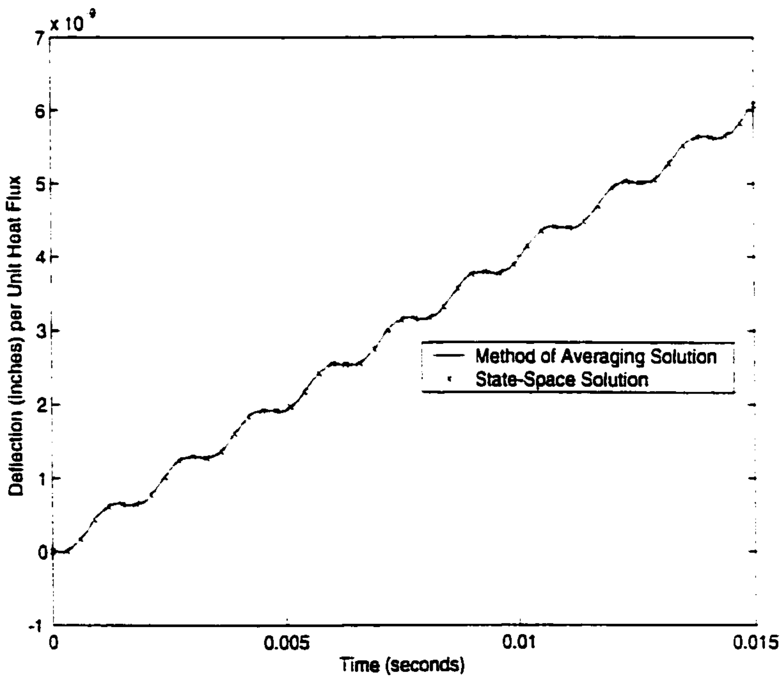

Figure A.2: Comparison of Method of Averaging and State-Space solutions: deflection (in) per unit heat flux $\left(\frac{\text{Btu}}{\text{h ft}^2}\right)$ at the plate center.

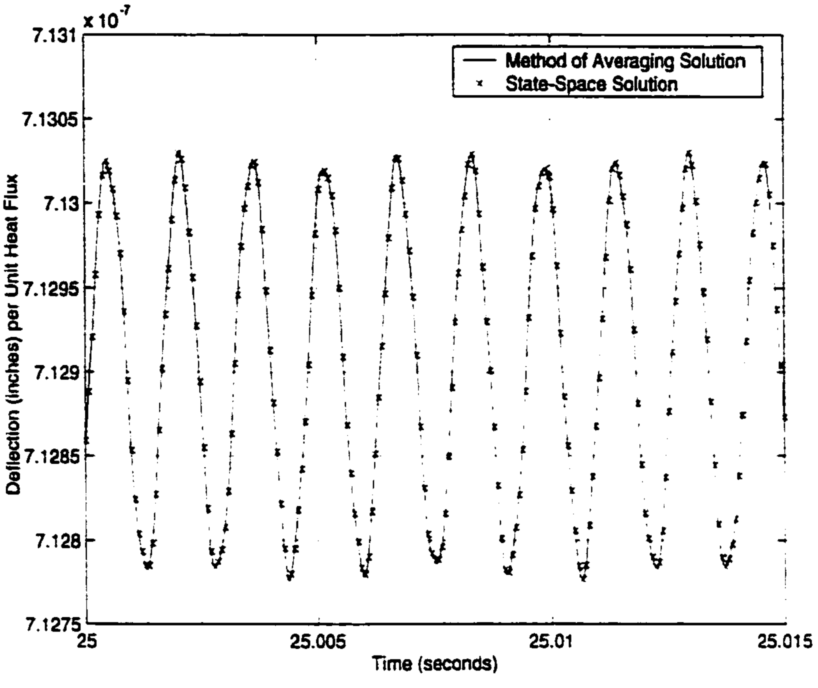

Figure A.3: Comparison of Method of Averaging and State-Space solutions: deflection (in) per unit heat flux $\left(\frac{\text{Btu}}{\text{h ft}^2}\right)$ at the plate center.

APPENDIX B

SOURCE CODE

B.1. Overview

This appendix gives a brief description of the files and applications used to perform the symbolic and numerical computations associated with this work. Due to the volume and length of the files, all source code for these files is provided on a CD-ROM instead of as a printed listing.

B.2. File And Application Descriptions

This section describes the files and their associated application. This section separates the files used by the Chapter they are associated with.

B.2..1 Chapter 1 Files and Applications

There are no files or applications associated with Chapter 1.

B.2..2 Chapter 2 Files and Applications

The applications associated with the Chapter 2 files are:

1. **Compaq Visual Fortran version 6.0**: This application is part of the Microsoft Visual Studio family of compilers. It was used to develop and compile the FORTRAN (.for) files that implement the equations in the paper by V. I. Kozlov [12]. The setup for the compiler and linker for each program is controlled by the associated project files (.dsp). The workspace file (.dsw) contains one or more project files.

2. **MATLAB version 6.1**: This application is used for general purpose numerical computation and data visualization. The MATLAB m-files (.m) are ASCII files (text files) containing code that can be executed in the MATLAB command window. The MATLAB mat-files are binary files containing data and the associated MATLAB variable name.

3. **Maple V Release 5.1**: This application was used for symbolic manipulation. It was used to check for dimensional consistency in the equations used in the modeling files.

The files associated with Chapter 2 are:

1. **kozlov.dsw**: This workspace file contains the projects associated with the implementation of the equations found in the work by V. I. Kozlov [12].

2. **alumkozlov.dsp**: This project file contains the compiler and linker settings for the FORTRAN file alumkozlov.for.

3. **alumkozlov.for**: This text file contains the FORTRAN source code that implements the equations governing the response of a square aluminum plate subjected to a thermal shock derived in [12].

4. **alumdecay.dsp**: This project file contains the compiler and linker settings for the FORTRAN file alumdecay.for.

5. **alumdecay.for**: This text file contains the FORTRAN source code to compute the vibration response decay rate of the aluminum plate analyzed using alumkozlov.for. It utilizes the response equations coded in alumkozlov.for.

6. **AlumCh2.m**: This script m-file implements the solution developed in Chapter 2 for a square aluminum plate.

7. **AlumCh2Decay.m**: This script m-file contains the code to compute the vibration response decay rate of the aluminum plate analyzed using AlumCh2.m. It utilizes the response equations developed in Chapter 2.

8. **GrEpCh2.m**: This script m-file implements the solution developed in Chapter 2 for a square 0/90/90/0 4 layer graphite-epoxy plate.

9. **GrEpCh2Decay.m**: This script m-file contains the code to compute the vibration response decay rate of the graphite-epoxy plate analyzed using GrEpCh2.m. It utilizes the response equations developed in Chapter 2.

10. **GenCh2Figs.m**: This script m-file generates the figures used in Chapter 2.

11. **Ch2Fig$x$.m**: Where x takes the values from 1 to 9. These script m-files generate the individual figures in Chapter 2.

12. **Ch2Fig$x$.mat**: Where x takes the values from 1 to 9. These mat-files contain the data needed to generate the figures in Chapter 2.

13. **Ch2Tabl3Alum.m**: This script m-file computes the steady-state thermal moments at the center of the aluminum plate.

14. **Ch2Tabl3GrEp.m**: This script m-file computes the steady-state thermal moments at the center of the graphite-epoxy plate.

15. **Ch2UnitCheck.msw**: Maple file containing commands to check the units on the variables used in the m-files AlumCh2.m. AlumCh2Decay.m. GrEpCh2.m. and GrEpCh2Decay.m.

B.2..3 Chapter 3 Files and Applications

The applications associated with the Chapter 3 files are:

1. **Maple V Release 5.1**: It was used to derive numerically implementable versions of the equations associated with the finite element mass. stiffness. coupling. input. sensor. and actuator matrices/vectors derived in Chapter 3. These equations were then output as FORTRAN source code that was subsequently converted to MATLAB m-file function code used to obtain the finite element model. This application was also used to check for unit consistency in the formulas used to construct the finite element model.

2. **MATLAB version 6.1.**

The files associated with Chapter 3 are:

1. **FEModelDevelopment.msw**: Maple file containing commands to derive equations for the finite element mass, stiffness. coupling. and input matrices/vectors and FORTRAN source files implementing equations.

2. **FEModelDevelopmentExtra.msw**: Maple file containing supplemental derivations used to check validity of Maple commands in FEModelDevelopment.msw.

3. **Ch3UnitCheck.msw**: Maple file containing commands to check the units on the variables used in the m-files associated with the generation of the finite element model.

4. **TwoPointQuadratureTest.mws:** This Maple file contains commands to verify the analytic two point Gauss quadrature formula in [47].

5. **ReddyEx4p10.mws:** This Maple file contains commands to verify the solution found in Example 4.10 of Reddy [46].

6. **MatrixCheck.txt:** This Maple text file was used to verify the m-file code used to compute the finite element mass, stiffness, and damping matrices by comparing the results computed in MATLAB to the results computed numerically in Maple.

7. **AlumSSPlate.m**: This is the main script m-file for generating a linear finite element model of a simply supported aluminum plate with both uniform thermal and uniform pressure loading on the top surface as inputs. It stores the resulting model in **AlumSSPlateModel.mat.**

8. **GrEpSSSmartPlate.m**: This is the main script m-file for generating a finite element model of a simply supported orthotropic laminated graphite-epoxy plate with both uniform thermal and uniform pressure loading on the top surface as inputs. The model also includes a piezoelectric sensor and actuator pair bonded to the top and bottom surface and the associated inputs and outputs. It stores the resulting model in **GrEpSSSmartPlateModel.mat.** It can also store data for debugging in the files **MechFE.mat** and **ThermFE.mat.**

9. **InitDispFiniteElements.m**: This m-file function defines the mechanical finite element mesh based on the plate dimensions and the number of finite elements in the x and y directions, and the boundary conditions.

10. **InitThermFiniteElements.m**: This m-file function defines the thermal finite element mesh based on the plate dimensions, the number of finite elements in the x, y, and z directions, the

actuator and sensor height, and the number of elements in the z direction associated with the piezoelectric sensors and actuators.

11. **AluminumParameters.m:** This m-file function defines the mechanical and thermal characteristics of an aluminum plate.

12. **GrEpParameters.m:** This m-file function defines the mechanical and thermal characteristics of a layered graphite-epoxy plate based on the plate height, graphite epoxy layer orientation, the graphite fiber weight fraction, and the laminate void volume fraction.

13. **PZTParameters.m:** This m-file function defines the mechanical, thermal, and piezoelectric characteristics of PZT, from Zhou *et al* [9].

14. **SmartPlateParameters.m:** This m-file function computes the smart plate parameters based on the data from **GrEpParameters** and **PZTParameters** as well as the piezoelectric actuator and sensor thicknesses.

15. **Stiffness.m:** This m-file function computes the plate extensional, coupling, and bending stiffness coefficients associated with the given reduced stiffness coefficient and the laminate geometry.

16. **RotateStiffness.m:** This m-file function computes the stiffness of a laminate that has been rotated about the z axis.

17. **Inertias.m:** This m-file function computes the plate normal, coupling, and rotary inertias associated with the given laminate density and the laminate thicknesses.

18. **ThermoMechanicalCouplingCoeff.m:** This m-file function computes the thermo-mechanical coupling coefficient matrix, β, from the stiffness matrix and the thermal expansion coefficient matrix.

19. **TensorTransform.m:** This m-file function performs tensor transformations (rotations).

20. **ThermalMass.m:** This file computes the finite element thermal mass matrix.

21. **ThermalStiffness.m:** This m-file function computes the finite element thermal stiffness matrix.

22. **ThemalStiffnessBCxx.m:** Where xx takes on the values x0. xn. y0. and yn. These m-file functions are used to modify the thermal stiffness matrices of boundary finite elements.

23. **ThermoMechanicalDamping.m:** This m-file function computes the finite element thermomechanical damping coupling matrix.

24. **MechanicalThermoStiffness.m:** This m-file function computes the finite element mechanical-thermal stiffness coupling matrix.

25. **MechanicalStiffness.m:** This m-file function computes the finite element mechanical stiffness matrix.

26. **MechanicalMass.m:** This m-file function computes the finite element mechanical mass matrix.

27. **ActuatorInput.m:** This m-file function computes the finite element piezoelectric actuator input vectors associated with the mechanical and thermal differential equations.

28. **ActuatorInput2.m:** This m-file function computes the finite element piezoelectric actuator input vectors associated with the mechanical and thermal differential equations for the case where the piezoelectric actuator partially covers the area of the mechanical/thermal finite element.

29. **SensorOutput.m:** This m-file function computes the finite element piezoelectric sensor output vectors associated with the mechanical and thermal differential equations.

30. **SensorOutput2.m:** This m-file function computes the finite element piezoelectric sensor output vectors associated with the mechanical and thermal differential equations for the case where the piezoelectric sensor partially covers the area of the mechanical/thermal finite element.

31. **AddDamping.m**: This m-file function computes the global mechanical damping matrix based on equation (3.227).

32. **AddRayleighDamping.m**: This m-file function computes the Rayleigh global mechanical damping matrix based on the equations in [65].

33. **zout.m**: This m-file function replaces small numbers in a matrix with zero. Size of the number that is considered small can be specified through an input argument.

34. **Ch2VsCh3ModelComparison:** This m-file script generates the figures that compare the Chapter 2 solution to the Chapter 3 solution of the thermal impact of a simply supported rectangular aluminum plate.

35. **CheckoutMechFE.m:** This m-file script is used to debug the mechanical finite element portion of the coupled thermomechanical model. It uses the data stored in **MechFE.mat**.

36. **ReddyEx4p10.m:** This script m-file is used to validate the mechanical finite element portion of the coupled thermomechanical model by comparing the plate center vertical deflection to the results found using the equations in Reddy [46]. Example 4.10.

37. **CheckoutThermFE.m:** This m-file script is used to debug the thermal finite element portion of the coupled thermomechanical model. It uses the data stored in **ThermFE.mat**.

38. **AlumSSPlateModel.mat:** This mat-file contains the simply supported aluminum plate model generated by **AlumSSPlate.m.**

39. **GrEpSSSmartPlateModel.mat:** This mat-file contains the simply supported graphite-epoxy smart plate model generated by **GrEpSSSmartPlate.m.**

40. **MechFE.mat:** Data for the mechanical finite element portion of the coupled thermomechanical model. Used for debugging.

41. **ThermFE.mat:** Data for the thermal finite element portion of the coupled thermomechanical model. Used for debugging.

42. **OpenLoopResponse.m:** This script m-file computes the thermal impulse response of the model generated by **GrEpSSSmartPlate.m.**

43. **GrEpSSSmartPlateOL.mat:** This mat-file contains thermal impulse response data associated with the model generated by **GrEpSSSmartPlate.m.**

44. **ChandraFiniteElementModel.m:** This is the main script m-file for generating the finite element model described by Chandrashekhara and Agarwal [24]. It prompts the user for mat-file to store the resulting model.

45. **ChandraGrEpParameters.m:** This m-file function defines the mechanical characteristics of AS/3501-6 Graphite/Epoxy and the plate laminate configuration used in [24].

46. **ChandraPZTParameters.m:** This m-file function defines the mechanical and piezoelectric characteristics of PZT G1195, from Chandrashekhara and Agarwal. [24].

47. **ChandraComparison.m:** This script m-file generates the figures similar to those presented in [24]. It uses the data stored in **OriginalPlateModel.mat**, **RateFeedback.mat**, and **PositionFeedback.mat**.

48. **OriginalPlateModel.mat**: This mat-file contains data for the response of the original plate sans piezoelectric sensors and actuators.

49. **RateFeedback.mat**: This mat-file contains data for the open-loop response of the smart plate and the closed-loop response of the smart plate using rate feedback.

50. **PositionFeedback.mat**: This mat-file contains data for the closed-loop response of the smart plate using position feedback.

B.2..4 Chapter 4 Files and Applications

MATLAB version 6.1 was the only application associated with the Chapter 4 files. The files associated with Chapter 4 are:

1. **OptimizeChandra$x$.m:** Where x can be 1, 2, or 3. These script m-files were used to optimize the three different fixed feedback gain controllers designed in Section 4.4.1. The final design results were saved in **OptimalController$x$.mat**.

2. **DOT500MEX.dll:** A MATLAB MEX-file of the FORTRAN Design Optimization Tools (DOT) optimization routine. Commercial product, not included on CD.

3. **ChandraSmartPlateLinSim.mdl:** Simulink model used to compute the time response associated with design 1 in Section 4.4.1.

4. **ChandraSmartPlateNLSim.mdl:** Simulink model used to compute the time response associated with designs 2 and 3 in Section 4.4.1.

5. **GainIncreaseController1.mat:** This mat-file contains the performance data associated with a linear design that uses gains twice as large as the optimal design 1 gains. This data was used to illustrate that increasing the gains above the optimal values did not improve the impulse response.

6. **ChandraDesignComparison.m:** This script m-file generates the figures that compare the three different fixed feedback gain controllers designs. It also generates the figures that compare the optimal design 1 with a design that uses gains twice as big. It uses the data stored in the mat-files **OptimalController$x$.mat** and **GainIncreaseController1.mat**.

7. **ModelReductionTest.m:** This m-file script is used to develop the reduced state model using the balanced model reduction technique outlined in Appendix A. The order of the reduced state model is iterated on until the smallest model that closely matched the full state model is obtained. The reduced state model is saved in mat-files **MRTest$x$.mat**, where x can be 1 through 3. Once a good reduced order model has been created, the mat-file **MRTest$x$.mat**, containing this model is renamed to **GrEpSSSmartPlateBRModel.mat**.

8. **CompareOLModels.m:** This m-file script generates time domain thermal impulse responses and frequency domain singular value data of the full state model and the reduced state model

for comparison. It stores the data in **CompareOLModels.mat.** It uses the models stored in **GrEpSSSmartPlateModel.mat** and **GrEpSSSmartPlateBRModel.mat.**

9. **Ch4ModelComparison.m:** This m-file script generates the figures that compare the full state model to the reduced state model using the data stored in **CompareOLModels.mat.**

10. **OptimalController.m:** This script m-file was used to optimize the fixed feedback gain controller for a graphite/epoxy/PZT smart plate subjected to a thermal impulse. The final design results are stored in **OptimalThermalController.mat.**

11. **InitialThermalController.mat:** This mat-file contains the thermal impulse response of the fixed feedback gain controller used as an initial guess for the optimization routine.

12. **DesignComparison.m:** This m-file script generates the figures that compare the open-loop response. the initial feedback gain response. and the optimal feedback gain response.

B.2..5 Chapter 5 Files and Applications

There are no files or applications associated with Chapter 5.

B.2..6 Appendix A Files and Applications

MATLAB version 6.1 was the only application associated with the Appendix A files. The files associated with Appendix A are:

1. **GrEpAppA.m**: This script m-file generates the model used in Appendix A. and stores it in **AppAModel.mat.**

2. **GenAppAFigs.m**: This script m-file generates the figures used in Appendix A.

3. **AppAFig$x$.m**: Where x takes the values from 1 to 3. These script m-files generate the individual figures in Appendix A.

4. **AppAFig$x$.mat**: Where x takes the values from 1 to 3. These mat-files contain the data needed to generate the figures in Appendix A.

5. **AppAModel.mat**: This mat-file contains the state-space model generated using the method described in Appendix A. It is used in the AppAFig$x$.m files to generate the response for the State-Space solution method described in Appendix A.

B.3. CD-ROM File Structure

The files listed above are stored on the accompanying CD-ROM. The file structure is as follows: The root directory contains a directory for each chapter, *Chapter#*, that has files as listed above. Each chapter directory has subdirectories for the applications that use the files. For example, the directory *Chapter2* contains the directories *CompaqVF*, *Maple*, and *Matlab*. The root directory also contains a directory named *DissertationSource* which contains the LaTeXfiles (including additional macros and the OU dissertation style) and graphics files used to create this document using *Scientific Word* 3.51. Adobe Illustrator version 7.0 was used to create the graphics files with the file extension .ai.